การประดิษฐ์เซลล์สุริยะชนิดฟิล์มบาง $Cu(In,Ga)Se_2$ จากระบบฟิล์มบาง $CuInSe_2/CuGaSe_2$ และ $CuGaSe_2/CuInSe_2/CuGaSe_2$

นางสาวบุศรินทร์ น้อยแก้ว

บทคัดย่อและแฟ้มข้อมูลฉบับเต็มของวิทยานิพนธ์ตั้งแต่ปีการศึกษา 2554 ที่ให้บริการในคลังปัญญาจุฬาฯ (CUIR)
เป็นแฟ้มข้อมูลของนิสิตเจ้าของวิทยานิพนธ์ ที่ส่งผ่านทางบัณฑิตวิทยาลัย
The abstract and full text of theses from the academic year 2011 in Chulalongkorn University Intellectual Repository (CUIR)
are the thesis authors' files submitted through the University Graduate School.

วิทยานิพนธ์นี้เป็นส่วนหนึ่งของการศึกษาตามหลักสูตรปริญญาวิทยาศาสตรดุษฎีบัณฑิต
สาขาวิชาฟิสิกส์ ภาควิชาฟิสิกส์
คณะวิทยาศาสตร์ จุฬาลงกรณ์มหาวิทยาลัย
ปีการศึกษา 2558
ลิขสิทธิ์ของจุฬาลงกรณ์มหาวิทยาลัย

FABRICATION OF $Cu(In,Ga)Se_2$ THIN FILM SOLAR CELLS FROM $CuInSe_2/CuGaSe_2$ AND $CuGaSe_2/CuInSe_2/CuGaSe_2$ SYSTEMS

Miss Busarin Noikaew

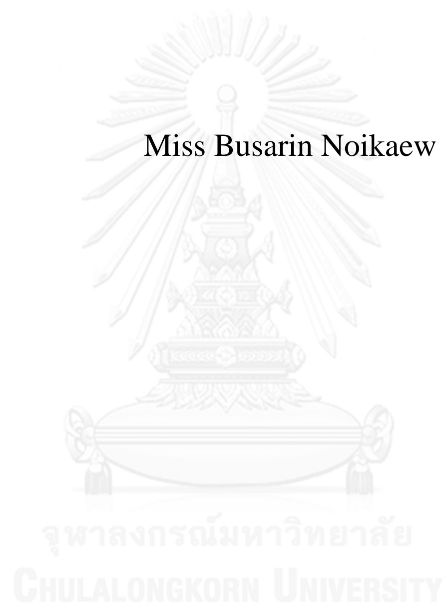

A Dissertation Submitted in Partial Fulfillment of the Requirements
for the Degree of Doctor of Philosophy Program in Physics
Department of Physics
Faculty of Science
Chulalongkorn University
Academic Year 2015

Copyright of Chulalongkorn University

Thesis Title	FABRICATION OF $Cu(In,Ga)Se_2$ THIN FILM SOLAR CELLS FROM $CuInSe_2/CuGaSe_2$ AND $CuGaSe_2/CuInSe_2/CuGaSe_2$ SYSTEMS
By	Miss Busarin Noikaew
Field of Study	Physics
Thesis Advisor	Assistant Professor Sojiphong Chatraphorn, Ph.D.

Accepted by the Faculty of Science, Chulalongkorn University in Partial Fulfillment of the Requirements for the Doctoral Degree

....Dean of the Faculty of Science
(Associate Professor Polkit Sangvanich, Ph.D.)

THESIS COMMITTEE

....Chairman
(Assistant Professor Thiti Bovornratanaraks, Ph.D.)
....Thesis Advisor
(Assistant Professor Sojiphong Chatraphorn, Ph.D.)
....Examiner
(Assistant Professor Tonphong Kaewkongka, Ph.D.)
....Examiner
(Varagorn Hengpunya, Ph.D.)
....External Examiner
(Assistant Professor Supab Choopun, Ph.D.)

บุศรินทร์ น้อยแก้ว : การประดิษฐ์เซลล์สุริยะชนิดฟิล์มบาง $Cu(In,Ga)Se_2$ จากระบบฟิล์มบาง $CuInSe_2/CuGaSe_2$ และ $CuGaSe_2/CuInSe_2/CuGaSe_2$ (FABRICATION OF $Cu(In,Ga)Se_2$ THIN FILM SOLAR CELLS FROM $CuInSe_2/CuGaSe_2$ AND $CuGaSe_2/CuInSe_2/CuGaSe_2$ SYSTEMS) อ.ที่ปรึกษาวิทยานิพนธ์หลัก: ผศ. ดร.โศจิพงศ์ ฉัตราภรณ์, หน้า.

เซลล์สุริยะประสิทธิภาพสูงชนิดฟิล์มบางคอปเปอร์อินเดียมแกลเลียมไดซีลีไนด์ (CIGS) ถูกประดิษฐ์ลงบนแผ่นรองรับกระจกโซดาไลม์ (SLG) ที่เคลือบด้วยโมลิบดินัม โดยวิธีการระเหยร่วมแบบสามขั้นตอน การรวมตัวของชั้นฟิล์มตั้งต้น $(In,Ga)_2Se_3$ ได้รับอิทธิพลมาจากฟลักซ์ของธาตุซีลีเนียมในขั้นตอนที่หนึ่ง อุณหภูมิธาตุซีลีเนียมที่พอเพียงตลอดการทดลองสำหรับงานวิจัยนี้คือ 300 องศาเซลเซียส อีกทั้งอิทธิพลของอุณหภูมิแผ่นรองรับในระหว่างขั้นตอนที่หนึ่ง (T_1) และขั้นตอนที่สองและสาม (T_2) ได้ถูกตรวจสอบเพื่อหาค่าที่เหมาะสมในการปลูกฟิล์มแบบสามขั้นตอน พบว่าอุณหภูมิในขั้นตอนที่หนึ่ง 370 องศาเซลเซียส และอุณหภูมิในขั้นตอนที่สองและสาม 520 องศาเซลเซียสนั้นส่งผลให้เซลล์สุริยะมีประสิทธิภาพสูงที่สุดคือ 13.7 เปอร์เซ็นต์ อย่างไรก็ตามกระบวนการปลูกฟิล์มแบบสามขั้นตอนมีการใช้ธาตุเป็นจำนวนมาก เช่น คอปเปอร์ อินเดียม แกลเลียม และซีลีเนียม รวมถึงระยะเวลาปลูกฟิล์มด้วย การปลูกฟิล์มบางคอปเปอร์อินเดียมไดซีลีไนด์/คอปเปอร์แกลเลียมไดซีลีไนด์ (CIS/CGS) และฟิล์มบางคอปเปอร์แกลเลียมไดซีลีไนด์/คอปเปอร์อินเดียมไดซีลีไนด์/คอปเปอร์แกลเลียมไดซีลีไนด์ (CGS/CIS/CGS) ถูกเตรียมขึ้นเพื่อเพิ่มประสิทธิภาพของเซลล์สุริยะ เมื่อเปรียบเทียบกับการเตรียมฟิล์มแบบสามขั้นตอน การยกระดับอัตราส่วนธาตุแกลเลียมทั้งด้านหน้าและด้านหลังได้มาจากการปลูกฟิล์มชั้นดูดกลืนแสงแบบ CIS/CGS และ CGS/CIS/CGS โดยที่การยกระดับอัตราส่วนธาตุแกลเลียมด้านหลังของชั้นฟิล์ม CIS/CGS แสดงถึงแนวโน้มการเพิ่มขึ้นของค่าเฉลี่ยกระแสจากการช่วยของสนามไฟฟ้าด้านหลังฟิล์ม แต่ค่าแรงดันไฟฟ้ามีค่าต่ำลงเนื่องจากปริมาณอัตราส่วนธาตุแกลเลียมลดลงที่ด้านหน้ารอยต่อฟิล์ม นอกจากนี้ชั้นดูดกลืนแสง CGS/CIS/CGS ที่แสดงถึงอัตราส่วนของธาตุแกลเลียมที่มากขึ้นทั้งด้านหน้าและด้านหลังฟิล์มส่งผลให้ค่าแรงดันไฟฟ้าเพิ่มสูงขึ้นได้เมื่อเทียบกับชั้นฟิล์ม CIS/CGS ประสิทธิภาพที่สูงที่สุดของเซลล์สุริยะที่เตรียมมาจากความหนา 1.8 ไมครอนของชั้นฟิล์ม CIS/CGS และ CGS/CIS/CGS ยังแสดงค่าสูงที่สุดถึง 15.5 เปอร์เซ็นต์ และ 12.5 เปอร์เซ็นต์ ตามลำดับ อีกทั้งประสิทธิภาพเชิงควอนตัมของชั้นดูดกลืนแสงทั้งสองชนิดที่ความหนา 1.8 ไมครอน ยังแสดงถึงขอบเขตการดูดกลืนแสงที่เพิ่มขึ้นในช่วงความยาวคลื่นย่านไกล และยังพบว่าการลดความหนาชั้นดูดกลืนแสงของชั้นฟิล์ม CGS/CIS/CGS ลงไประดับ 0.8 และ 1.2 ไมครอนยังให้ค่าประสิทธิภาพของเซลล์สุริยะอยู่ในระดับเดียวกับชั้นฟิล์ม CIS/CGS ที่ความหนา 1.8 ไมครอนอีกด้วย

ภาควิชา	ฟิสิกส์	ลายมือชื่อนิสิต	....
สาขาวิชา	ฟิสิกส์	ลายมือชื่อ อ.ที่ปรึกษาหลัก	....
ปีการศึกษา	2558		

5373916623 : MAJOR PHYSICS
KEYWORDS: CIGS, BILAYER, TRILAYER,THIN FILM SOLAR CELLS

BUSARIN NOIKAEW: FABRICATION OF $Cu(In,Ga)Se_2$ THIN FILM SOLAR CELLS FROM $CuInSe_2/CuGaSe_2$ AND $CuGaSe_2/CuInSe_2/CuGaSe_2$ SYSTEMS. ADVISOR: ASST. PROF. SOJIPHONG CHATRAPHORN, Ph.D., pp.

High efficiency $Cu(In,Ga)Se_2$ (CIGS) thin film solar cells are usually deposited on Mo-coated soda-lime glass (SLG) substrates by the three-stage co-evaporation process. The formation of $(In,Ga)_2Se_3$ precursor layer is strongly affected by the Se flux supplied during the 1st stage. The Se source temperature of 300°C is sufficient for the entire deposition in this work. The influence of the substrate temperatures during 1st stage (T_1) and the 2nd and 3rd stages (T_2) is investigated for the optimum values of T_1 and T_2. The values of T_1= 370°C and T_2=520°C result in the device's maximum efficiency of 13.7%. However, this technique consumes a lot of material, e.g. Cu, In, Ga and Se, as well as the deposition time. The depositions of CIS/CGS bilayer and CGS/CIS/CGS trilayer are employed in order to enhance the efficiency of the devices when compared with those fabricated by the 3-stage deposition process. The front and back Ga-grading are obtained from the depositions of the bilayer and trilayer absorbers, respectively. The bilayer absorbers with back Ga-grading show the increasing trend of the average value of the short-circuit current density (J_{sc}) due to the assisting back surface field, but the average open-circuit voltage (V_{oc}) is significantly low due to the reduction of Ga content at the front surface. On the other hand, the CGS/CIS/CGS trilayer absorbers show double Ga-grading resulting in the increase of the V_{oc} when compared with the CIS/CGS bilayers. The highest efficiencies of the devices fabricated from the 1.8 µm thick CIS/CGS bilayer and CGS/CIS/CGS trilayer absorber, show the maximum value of 12.5% and 15.5%, respectively. The external quantum efficiency (EQE) of the 1.8 µm thick bilayer and trilayer absorbers shows the enhancement in the long wavelengths. It was found that the 0.8 and 1.2 µm thick trilayer absorbers can maintain the same level of efficiency to that of the bilayer absorber of 1.8 µm thick.

Department:	Physics	Student's Signature	....
Field of Study:	Physics	Advisor's Signature	....
Academic Year:	2015		

ACKNOWLEDGEMENTS

I would like to thank you my thesis advisor, Assistant Professor Dr. Sojiphong Chatraphorn for the useful suggestion and initiate new outstanding ideas for all my course of the dissertation. Apart from this, Assistant Professor Dr. Kajornyod Yoodee also encouraged me in term of searching additional knowledge and information.

Then, I also would like to thank you the committee, Assistant Professor Dr. Thiti Bovornratanaraks, Assistant Professor Dr. Tonphong Kaewkongka, Dr. Varagorn Hengpunya and Assistant Professor Dr. Supab Choopun for usefulness comments and helpfulness in the Thesis defense.

I would like to thank Semiconductor Physics Research Laboratory (SPRL) and members from the past to the present, especially, Dr. Rachsak Sakdanuphab, Mr. Marut Puangsudrak and Miss Boonyaluk Namnuan throughout the study for their helping and generousness and then give me the friendship.

I would like to acknowledge the financial supports from Thailand Center of Excellence in Physics (ThEP Center), the Asahi Glass Foundation, Ratchadaphiseksomphot Endowment Fund of Chulalongkorn University (RES560530181-AM), the Special Task Force for Activating Research (STAR), Ratchadaphiseksomphot Endowment Fund, Chulalongkorn University through the Energy Materials Physics Research Group and Research Funds from the Faculty of Science, Chulalongkorn University and the 90th Anniversary of Chulalongkorn University Fund (Ratchadaphisek-somphot Endowment Fund).

I would like to thank for Mr. Pornsak Panchawirat (ThEP Center, Thailand) for helping with FESEM and EDS measurements, and the Department of Geology, Faculty of Science, Chulalongkorn University for the access to the XRD facility.

Finally, I would like to thank for encouragement from my family and friends to contribute my effortless completing the thesis.

CONTENTS

Page

THAI ABSTRACT iv

ENGLISH ABSTRACT v

ACKNOWLEDGEMENTS vi

CONTENTS vii

LISTS OF TABLES x

LISTS OF FIGURES xi

CHAPTER I INTRODUCTION 1

1.1 Overview 1

1.2 The fabrication methods of CIGS thin films 2

1.3 The fabrication of Ga-grading profiles 4

1.4 Objectives 6

1.5 Scope of this dissertation 7

CHAPTER II THEORETICAL BACKGROUND 8

2.1 General properties of $Cu(In,Ga)Se_2$ 8

2.2 Phase formation of $Cu(In,Ga)Se_2$ materials 13

2.2.1 Phase diagram of Cu-In-Se system 13

2.2.2 Phase diagram of Cu-Ga-Se system 13

2.2.3 Phase diagram of Cu-In-Ga-Se system 14

2.3 The electrical properties of solar cells 15

2.3.1 J-V characteristics of solar cells 15

2.3.2 The p-n junction of solar cells 18

2.3.3 Normal and double Ga-grading of CIGS solar cells 19

2.4 CIGS thin film deposition by co-evaporation method 21

2.4.1 The three-stage process 21

2.4.2 The single process 29

2.4.3 The bilayer process 30

2.4.4 The trilayer process 31

CHAPTER III EXPERIMENTAL PROCEDURES 33

Page

3.1 Fabrication processes of CIGS thin film solar cells 33
3.1.1 SLG substrate preparation 35
3.1.2 Mo back contact 36
3.1.3 CdS buffer layer 36
3.1.4 ZnO window layers 37
3.1.5 Al-grid front contact 38
3.2 Solar cell characterizations 38
3.2.1 Current density-Voltage measurement (J-V) 38
3.2.2 External Quantum Efficiency measurement (EQE) 39
CHAPTER IV THE FABRICATION OF CIGS THIN FILM SOLAR CELLS BY THE THREE-STAGE PROCESS 41
4.1 The effect of Se source temperatures on $(In,Ga)_2Se_3$ precursors......................44
4.2 The effect of substrate temperatures on CIGS thin film solar cells..................50
4.2.1 FESEM cross-section images of varying substrate temperatures in the 1st stage 50
4.2.2 XRD patterns of varying substrate temperatures in the 1st stage 50
4.2.3 J-V measurements of varying substrate temperatures in the 1st stage 51
4.2.4 FESEM cross-section images of varying substrate temperatures in the 2nd and 3rd stages...55
4.2.5 XRD patterns of varying substrate temperatures in the 2nd and 3rd stages 57
4.2.6 J-V measurements of varying substrate temperatures in the 2nd and 3rd stages 57
4.3 Summary...61
CHAPTER V THE FABRICATION OF CIGS THIN FILM SOLAR CELLS USING BILAYER AND TRILAYER SYSTEMS 62
5.1 CGS and CIS single layer grown by the single stage process 62
5.1.1 FESEM surface and cross-section images of CGS and CIS single layer 63
5.1.2 XRD patterns of CGS and CIS single layer 63

Page

5.1.3 J-V measurements of CGS and CIS single layer....64
5.1.4 EQE measurements of CGS and CIS single layer....64
5.2 CGS/CIS and CIS/CGS bilayers....67
5.2.1 FESEM surface and cross-section images of CGS/CIS and CIS/CGS bilayers....68
5.2.2 EDS depth profiles of CGS/CIS and CIS/CGS bilayers....72
5.2.3 XRD patterns of CGS/CIS and CIS/CGS bilayers....73
5.2.4 J-V measurements of CGS/CIS and CIS/CGS bilayers....74
5.2.5 EQE measurements of CGS/CIS and CIS/CGS bilayers....77
5.3 CGS/CIS/CGS trilayers grown by the trilayer processes....79
5.3.1 FESEM surface and cross-section images of CGS/CIS/CGS trilayers....80
5.3.2 EDS depth profiles of CGS/CIS/CGS trilayers....82
5.3.3 XRD patterns of CGS/CIS/CGS trilayers....83
5.3.4 J-V measurements of CGS/CIS/CGS trilayers....85
5.3.5 EQE measurements of CGS/CIS/CGS trilayers....87
5.4 The comparison of Ga-graded and homogeneous bandgap of CIGS thin film solar cells....88
5.4.1 J-V Characteristics....88
5.4.2 EQE measurements....89
5.5 Summary....91
CHAPTER VI CONCLUSION....92
....95
REFERENCES....95
APPENDIX....99
List of Symbols and Abbreviations....99
VITA....103

LISTS OF TABLES

Page

Table 1 Various deposition processes for CIGS thin film fabrication. 3

Table 2 Lattice mismatch values (ε) of CGS/CIS and CIS/CGS bilayers 9

Table 3 The parameters for a deposition of CIGS by the three-stage. 24

Table 4 Density, molecular mass and α_i parameter of the materials for CIGS thin film deposition. 27

Table 5 The parameters for deposition of CGS and CIS single layer. 29

Table 6 The parameters for deposition of CGS/CIS and CIS/CGS bilayers. 31

Table 7 The parameters for deposition of CGS/CIS/CGS trilayers. 32

Table 8 The variation of Se composition and thickness of precursor layers by varying Se source temperatures at 280°C, 300°C and 320°C. 49

Table 9 The solar cell parameters of varying Se source temperatures at 280°C and 300°C. 49

Table 10 The solar cell parameters of varying substrate temperatures in the 1st stage at 300°C, 350°C, 370°C, 390°C and 410°C with constant substrate temperature in the 2nd and 3rd stages at 580°C. 55

Table 11 The solar cell parameters of varying substrate temperatures in the 2nd and 3rd stages at 500°C, 520°C, 540°C, 560°C and 580°C with constant substrate temperature in the 1st stage at 370°C. 61

Table 12 The solar cell parameters of CGS and CIS single layer. 66

Table 13 The solar cell parameters of CGS/CIS and CIS/CGS bilayers. 75

Table 14 The solar cell parameters of various CGS/CIS/CGS trilayer thicknesses. 85

Table 15 The deposition times with the efficiencies of the 3-stage CIGS, CIS/CGS bilayers and CGS/CIS/CGS trilayers absorbers. 89

LISTS OF FIGURES

Page

Figure 1 The crystal structures of chalcogenide compound; (a) zincblende structure........8
Figure 2 The bandgap energy of the Cu(In,Ga,Al)(Se,S)$_2$ alloy system as a function of lattice constant a. 9
Figure 3 The alloyed CIGS with homogeneous or non-homogeneous distribution of In and Ga. 10
Figure 4 (a) Theoretical efficiencies of various solar cell materials as a function of bandgap energy at AM1.5. (b) Absorption coefficient of $CuInSe_2$ material compared with the variation of photovoltaic materials........12
Figure 5 Phase diagram along the Cu_2Se-In_2Se_3 psudobinary of $CuInSe_2$ compound........13
Figure 6 Phase diagram along the Cu_2Se-Ga_2Se_3 psudobinary of $CuGaSe_2$ compound........14
Figure 7 Isothermal quasi-ternary Cu_2Se-In_2Se_3-Ga_2Se_3 phase diagram of Cu(InGa)Se$_2$ compounds at room temperature. 15
Figure 8 J-V characteristic curve of a solar cell........16
Figure 9 One-diode equivalent circuits of an illuminated solar cell. 17
Figure 10 Energy band diagram of heterojunction CIGS thin film solar cell with recombination paths; A = interface recombination, B = space charge region recombination, C = neutral bulk recombination and D = back contact recombination. 19
Figure 11 Schematic diagrams of the bandgap energy of Cu(In,Ga)Se$_2$ (a) uniform bandgap (b) front grading, (c) back grading and (d) double grading. 20
Figure 12 (a) The schematic illustration inside the vacuum growth chamber. (b) The photograph of the co-evaporation systems including the growth chamber, controller systems, real-time monitor and diffusion pump. 22

Figure 13 Schematic diagram of (a) The three-stage growth profile by varying low substrate temperature at the 1st stage (T1) and then, varying the increased substrate temperature at the 2nd stage and the 3rd stage (T2). (b) Thin film composition for CIGS growth in the three-stage process, y=[Cu]/([In]+[Ga]) is shown in the solid line, x=[Ga]/([In]+[Ga]) is shown in the dash line. 23

Figure 14 The graph of evaporation rate versus elemental temperature of Cu, In and Ga sources to obtain *a* and *b* parameters by least-square fit which detected by QCM. 28

Figure 15 The evaporation profile of single layer process of (a) $CuGaSe_2$ with the ratio of [Ga]/([In]+[Ga]); x=1. (b) $CuInSe_2$ with the ratio of [Ga]/([In]+[Ga]); x=0............ 29

Figure 16 The evaporation profiles of bilayer deposition processes (a) CGS/CIS and (b) CIS/CGS. 30

Figure 17 The evaporation profile of trilayers deposition process of CGS/CIS/CGS trilayers............ 31

Figure 18 Schematic structure of $Cu(In,Ga)Se_2$ thin film solar cells............ 33

Figure 19 Schematic structure of $Cu(In,Ga)Se_2$ thin film solar cells prepared by Ga-grading profiles (a) front grading, (b) back grading and (c) double grading. 34

Figure 20 Diagram of CGS/CIS and CIS/CGS bilayers deposited under Cu-rich (y=1.2) and Cu-poor (y=0.9) conditions. 35

Figure 21 The schematic diagram of J-V measurement set up. 39

Figure 22 EQE spectrum of a CIGS solar cell showing the factors causing the current losses as labeled in each region. 40

Figure 23 The three-stage deposition process during CIGS thin film growth observed by the output power of substrate (blue line), the pyrometer signal (red line) and the substrate temperature (black line). Then, Cu composition observed by stoichiometric (y=1), Cu-rich (y>1) and Cu-poor (y<1). 43

จุฬาลงกรณ์มหาวิทยาลัย
Chulalongkorn University

Figure 24 The finished CIGS thin film grown on (a) 10 cm x 10 cm Mo-coated SLG substrate and (b) CIGS films was divided into 9 pieces of 3 cm x 3 cm. 43

Figure 25 The surface morphologies of $(In,Ga)_2Se_3$ precursors by varying Se source temperature at 280^oC in each different film area, cross-section image of $(In,Ga)_2Se_3$ precursor grown on Mo-coated SLG substrate and EDS result measured the Se composition in the IGS precursor layer. 46

Figure 26 The surface morphologies of $(In,Ga)_2Se_3$ precursors by varying Se source temperature at 300^oC in each different film area, cross-section image of $(In,Ga)_2Se_3$ precursor grown on Mo-coated SLG substrate and EDS result measured the Se composition in the IGS precursor layer. 47

Figure 27 The surface morphologies of $(In,Ga)_2Se_3$ precursors by varying Se source temperature at 320^oC in each different film area, cross-section image of $(In,Ga)_2Se_3$ precursor grown on Mo-coated SLG substrate and EDS result measured the Se composition in the IGS precursor layer. 48

Figure 28 J-V characteristics of the devices with best efficiency fabricated from varying Se source temperature at 280^oC and 300^oC. 49

Figure 29 FESEM cross-section images of CIGS thin film for varying substrate temperatures in the 1st stage at (a) 300^oC, (b) 350^oC, (c) 370^oC, (d) 390^oC and (e) 410^oC with constant substrate temperature in the 2nd and 3rd stages at 580^oC. 52

Figure 30 XRD patterns of CIGS thin film for varying substrate temperatures in the 1st stage at (a) 300^oC, (b) 350^oC, (c) 370^oC, (d) 390^oC and (e) 410^oC with constant substrate temperature in the 2nd and 3rd stages at 580^oC. 53

Figure 31 Distributions of CIGS solar cell parameters of the devices fabricated from varying substrate temperatures in the 1st stage at 300^oC, 350^oC, 370^oC, 390^oC and 410^oC with constant substrate temperature in the 2nd and 3rd stages at 580^oC. 54

จุฬาลงกรณ์มหาวิทยาลัย
Chulalongkorn University

Figure 32 J-V characteristics of the devices with best efficiency fabricated from varying substrate temperatures in the 1st stage at 300°C, 350°C, 370°C, 390°C and 410°C with constant substrate temperature in the 2nd and 3rd stages at 580°C. 54

Figure 33 EDS depth profile of CIGS absorber layer grown by the 3-stage process. 56

Figure 34 FESEM cross-section images of CIGS thin films for varying substrate temperatures in the 2nd and 3rd stages at (a) 500°C, (b) 520°C, (c) 540°C, (d) 560°C and (e) 580°C with constant substrate temperature in the 1st stage at 370°C. 58

Figure 35 XRD patterns of CIGS thin film for varying substrate temperatures in the 2nd and 3rd stages at 500°C, 520°C, 540°C, 560°C and 580°C with constant substrate temperature in the 1st stage at 370°C. 59

Figure 36 Distributions of CIGS solar cell parameters of the devices fabricated from varying substrate temperatures in the 2nd and 3rd stages at 500°C, 520°C, 540°C, 560°C and 580°C with constant substrate temperature in the 1st stage at 370°C. 60

Figure 37 J-V characteristics of the devices with best efficiency fabricated from varying substrate temperatures in the 2nd and 3rd stages at 500°C, 520°C, 540°C, 560°C and 580°C with constant substrate temperature in the 1st stage at 370°C. 60

Figure 38 The single stage process of CGS or CIS thin film observed by the output power of substrate heater (blue line), the pyrometer signal (red line) and the substrate temperature (black line). 63

Figure 39 FESEM surface morphologies of (a) CGS single layer, (b) CIS single layer and cross-section images of (c) CGS single layer, (d) CIS single layer. 65

Figure 40 XRD patterns of CGS and CIS single layer. 65

Figure 41 J-V characteristics of the devices with best efficiency fabricated from CGS and CIS single layer. 66

Figure 42 EQE curves of the devices with best efficiency fabricated from CGS and CIS single layer. 66

จุฬาลงกรณ์มหาวิทยาลัย
Chulalongkorn University

Figure 43 The bilayer deposition processes observed by the output power of substrate heater (blue line), the pyrometer signal (red line) and the substrate temperature setting (black line). 67

Figure 44 FESEM surface morphologies and cross-section images of (a),(b) CGS/CIS bilayers and (c),(d) CIS/CGS bilayers under Cu-poor(y=0.9)/Cu-poor(y=0.9) conditions. 70

Figure 45 FESEM surface morphologies and cross-section images of (a),(b) CGS/CIS bilayers and (c),(d) CIS/CGS bilayers under Cu-poor(y=0.9)/Cu-rich(y=1.2) 70

Figure 46 FESEM surface morphologies and cross-section images of (a),(b) CGS/CIS bilayers and (c),(d) CIS/CGS bilayers under Cu-rich(y=1.2)/Cu-rich(y=1.2) conditions...71

Figure 47 FESEM surface morphologies and cross-section images of (a),(b) CGS/CIS bilayers and (c),(d) CIS/CGS bilayers under Cu-rich(y=1.2)/Cu-poor(y=0.9) conditions. 71

Figure 48 EDS depth profiles of CGS/CIS and CIS/CGS bilayers grown under various Cu compositions...72

Figure 49 XRD patterns of CGS/CIS and CIS/CGS bilayers grown under various Cu compositions which compared to the CGS and CIS single layers. 73

Figure 50 Distributions of CIGS solar cell parameters of the devices fabricated from CGS/CIS bilayer grown under various Cu compositions................76

Figure 51 Distributions of CIGS solar cell parameters of the devices fabricated from CIS/CGS bilayer grown under various Cu compositions................76

Figure 52 J-V characteristics of the devices with best efficiency fabricated from CGS/CIS and CIS/CGS bilayers grown under various Cu compositions. 77

Figure 53 EQE curves of the devices with best efficiency fabricated from CGS/CIS and CIS/CGS bilayers grown under various Cu compositions. 78

จุฬาลงกรณ์มหาวิทยาลัย
Chulalongkorn University

Figure 54 The trilayer process of CGS/CIS/CGS thin film which observed by the output power of substrate (blue line), the pyrometer signal (red line) and the substrate temperature (black line). 79

Figure 55 FESEM surface morphologies and cross-section images of various CGS/CIS/CGS trilayer thicknesses (a) 1.8 µm, (b) 1.2 µm, (c) 0.8 µm and (d) 0.5 µm. 81

Figure 56 EDS depth profiles of various CGS/CIS/CGS trilayers thicknesses of 1.8 µm, 1.2 µm, 0.8 µm and 0.5 µm. 82

Figure 57 (a) XRD patterns of 3-stage process CIGS and various CGS/CIS/CGS trilayers thicknesses of 1.8 µm, 1.2 µm, 0.8 µm and 0.5 µm. (b) Segregation of CIGS (112) phase observed in the trilayer absorber....84

Figure 58 Distributions of CIGS solar cell parameters of the devices fabricated from1.8 µm of 3-stage process absorbers, trilayer of various thicknesses of 1.8 µm, 1.2 µm, 0.8 µm and 0.5 µm. 86

Figure 59 J-V characteristics of the devices with best efficiency fabricated from 3-stage process absorbers and various CGS/CIS/CGS trilayers thicknesses of 1.8 µm, 1.2 µm, 0.8 µm and 0.5 µm. 86

Figure 60 EQE curves of the devices with best efficiency fabricated from 3-stage process absorbers and various CGS/CIS/CGS trilayers thicknesses of 1.8 µm, 1.2 µm, 0.8 µm and 0.5 µm. 87

Figure 61 Distributions of CIGS solar cell parameters of the devices fabricated from bilayer, trilayer of various thicknesses and 3-stage process absorbers. 90

Figure 62 J-V characteristics of the devices with best efficiency fabricated from bilayer, trilayer of various thicknesses and 3-stage process absorbers. 90

Figure 63 EQE curves of the devices with best efficiency fabricated from bilayer, trilayer of various thicknesses and 3-stage process absorbers. 91

จุฬาลงกรณ์มหาวิทยาลัย
Chulalongkorn University

CHAPTER I
INTRODUCTION

1.1 Overview

A photovoltaic (PV) device such as a solar cell is one of the renewable energy sources that can create the electricity under illumination of sunlight. At the same time, fossil fuel (coal, petroleum and natural gas) combustion and nuclear fission exhaust CO_2 during energy production. Thus, solar energy becomes an environmentally clean, large areas occupying and proper energy storage systems. The photovoltaic effect was first discovered by Alexandre Edmond Becquerel in 1839. The PV device was made by Charles Fritts in 1883 using selenium on a thin layer of gold to form a device giving less than 1% efficiency. In 1954, Chapin et al. at Bell Labs announced the first modern silicon solar cell of 6% efficiency. In the same year, the group at Wright Patterson Air Force Base in the US published a thin film heterojunction solar cell based on Cu_2S/CdS at 6% efficiency. In 1958, Si based solar cell panels were deployed in Vanguard I satellite for space program and showed the highest efficiency when compared to the others. Although crystalline silicon technology has established excellent stability modules, thick films of crystalline silicon are at high-cost in manufacturing scale. An alternative for cost reduction is to turn to thin film technologies. Cu_2S/CdS heterojunction thin film solar cells were an origin for $CuIn_{1-x}Ga_xSe_2$ or (CIGS) thin film development [1]. Unfortunately, Cu_2S/CdS is unstable over some period of time. Most of thin film materials, CIGS-a semiconducting compound in I–III–VI_2 groups have been widely used for thin film solar cells. The advantages of CIGS thin film solar cells are its high absorption coefficient, direct bandgap, long-term stability and low cost of production [2-4]. The bandgap energy of CIGS materials can be adjusted in the range between 1.0-1.7 eV by varying the x ratio or Ga composition, where x is [Ga]/([In]+[Ga]), e.g. pure CIS is x =0 and pure CGS is x=1. Moreover, CIGS structure may also depend on the y ratio, where y is [Cu]/([In]+[Ga]). Thus, the ratio of Ga to group-III elements about 20-30% corresponds to bandgap energy of 1.1-1.2 eV that can yield the highest solar cell

performances [5]. In addition, the diffusion of Na from SLG through Mo layer during CIGS deposition can induce the p-type doping by enhancing the carrier concentration and conductivity leading to efficiency improvement [6]. At present, The world-record efficiencies of polycrystalline Cu(In,Ga)Se_2 (CIGS) thin film solar cells and solar modules grown on soda-lime glass (SLG) substrate have recently been improved to 22.3% [7] and 18.7%, respectively [8]. Moreover, CIGS thin film solar cells using flexible substrates have been attractive as a candidate for innovative applications.

1.2 The fabrication methods of CIGS thin films

A typical structure of CIGS thin film solar cells consist of six different thin film layers deposited on soda-lime glass (SLG) substrates; Al-grid/ZnO(Al)/i-ZnO/CdS/CIGS/Mo/SLG. The CIGS absorber layer is a p-type semiconductor while an n-type semiconductor is a ZnO window layer. The Al and Mo metallic layers are the front and the back contacts of the solar cell, respectively. CdS thin film is a buffer layer between p-CIGS absorber layer and n-ZnO window layer. CIGS thin film solar cells can be fabricated by various techniques such as sputtering [9, 10], selenization [11, 12], spray pyrolysis [13, 14], electro-deposition [15, 16] and co-evaporation [17-19], Although many deposition techniques have been developed, co-evaporation process may be more appropriated for the fabrication from a laboratory scale to a manufacturing scale due to lower production costs, shorter production time. Moreover, there are three main methods of co-evaporation process that are used for the fabrication of CIGS absorber layer, for example, single-stage, two-stage and three-stage deposition processes. The single-stage and two-stage processes are rather simple and rapid process, but the quality of CIGS thin film solar cells may not be at their best. The improvement of the quality of the CIGS material for photovoltaic devices is required toward the higher efficiency. The three-stage deposition process has been employed for the deposition of the CIGS absorber layer and yielded the highest efficiency among others. The other deposition processes for CIGS thin film fabrication are summarized in Table 1.

จุฬาลงกรณ์มหาวิทยาลัย
CHULALONGKORN UNIVERSITY

Table 1 Various deposition processes for CIGS thin film fabrication.

Methods	Advantage	Disadvantage
Sputtering [9] uses simultaneous sputtering of two targets ($(In,Ga)_2Se_3$ and CuSe target)	- high deposition rate - large area deposition	- require expensive vacuum equipment and sputtering targets
Selenization [11] uses diluted H_2Se gas after metallic deposition process (high temperature of selenization =575°C)	- large area deposition - rapid deposition process	- toxic H_2Se gas - poor adherence to substrate
Spray pyrolysis [13] uses aqueous solution containing $CuCl_2$, $InCl_3$, $GaCl_3$ and selenourea as the solvent spray on substrate (T_{sub}=300°C-350°C)	- simple and low-cost technique - non-vacuum methods	- various chemical parameters control - high viscosity solvents contain impurities
Electrodeposition [15] uses aqueous solution containing $CuCl_2$, $InCl_3$, $GaCl_3$ and H_2SeO_3. Films were electroplated by applying a constant potential ($T_{solution}$=24°C)	- low-cost technique - low temperature - large area deposition - non-vacuum methods	- various electrodeposition parameters such as pH, potential applied and bath composition

จุฬาลงกรณ์มหาวิทยาลัย
Chulalongkorn University

Methods	Advantage	Disadvantage
Co-evaporation evaporate Cu, In, Ga and Se atoms simultaneously		
Single-stage [20]	- simple evaporation method - constant substrate temperature	- small columnar grains - rough surface
Two-stage [20]	- large columnar grain - constant substrate temperature	- rough surface - both small and large columnar grains
Three-stage [17-19]	- good uniformity - large columnar grains and smooth surface - large area deposition - achieve the highest efficiency	- limit for lab scale - complicated processing step - use more materials and times

1.3 The fabrication of Ga-grading profiles

The variation of bandgap energy due to Ga-grading can be achieved by the three-stage process. The increase of Ga contents at the front or the back contact or both sides lead to a normal and a double-grading, respectively. When Ga contents increase, the bandgap energy of CIGS material also increases accordingly.

Thus, the fabrication of Ga-grading profiles was widely investigated by the three-stage process from several research groups as followed.

In 1994, M.A. Contreras, et al. from National Renewable Energy Laboratory (NREL) [21] studied Ga-grading profiles deposited by the three-stage co-evaporation process. They indicated that both normal and double grading were observed as a function of depth profile. In case of back grading, the conduction band (CB) edge was raised toward the back surface by increasing Ga contents. It was found that the carriers can be collected and moved toward the p-n junction by the back surface field (BSF). For front grading, high photon energy from shorter spectrum ranges could be absorbed at the front surface. The highest efficiency for the double grading profile was 16.8%.

In 2001, T. Dullweber, et al. from Stuttgart, Germany [22] suggested that the carrier recombination may be reduced by increasing conduction band (CB) edge resulting in short-circuit current improvement. In case of increasing bandgap at the front surface, open-circuit voltage was also improved. Thus, the solar cell performances was controlled via Ga/In and S/Se grading during the deposition. The highest efficiency for graded-bandgap device was 16.7%.

In 2011, S. Schleussner, et al. from Uppsala University, Sweden [23] studied various double grading profiles deposited by the multi-stage process that applied from the three-stage process. The bandgap could be engineered by varying the evaporation profiles. It was found that the double grading showed improvement in both short-circuit current and open-circuit voltage as well as enhancement of more carriers at long wavelengths. Moreover, they suggested that the exceeding Ga gradient on the front side might limit short-circuit current which would cause poor device performances. The highest efficiency for the double grading device was 16.4%.

For previous studies, Ga-grading profiles have been successfully investigated by the three-stage co-evaporation process. From such process, it was a rather complicated process to obtain CIGS absorber layer and bandgap grading and could not naturally be obtained by this technique. In addition, the three-stage co-evaporation process consumes a lot of materials, e.g. Cu, In, Ga and Se, as well as the deposition time. To find the optimum process, CIGS absorber can be fabricated by CIS/CGS bilayer systems. In 2003, O. Lundberg, et al. from Angstrom Solar Center, Uppsala

University, Sweden [24] studied the inter-diffusion of In and Ga in polycrystalline CIGS thin film by growth of CGS/CIS and CIS/CGS bilayers under Cu-rich and Cu-poor with and without sodium conditions. It was found that the diffusion would proceed via vacant metal sites without sodium. Two years later, O. Lundberg, et al. [25] studied the effect of Ga-grading at the back surface on CIGS thickness reduction. It was found that the solar cell performances of reduced thickness down to 0.5 μm were enhanced at 2.5% compared with homogenous CIGS absorber layer due to assistant of the back surface field. Thus, thinner thickness could be employed for less materials and time used in the deposition process.

However, in my work, the deposition of CGS/CIS, CIS/CGS bilayer as well as CGS/CIS/CGS trilayer absorbers are proposed for the fabrication of CIGS thin film solar cells in order to reduce the materials and time used in the process and induce the variation of Ga leading to the bandgap grading and thus increasing efficiency of the devices by enhancing either the open-circuit voltage or short-circuit current density. The efficiency and other parameters of the devices fabricated from the bilayer and trilayer absorbers are investigated in comparison to the reference device using the three-stage deposition process.

1.4 Objectives

จุฬาลงกรณ์มหาวิทยาลัย
CHULALONGKORN UNIVERSITY

1) To prepare the homogeneous bandgap CIGS thin film solar cells using the three-stage process as a reference device.
2) To study the effect of solar cell performances for normal grading using CGS/CIS and CIS/CGS bilayer systems.
3) To study the effects of solar cell performances for double grading using CGS/CIS/CGS trilayer absorbers as well as the thickness reduction.
4) To compare the solar cell performances between the reference device and the Ga-grading devices.
5) To compare the materials and time used in various deposition processes as well as various thickness reductions.

1.5 Scope of this dissertation

This dissertation consists of six chapters. Chapter II describes the theoretical backgrounds of CIGS thin film solar cells such as a p-n junction of solar cell, band structure, phase diagram and the calculation of evaporation rates. Chapter III explains the device fabrications and general characterization processes of the CIGS solar cells. Chapter IV shows the results of optimization of the three-stage deposition process for the CIGS solar cells. Chapter V describes the results of CIGS solar cells obtained from the bilayer and trilayer fabrication processes that demonstrate the results of the bandgap grading. Finally, chapter VI is the conclusion of this dissertation.

CHAPTER II
THEORETICAL BACKGROUND

2.1 General properties of $Cu(In,Ga)Se_2$

$CuIn_{1-x}Ga_xSe_2$ or CIGS is an alloyed semiconducting material in I-III-VI_2 groups, where I = Cu, III = In, Ga and VI = S or Se. The crystal structure of CIGS is chalcopyrite structure. The two unit cells of zincblende structure in II-VI groups are formed to be tetragonal chalcopyrite structure with $I\bar{4}2d$ space group. Half of Zn (II) atoms are replaced by Cu (I) atoms and another half are replaced by In and Ga (III) atoms. Thus, Cu (I) and In, Ga (III) atoms share four bonds with Se (VI) atoms, as illustrated in Figure 1. However, the ratio of the lattice constants, *c*/*a*, is not exactly two due to tetragonal distortion in chalcopyrite material [26]. In addition, the bandgap energy of CIGS crystal also depends on lattice constant *a* as seen in Figure 2.

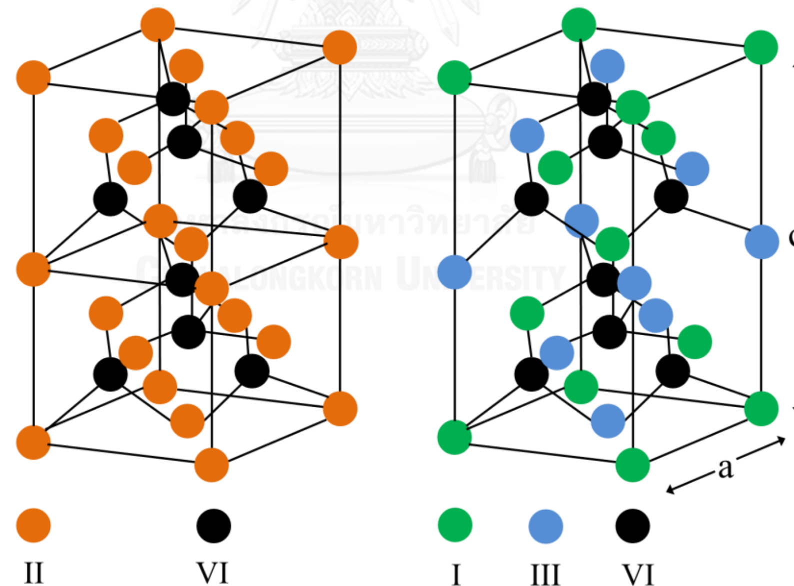

Figure 1 The crystal structures of chalcogenide compound; (a) zincblende structure and (b) chalcopyrite structure.

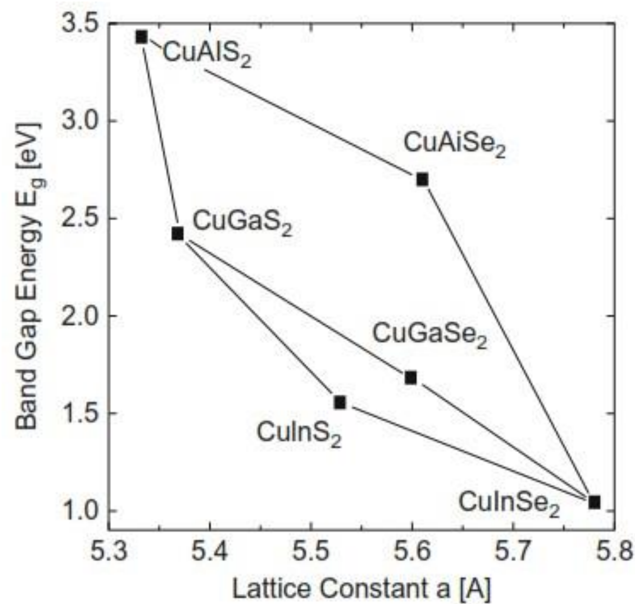

Figure 2 The bandgap energy of the Cu(In,Ga,Al)(Se,S)$_2$ alloy system as a function of lattice constant a.

Table 2 Lattice mismatch values (ε) of CGS/CIS and CIS/CGS bilayers

Compounds	*a* (Å)	*c* (Å)	*ε*
CGS	5.6140	11.0220	-
CIS	5.7815	11.6188	-
CGS/CIS	-	-	0.0290
CIS/CGS	-	-	-0.0298

In case of *epitaxial* bilayers by the deposition of CIS single layer on top of CGS single layer or vice versa, the lattice mismatch between both CIS and CGS layer also contributes to strain at the interface between the two layers. The lattice

parameters a for CGS and CIS are 5.6140 Å and 5.7815 Å, respectively [27]. Thus, the strain due to lattice mismatch can be expressed in terms of the lattice constants by

$$\varepsilon = \frac{a_{bottom} - a_{upper}}{a_{bottom}}, \qquad (1)$$

where ε is a lattice mismatch between the two layers, a_{bottom} is lattice parameter a of the bottom layer and a_{upper} is lattice parameter a of the upper layer.

The negative value of ε refers to compressive strain and positive value refers to tensile strain. The lattice mismatch of bilayers is shown in Table 2. However, this might not be the case for the polycrystalline bilayer CIS/CGS or trilayer CGS/CIS/CGS since the constituents are most likely to form an alloyed CIGS with homogeneous or non-homogeneous distribution of In and Ga. One can also expect observe the complete coalescence of the CIS and CGS x-ray diffraction peaks when In and Ga are uniformly distributed in the CIGS, while the incomplete coalescence can be observed in the case that In and Ga have some distribution gradient due to their different diffusivities as shown by the schematic in Figure 3 [20].

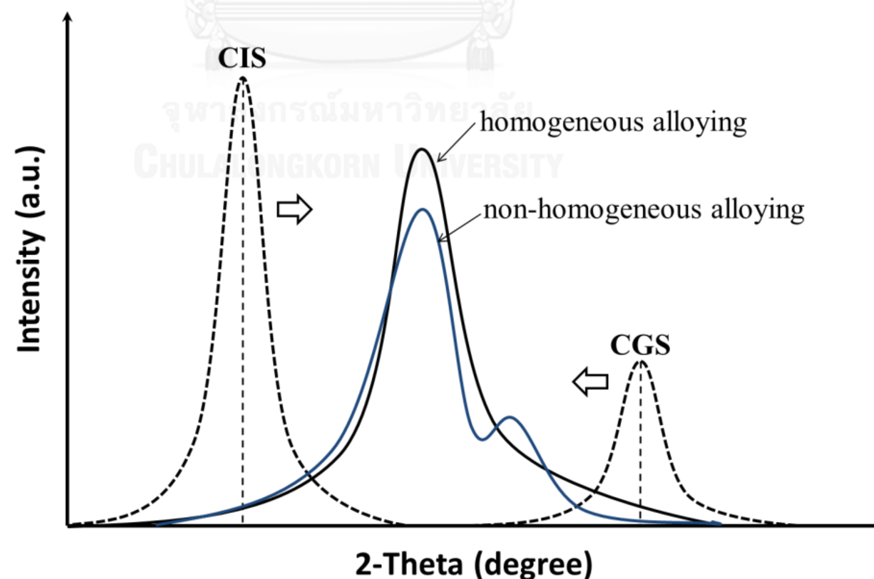

Figure 3 The alloyed CIGS with homogeneous or non-homogeneous distribution of In and Ga.

CHULALONGKORN UNIVERSITY

Another important property of CIGS is its direct bandgap energy and high optical absorption when compared with other materials [21]. The bandgap energy of CIGS can be adjusted by varying Ga composition or x = [Ga]/([In]+[Ga]), in the ranges of 1.04-1.68 eV depending on x value. The variation of bandgap energy of CIGS is given by

$$E_{g,CIGS}(x) = (1-x)E_{g,CIS} + xE_{g,CGS} - bx(1-x) \quad (2)$$

where b = 0.15-0.24 eV is the bowing parameter [28].

When Ga composition is increased, the bandgap energy of CIGS is also increased by rising of conduction band (CB) that has a direct effect on built-in potential corresponding to open-circuit voltage enhancement of the solar cells. The suitable values of bandgap energy for uniform CIGS material are in the range of 1.1-1.5 eV under solar radiation at AM1.5, as shown in Figure 4 (a) and the absorption coefficient of various materials related with the photon energy can be demonstrated in Figure 4 (b).

จุฬาลงกรณ์มหาวิทยาลัย
Chulalongkorn University

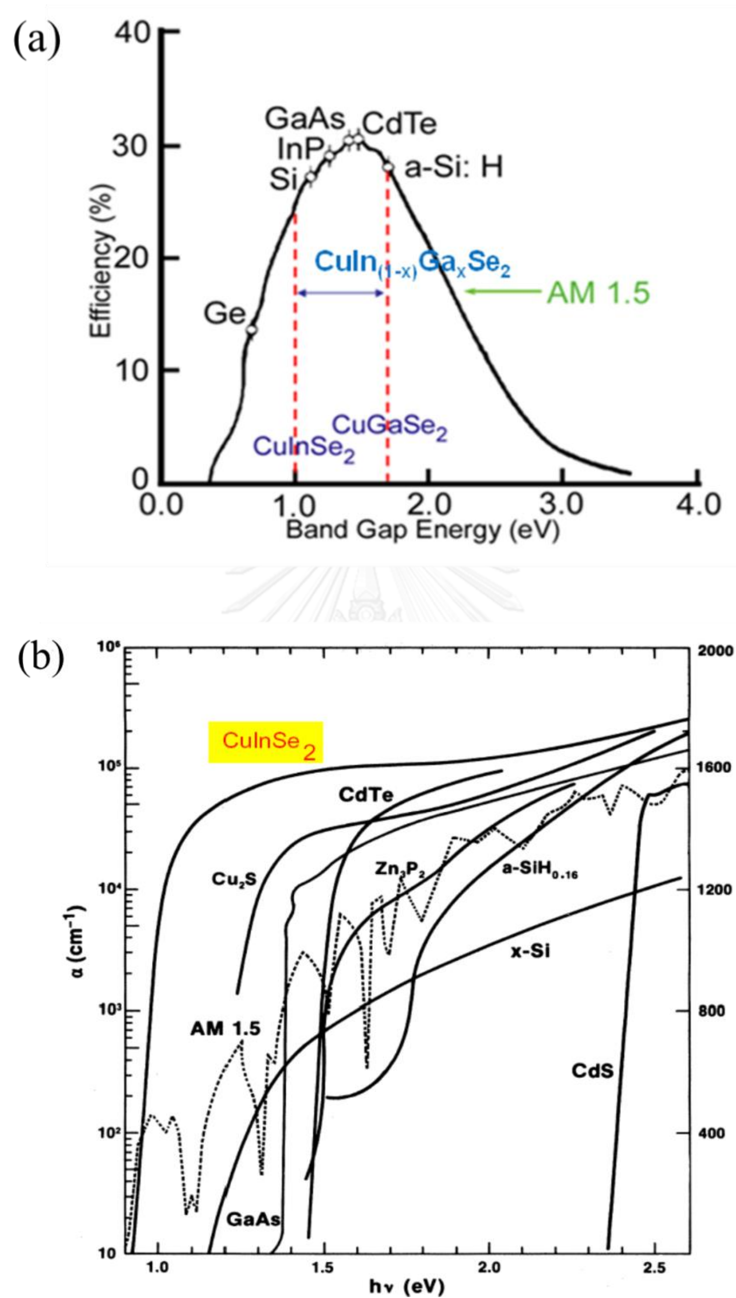

Figure 4 (a) Theoretical efficiencies of various solar cell materials as a function of bandgap energy at AM1.5. (b) Absorption coefficient of $CuInSe_2$ material compared with the variation of photovoltaic materials.

2.2 Phase formation of $Cu(In,Ga)Se_2$ materials

2.2.1 Phase diagram of Cu-In-Se system

Phase diagram of Cu-In-Se system associates with Cu_2Se-In_2Se_3 *pseudobinary* compounds. $CuInSe_2$ (CIS) chalcopyrite structure usually refers to α-CIS phase when Cu concentration is in the ranges of 24.0-24.5%, as depicted in the red region. Firstly, Cu_2Se refers to Cu-rich or [Cu]/[In]≥1. For Cu-deficient or [Cu]/[In]<1, there are many phases such as β-CIS ($CuIn_3Se_5$), γ-CIS ($CuIn_5Se_8$) and In_2Se_3 which are called as order vacancy compounds (OVC) or order defect compounds (ODC). Cu vacancies (V_{Cu}) can be occupied by In atoms (In_{Cu}). Lastly, stoichiometric compound or [Cu]/[In]=1 is a combination of slightly Cu-deficient of α-CIS and Cu_2Se. The sphalerite structure of δ-CIS is an unstable phase at room temperature. In addition, quasi-liquid phase of Cu_2Se on the film surface can enhance high diffusivities of In and Ga into Cu_2Se that could lead to larger grain growth of CIGS film. The phase diagram of $CuInSe_2$ compounds are shown in Figure 5 [29].

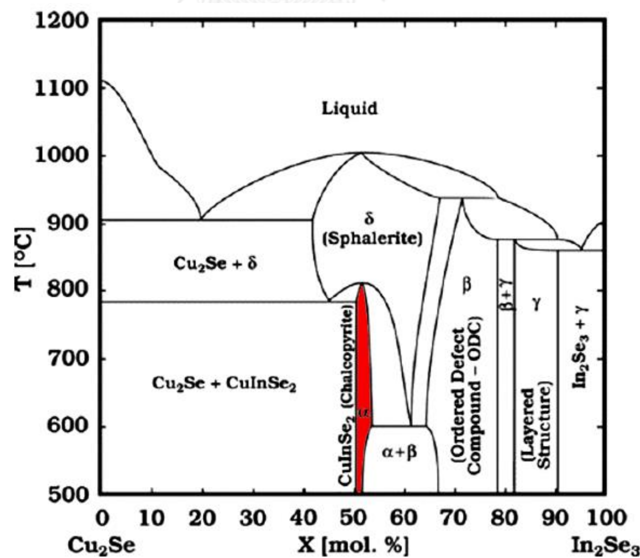

Figure 5 Phase diagram along the Cu_2Se-In_2Se_3 psudobinary of $CuInSe_2$ compound.

2.2.2 Phase diagram of Cu-Ga-Se system

According to $CuGaSe_2$ (CGS) compounds, the phase formation of Cu_2Se-Ga_2Se_3 pseudobinary is less considered than Cu_2Se-In_2Se_3 pseudobinary because

$CuInSe_2$ is the historical development of $Cu(In,Ga)Se_2$ semiconducting compounds. CGS is also a chalcopyrite structure that occupied Cu-poor composition (20.7%). The phase transition under Cu-poor condition of Cu-Ga-Se is less complexity than Cu-In-Se system. In addition, Ga_2Se_3 phase seems to be a defect zincblende structure under Cu composition more than 10%. The melting point of $CuGaSe_2$ and $CuInSe_2$ are approximately 1080°C and 980°C, respectively. Thus, it is difficult to deposit high quality of $CuGaSe_2$ thin films because $T_{substrate}/T_{melting}$ ratio of $CuGaSe_2$ is less than $CuInSe_2$ at the same temperature. Phase diagram of Cu_2Se-Ga_2Se_3 pseudobinary is provided in Figure 6 [29].

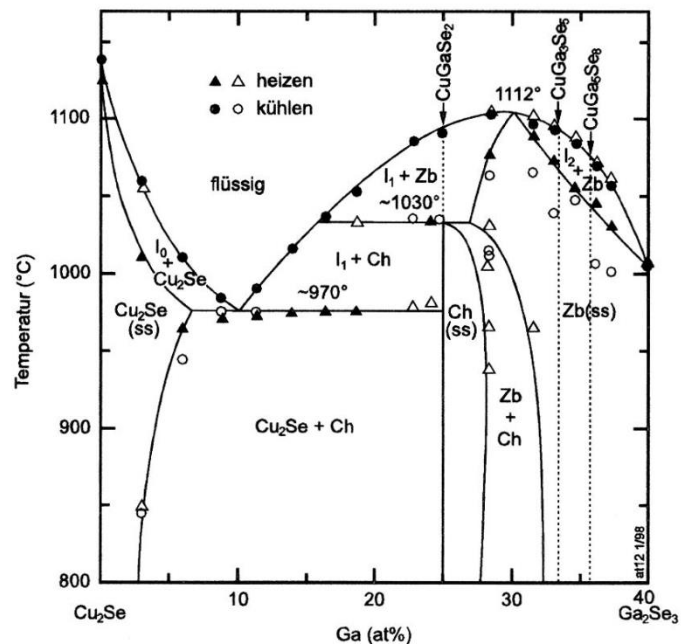

Figure 6 Phase diagram along the Cu_2Se-Ga_2Se_3 psudobinary of $CuGaSe_2$ compound.

2.2.3 Phase diagram of Cu-In-Ga-Se system

The pseudoternary of Cu_2Se-In_2Se_3-Ga_2Se_3 composition diagram at room temperature is depicted in Figure 7 [29]. The existence of α single phase expands with increasing [Ga]/[In] composition toward Cu-poor composition. The phase formation energy of Ga neutral defect complex ($2V_{Cu}$+Ga_{Cu}) is higher than In neutral defect complex ($2V_{Cu}$+In_{Cu}). The quaternary of CIGS is dominated in Ch+P1+Zb phase domain. The notations; Ch refers to α phase (Chalcopyrite), P1 refers to β phase

(derivative of chalcopyrite), P2 refers to γ phase (layered structure) and Zb refers to δ phase (zincblende, unordered). Thus, the chalcopyrite phase should consist of Ga composition (x value) at least 0.25 for efficiency enhancement.

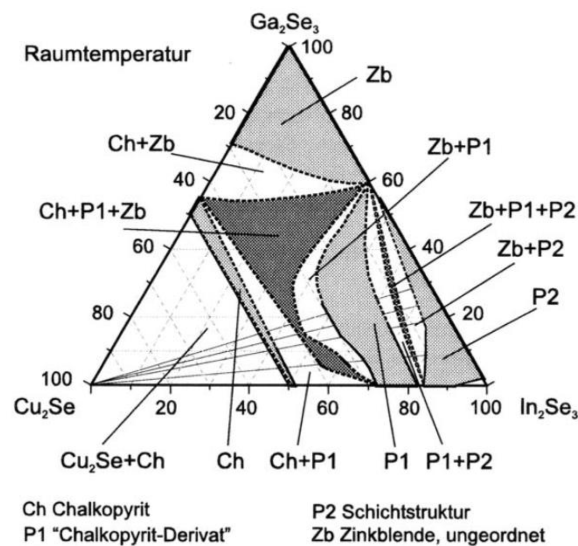

Figure 7 Isothermal quasi-ternary Cu_2Se-In_2Se_3-Ga_2Se_3 phase diagram of $Cu(InGa)Se_2$ compounds at room temperature.

2.3 The electrical properties of solar cells

2.3.1 J-V characteristics of solar cells

The current density-voltage (J-V) measurement is the common tool for solar cell characterization. J-V characteristic is operated under dark (without illumination) and light (with illumination) conditions by applying an external voltage (V) to the devices. Then, the four basic parameters to identify the solar cell performances consist of the short-circuit current density (J_{sc}), the open-circuit voltage (V_{oc}), the fill factor (FF) and the efficiency (η). An example of J-V characteristic curve of a solar cell is depicted in Figure 8.

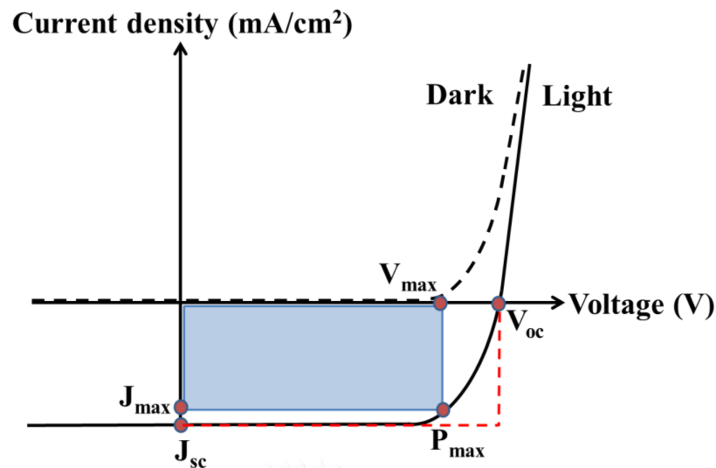

Figure 8 J-V characteristic curve of a solar cell.

To simply illustrate the ideal of solar cell, one-diode model can be considered. Under illumination with standard condition 100 mW/cm^2 (AM1.5) or zero bias voltage (V=0), J-V characteristic is described by Shockley diode equation;

$$J = J_0\left[\exp\frac{qV}{nk_BT} - 1\right] - J_L, \tag{3}$$

where J_L is the photocurrent density generated from the device or the short-circuit density *(J_{sc})* that has an opposite direction to J_0- the reverse saturation current density of a diode under the dark condition, n is the diode ideality factor and k_B is the Boltzmann constant.

There are other two important factors in a real solar cell; series resistance (R_s) and shunt resistance (R_{sh}). Then, the total current is given by

$$J = J_0\left[\exp\left(\frac{q(V - JR_s)}{nk_BT}\right) - 1\right] + \frac{V - JR_s}{R_{sh}} - J_L, \tag{4}$$

Where R_s indicates the resistance of the current paths in the device and contacts, R_{sh} is the shunt resistance of the current in parallel paths that has an effect of current flow across the p-n junction. Thus R_s should be as low as possible ($R_s \rightarrow 0$) and R_{sh} is needed to be very high *($R_{sh} \rightarrow \infty$)* for good devices. The equivalent circuit of an illuminated solar cell is shown in Figure 9.

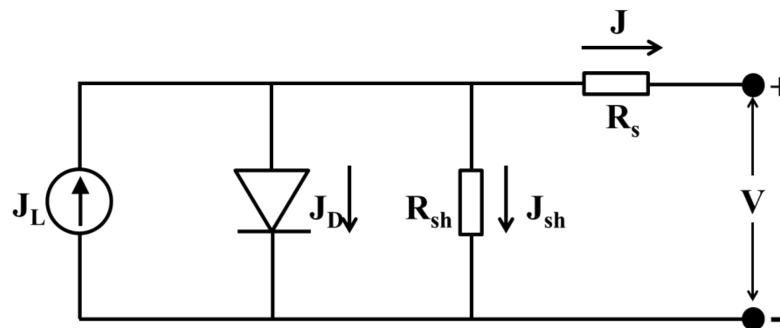

Figure 9 One-diode equivalent circuits of an illuminated solar cell.

The open-circuit voltage (V_{oc}) is related to the bandgap energy. When the current cannot flow (J=0, $R_s \rightarrow 0$ and $R_{sh} \rightarrow \infty$), the open-circuit voltage can be written as

$$V_{oc} = \frac{k_B T}{q} \ln\left(1 + \frac{J_L}{J_0}\right). \quad (5)$$

The fill factor (FF) describes to the performance of the p-n junction to that of the square of J-V curve. As seen in Figure 8, The FF is the ratio of the maximum output power to the obtained value of J_{sc} and V_{oc} (the area of solid line square to the area of dash line square), i.e.

$$FF = \frac{J_{max} \times V_{max}}{J_{sc} \times V_{oc}}. \quad (6)$$

Then, the energy conversion efficiency (η) is the ratio of the input power (light incident) and the output power (electrical power). P_{in} is the incident power that equal to $P_{AM1.5}$ = 100 mW/cm^2 [30, 31], i.e.

$$\eta = \frac{J_{max} \times V_{max}}{P_{in}} = \frac{FF \times J_{sc} \times V_{oc}}{P_{in}}. \quad (7)$$

จุฬาลงกรณ์มหาวิทยาลัย
CHULALONGKORN UNIVERSITY

2.3.2 The p-n junction of solar cells

CIGS thin film solar cell has a heterojunction band structure of two semiconducting materials between n-type ZnO-window layer and p-type CIGS-absorber layer. The heterojunction band diagram of CIGS thin film solar cell is illustrated in figure 10 [30]. The advantage of unequal bandgap energy (E_g) is an attractive device to closely match with the solar spectrum. Thus, the unequal bandgap consist of four different semiconducting materials by means of placing larger bandgap of ZnO(Al) on the front side or photon entrance. When the incident light is illuminated on ZnO(Al) window layer, photons with energy equal or greater than the bandgap energy of CIGS material are absorbed. Thus, electron-hole pairs are generated. The electric fields at the junction separate negative charges to the opposite direction and positive charges to the direction of the electric fields. Electrons are transported to the n region of ZnO window layer toward Al-grid, and holes are transported to the p region of CIGS to Mo back contact. The metallic contact layers at the front (Al-grid) and the back (Mo) contacts conduct the carrier to external load. The unfavorable electrons can be recombined at the interface or the absorber layer by the recombination paths. The recombination paths may usually occur from defect state within the CIGS absorber layer or the interface regions. The recombination paths are appeared at (A) CdS/CIGS interface recombination, (B) space charge region recombination, (C) bulk recombination or (D) back contact recombination [32] as seen in Figure 10. To reduce the recombination, bandgap grading of p-CIGS material at the front or the back surface may be applied. In addition, increasing bandgap at the back surface may induce the additional electric field or back surface field (BSF) to reduce the carrier recombination and improve the carrier collections in the solar cell.

จุฬาลงกรณ์มหาวิทยาลัย
Chulalongkorn University

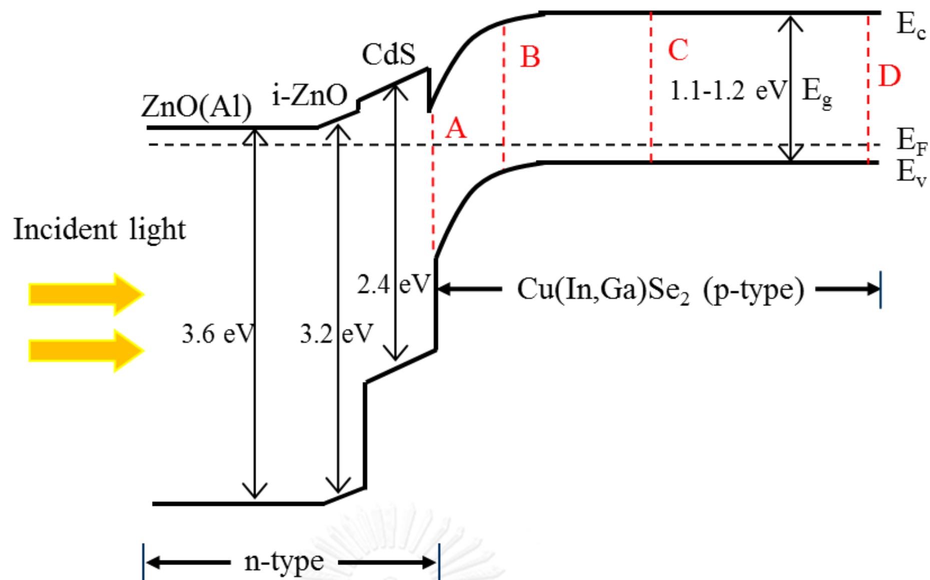

Figure 10 Energy band diagram of heterojunction CIGS thin film solar cell with recombination paths; A = interface recombination, B = space charge region recombination, C = neutral bulk recombination and D = back contact recombination.

2.3.3 Normal and double Ga-grading of CIGS solar cells

The increase of Ga contents at the front or the back surface, the conduction band edge of the p-CIGS absorber layer is increased leading to bandgap grading. Normal grading refer to increasing Ga contents at the front or the back surface and double grading refer to increasing Ga contents at both sides. In general, the uniform bandgap has no drift forces outside the depletion region. Thus, carriers are only generated at the depletion region. Moreover, the generated electrons may be recombined at the depletion region or at the back surface of the absorber layer.

For this reason, bandgap grading could be fabricated to reduce the carrier recombinations. For increasing conduction band edge at the back surface, more carriers can be collected by the back surface field (BSF). Thus, the short-circuit current density can be improved. In case of increasing conduction band edge at the front surface, the open-circuit voltage can be improved by increasing built-in voltage and it can enhance the high photon energy to be absorbed in the absorber layer. Thus, double grading may improve both the open-circuit voltage and the short-circuit

current density [32]. In case of improving the efficiency of thinner absorber layer, back grading is the important factor to maintain high performances by the back surface field assistant [25].

The external electric field ($\vec{\varepsilon}$) due to increasing bandgap energy can be described by [33].

$$\vec{\varepsilon} = \frac{1}{e}\frac{d\Delta E_g}{dx}\hat{x}, \tag{8}$$

where ΔE_g is the bandgap energy by Ga-grading over the distance x. The schematic diagrams of various Ga-graded bandgap conditions are illustrated in Figure 11 (a)-(d).

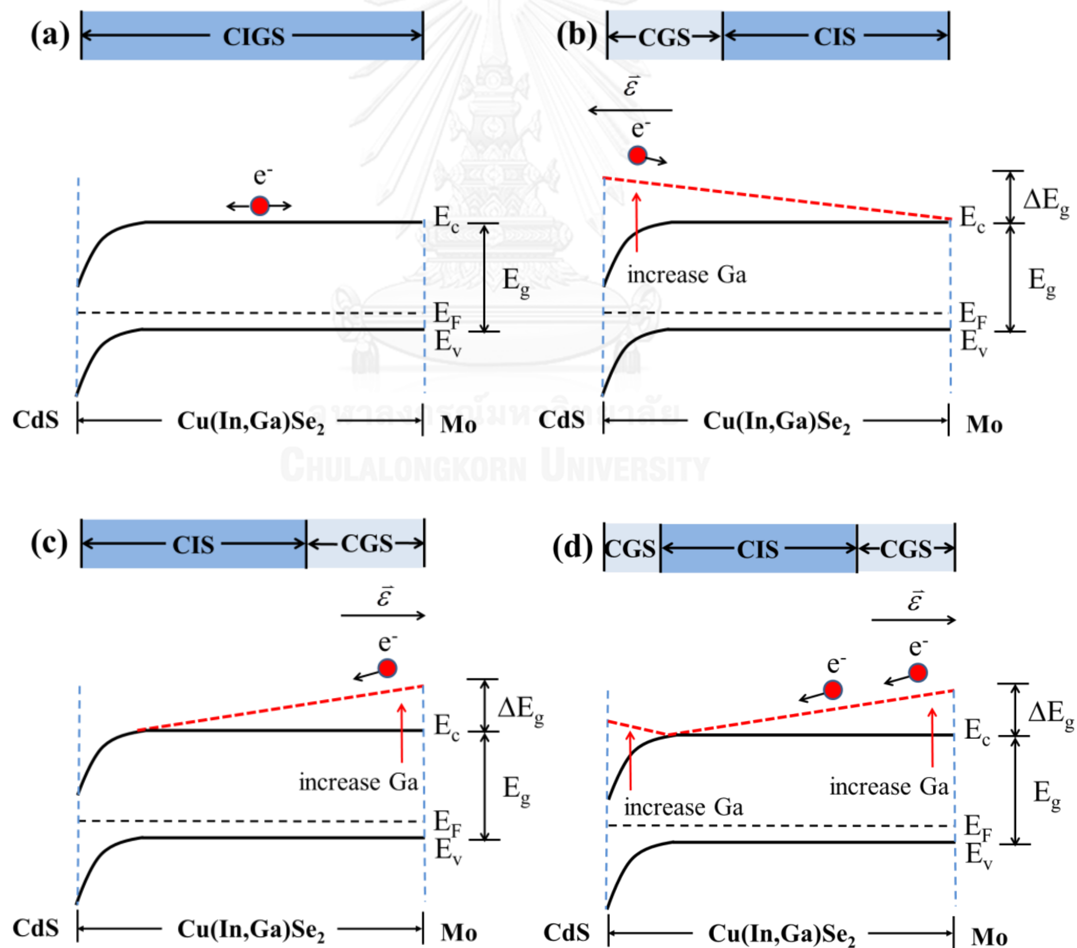

Figure 11 Schematic diagrams of the bandgap energy of $Cu(In,Ga)Se_2$ (a) uniform bandgap (b) front grading, (c) back grading and (d) double grading.

2.4 CIGS thin film deposition by co-evaporation method

In this work, CIGS absorber layers are fabricated by the multi-sources co-evaporation techniques without substrate rotation. To obtain bandgap grading profiles, CIGS absorbers are deposited by CGS/CIS, CIS/CGS bilayers and CGS/CIS/CGS trilayers for the normal and double grading profiles, which the uniform bandgap is deposited by the three-stage process. The elemental sources of Cu, In, Ga and Se are evaporated from the Knudsen cells (K-cells). To obtain the crystalline quality of CIGS absorber layer, the base pressure of this system is kept approximately 2 x 10^{-6} Torr. A quartz crystal monitor (QCM) is used to calibrate the evaporation rates for calculation of the evaporation profiles. Moreover, a pyrometer is used to monitor thin film deposition by observing the radiation from the film surface. The schematics and the picture of the evaporation system are shown in Figure 12 (a), (b).

2.4.1 The three-stage process

High efficiency CIGS thin film solar cells are usually fabricated by the three-stage co-evaporation process. In the first stage, In, Ga and Se were evaporated at lower substrate temperature to form $(In,Ga)_2Se_3$ precursor layer. Then, in the second stage, Cu and Se were evaporated on top of $(In,Ga)_2Se_3$ layer at higher substrate temperature until Cu-rich (y>1) as obtained. This stage reverses the γ-CIGS and β–CIGS phase formation to be α–CIGS phase. Finally, In, Ga and Se were evaporated until Cu-rich composition converted to Cu-poor composition with observed by the End Point Detection (EPD). Se was maintained about 30 minutes for surface modification. Moreover, the ratio of [Ga]/([In]+[Ga]) or x ratio is usually set at 0.37 for entire deposition process. The total time was ~120 minutes for CIGS thickness of 1.8 μm. The schematic of the three-stage co-evaporation process is illustrated in Figure 13. The parameters for a deposition of CIGS by the three-stage process are provided in Table 3.

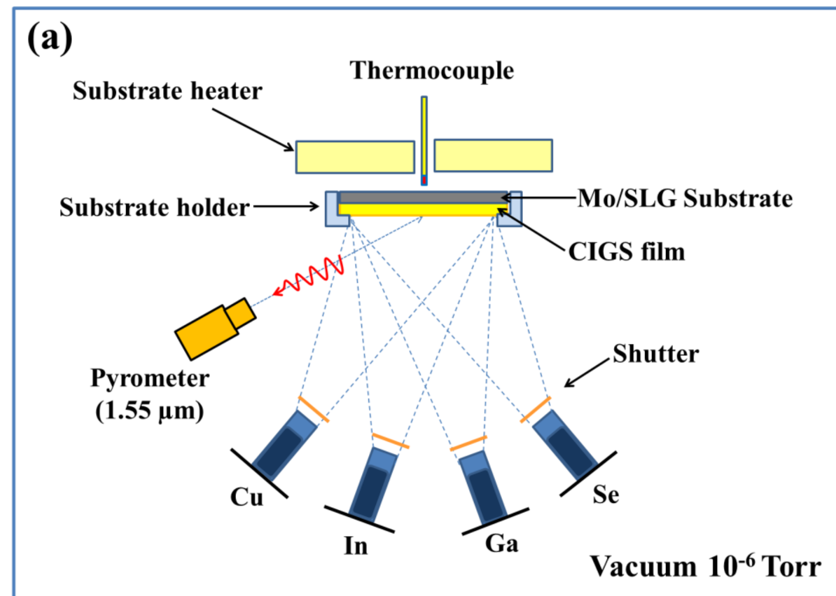

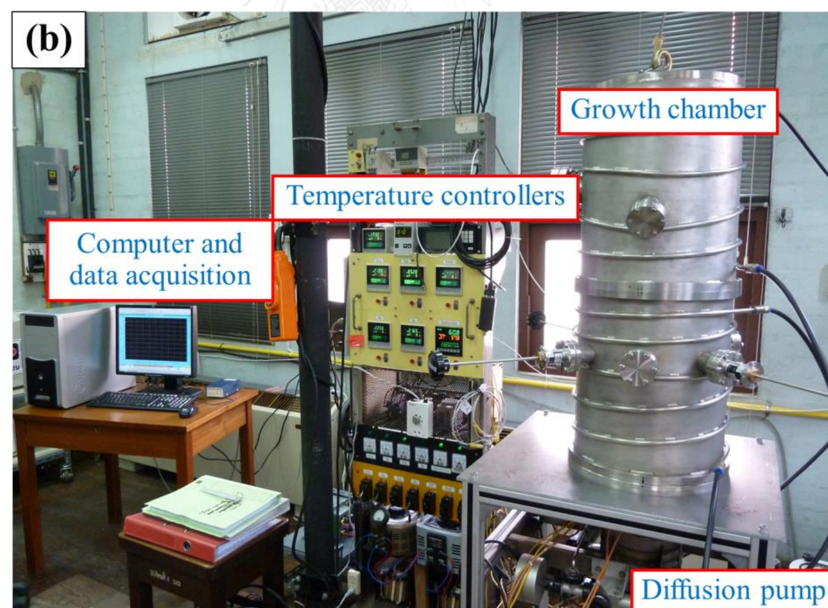

Figure 12 (a) The schematic illustration inside the vacuum growth chamber. (b) The photograph of the co-evaporation systems including the growth chamber, controller systems, real-time monitor and diffusion pump.

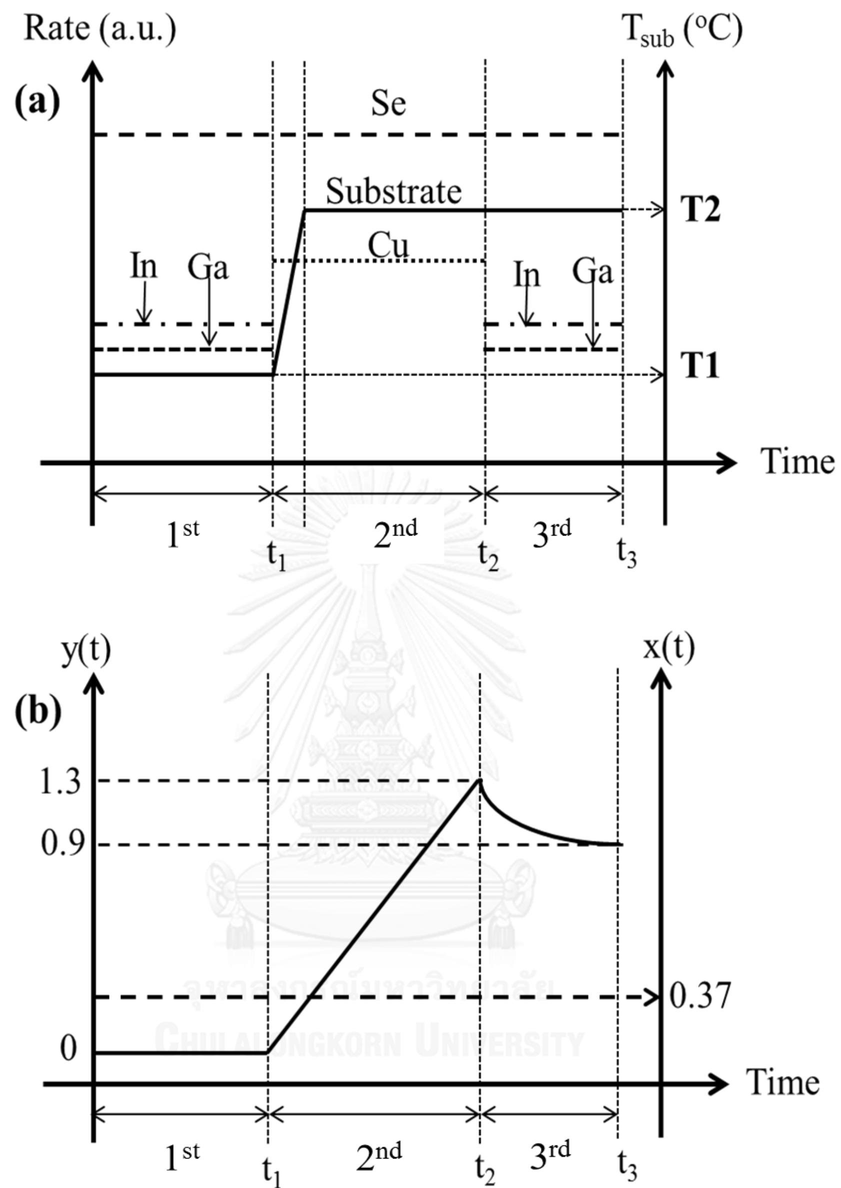

Figure 13 Schematic diagram of (a) The three-stage growth profile by varying low substrate temperature at the 1st stage (T1) and then, varying the increased substrate temperature at the 2nd stage and the 3rd stage (T2). (b) Thin film composition for CIGS growth in the three-stage process, y=[Cu]/([In]+[Ga]) is shown in the solid line, x=[Ga]/([In]+[Ga]) is shown in the dash line.

Table 3 The parameters for a deposition of CIGS by the three-stage.

Parameters	Data
	CIGS
Thickness	1.8 μm
Time (t_{Cu})	50 min
Time ($t_{1,3}$)	40, 16 min
x	0.37
$y(t_1)$	1.3
$y(t_2)$	0.9

The three-stage process, the first stage starts with the ratio [Cu]/([In]+[Ga]) equal zero (y=0) and gradually increases to Cu-rich (y>1) composition at the end of second stage. It can be written as

$$y(t) = \frac{y(t_1)}{t_1} \cdot t, \tag{9}$$

where *y(t)* is the ratio of [Cu]/([In]+[Ga]) in the second stage, *t* is the end time for the second stage, $y(t_1)$ is the ratio of [Cu]/([In]+[Ga]) in the first stage and t_1 is the total time in the first stage. For the end of the second stage, y becomes Cu-poor (y<1) and can be written as

$$y(t) = \frac{y(t_1)}{t} \cdot t_1, \tag{10}$$

where *y(t)* is the ratio of [Cu]/([In]+[Ga]) in the third stage, *t* is the end time for the third stage, $y(t_1)$ is the ratio of [Cu]/([In]+[Ga]) in the second stage and t_1 is the total time in the second stage.

To obtain the CIGS thin film deposited by the three-stage process, bilayer and trilayer processes, the relationship between the evaporation rate and the temperature of the elemental source is given by

$$\ln(r) = a(\frac{1}{T}) + b, \tag{11}$$

จุฬาลงกรณ์มหาวิทยาลัย
CHULALONGKORN UNIVERSITY

where r is the evaporation rate (Å/s), T is the source temperature, a and b are the parameters obtained by the least-square fit. The example graphs of the evaporation rate with temperature of each elemental source can be seen in Figure 14.

Firstly, the evaporation rate of Cu (r_{Cu}) is calculated from eq. 12 so that the thickness of Cu can be derived from eq. 13.

$$r_{Cu} = \frac{d_{Cu}}{t_{Cu}}, \tag{12}$$

$$d_{Cu} = \frac{N_{Cu} \cdot (M_{Cu}) \cdot (\rho_{CIS} \cdot (1-x) + \rho_{CGS} \cdot x)}{N_{CIGS} \cdot (M_{Cu} + M_{In} \cdot (1-x) + M_{Ga} \cdot x + 2 \cdot M_{Se}) \cdot \rho_{Cu}} \cdot d_{CIGS}, \tag{13}$$

where r_{Cu} is the deposition rate of Cu element (Å/s),

d_{Cu} is the thickness of Cu element (Å),

t_{Cu} is the total time for Cu element deposition,

N_{Cu} and N_{CIGS} are the number of Cu atoms and CIGS molecules, so the ratio of

N_{Cu} / N_{CIGS} equal unity,

x is the ratio of [Ga]/([In]+[Ga]),

M_i is the molecular mass of material i,

ρ_i is the density of material i

d_{CIGS} is the thickness of CIGS thin film (Å)

The most important thing for CIGS thin film deposition is the optimization of x and y values that have an effect of the bandgap and thin film morphology, respectively. Then, the rate of In (r_{In}) and Ga (r_{Ga}) lead to the values of x and y;

$$x = \frac{[Ga]}{[In]+[Ga]} = \frac{N_{Ga}}{N_{In}+N_{Ga}}, \quad (14)$$

$$y = \frac{[Cu]}{[In]+[Ga]} = \frac{N_{Cu}}{N_{In}+N_{Ga}}. \quad (15)$$

The number of atoms in each material (N_i) can be calculated by

$$N_i = \frac{\rho_i \cdot V \cdot N_A}{M_i} = \rho_i \cdot M_i^{-1} \cdot d_i A \cdot N_A. \quad (16)$$

Thus, the values of x and y in unit area of CIGS thin film can be written in eq. 17 and eq. 18, respectively;

$$x = \frac{\rho_{Ga} \cdot M_{Ga}^{-1} \cdot d_{Ga} \cdot A \cdot N_A}{(\rho_{In} \cdot M_{In}^{-1} \cdot d_{In} + \rho_{Ga} \cdot M_{Ga}^{-1} \cdot d_{Ga}) \cdot A \cdot N_A}, \quad (17)$$

$$y = \frac{\rho_{Cu} \cdot M_{Cu}^{-1} \cdot d_{Cu} \cdot A \cdot N_A}{(\rho_{In} \cdot M_{In}^{-1} \cdot d_{In} + \rho_{Ga} \cdot M_{Ga}^{-1} \cdot d_{Ga}) \cdot A \cdot N_A}, \quad (18)$$

where A is the unit area for thin film deposition, N_A is the *Avogadro's number* = 6.02×10^{23} atoms or molecules. From eqs. 17 and 18 the parameter α_i will be defined as the ratio of density to molecular mass of each element;

$$\alpha_{Cu} = \rho_{Cu} \cdot M_{Cu}^{-1}, \quad (19a)$$

$$\alpha_{In} = \rho_{In} \cdot M_{In}^{-1}, \quad (19b)$$

$$\alpha_{Ga} = \rho_{Ga} \cdot M_{Ga}^{-1}, \quad (19c)$$

where ρ_i is the density and M_i is the molecular mass values of the materials provided in Table 4.

Table 4 Density, molecular mass and α_i parameter of the materials for CIGS thin film deposition.

Material	ρ **(g/cm^3)**	**M(g/mol)**	$\alpha = \rho/M$ **(mole/cm^3)**
Cu	8.96	63.55	0.1410
In	7.31	114.82	0.0637
Ga	5.91	69.72	0.0848
Se	4.79	78.96	0.0607
CIS	5.89	336.29	-
CGS	5.27	291.19	-

จุฬาลงกรณ์มหาวิทยาลัย
Chulalongkorn University

Substituting eqs. $19a$, $19b$ and $19c$ into eqs. 17 and 18 so that the relationship of material thickness can be expressed in eqs. 20, 21 and 22;

$$d_{Ga} \cdot \alpha_{In} + d_{Ga} \cdot \alpha_{Ga} = d_{Cu} \cdot \alpha_{Cu} \cdot \frac{1}{y} = d_{Ga} \cdot \alpha_{Ga} \cdot \frac{1}{x}, \tag{20}$$

$$d_{Ga} = \frac{x}{y} \cdot \frac{\alpha_{Cu}}{\alpha_{Ga}} \cdot d_{Cu}, \tag{21}$$

$$d_{In} = \frac{(1-x)}{y} \cdot \frac{\alpha_{Cu}}{\alpha_{In}} \cdot d_{Cu}. \tag{22}$$

Then, the thickness of the element is proportional to the total deposition time so that eqs. 21 and 22 become eqs. 23 and 24.

$$r_{Ga} = \frac{x}{y} \cdot \frac{\alpha_{Cu}}{\alpha_{Ga}} \cdot r_{Cu}, \tag{23}$$

$$r_{In} = \frac{(1-x)}{y} \cdot \frac{\alpha_{Cu}}{\alpha_{In}} \cdot r_{Cu}. \tag{24}$$

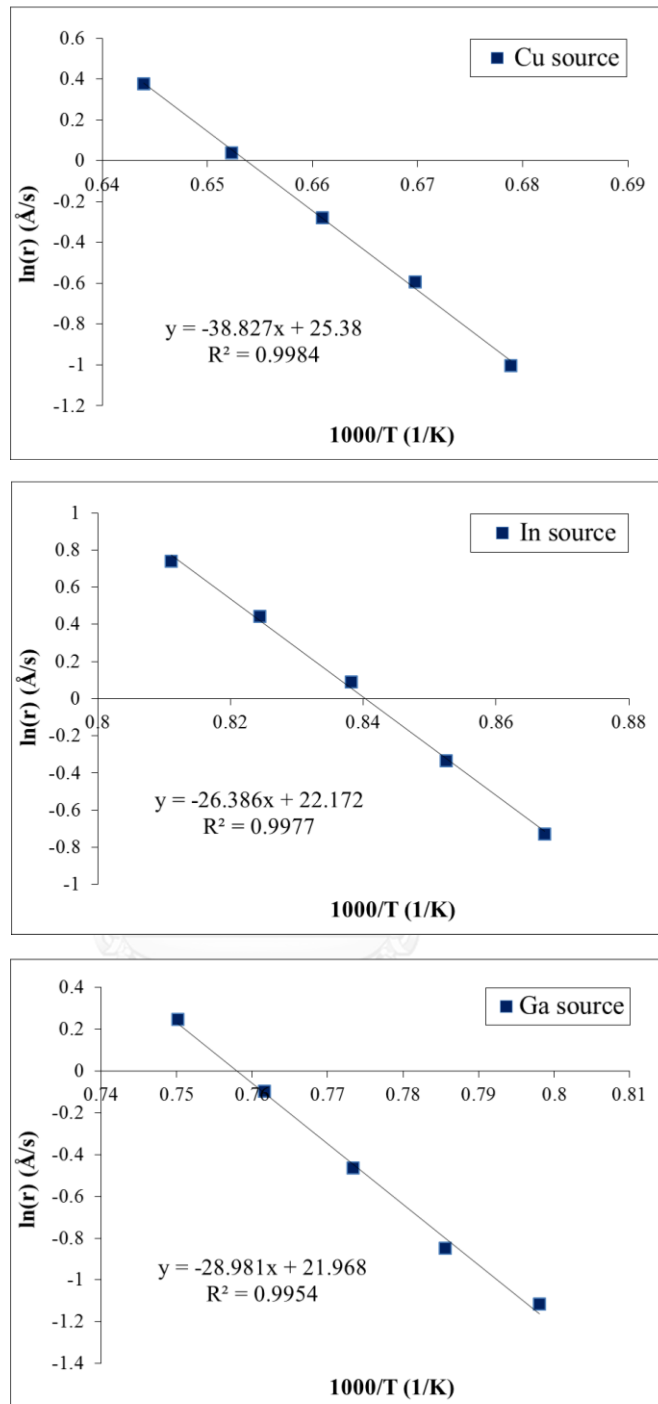

Figure 14 The graph of evaporation rate versus elemental temperature of Cu, In and Ga sources to obtain *a* and *b* parameters by least-square fit which detected by QCM.

2.4.2 The single process

To observe Ga-grading profiles by the bilayer or trilayer processes, the physical properties of $CuGaSe_2$ (CGS) and $CuInSe_2$ (CIS) single layer should be firstly investigated. The depositions of CIS and CGS layers are related to the composition of [Ga]/([In]+[Ga]) or x=0 and x=1, respectively. Cu composition throughout the growth process of CIS and CGS was set as y=0.9 or 10% below stoichiometric ratio to maintain chalcopyrite structure. The substrate temperature was kept constant at 560°C. The growth profile of single layer is shown in Figure 15 and then the parameters for single layer deposition are shown in Table 5

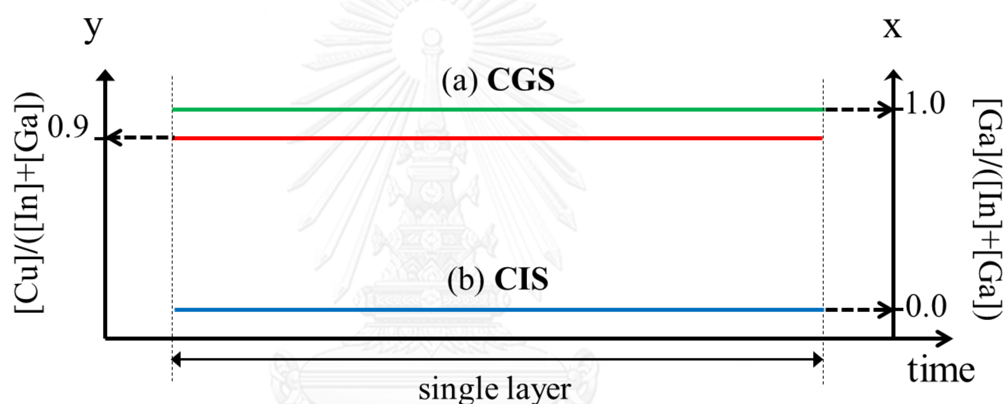

Figure 15 The evaporation profile of single layer process of (a) $CuGaSe_2$ with the ratio of [Ga]/([In]+[Ga]); x=1. (b) $CuInSe_2$ with the ratio of [Ga]/([In]+[Ga]); x=0.

Table 5 The parameters for deposition of CGS and CIS single layer.

Parameters	Data	
	CGS	**CIS**
Thickness	1.8 µm	1.8 µm
Time	60 min	60 min
x	1.0	0.0
y	0.9	0.9

2.4.3 The bilayer process

The bilayer process is the modified evaporation method for CIGS thin film deposition in order to observe the normal grading of CGS/CIS and CIS/CGS bilayers. It is simply the single stage deposition of two or three layers of CIS and CGS. This technique is not complicated as the three-stage process, duration time is shorter and fewer materials are used compared to the three-stage process. The main purpose of this technique is to observe the variations of bandgap by different Ga contents at the front or the back surface. The substrate temperature of the bilayer technique was kept constant at 560°C throughout the deposition process. For this experiment, Cu composition were varied under Cu-rich (y=1.2) and Cu-poor (y=0.9) compositions. The average Ga composition was set at 0.37 as same as the three-stage process with the total thickness of 1.8 μm. The bilayer deposition processes are depicted in Figure 16 (a), (b). Also, the parameters for the bilayer deposition are provided in Table 6.

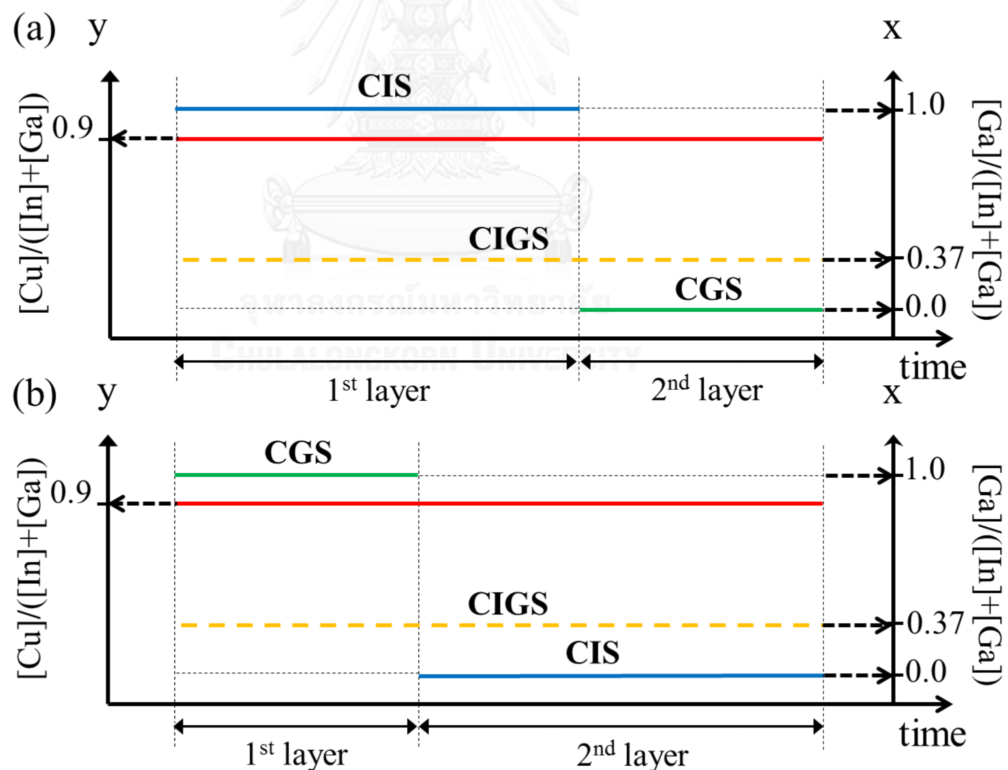

Figure 16 The evaporation profiles of bilayer deposition processes (a) CGS/CIS and (b) CIS/CGS.

Table 6 The parameters for deposition of CGS/CIS and CIS/CGS bilayers.

Parameters	Data	
	CGS	CIS
Thickness	0.67 μm	1.13 μm
Time	24 min	36 min
x	1.0	0.0
y	0.9	0.9

2.4.4 The trilayer process

To observe double grading, CGS/CIS/CGS trilayers is the modified process from the bilayer processes. The addition of CGS thin film layer was applied on top of CIS/CGS bilayers by means of increasing Ga contents both the front and the back surface. The standard thickness of CGS/CIS/CGS trilayers is ~1.8 μm. The substrate temperature of the entire process was kept constant at 560°C. Cu composition is 0.9 and Ga composition is 0.25. To observe the use of less materials and times, thinner thicknesses of CGS/CIS/CGS trilayers are also varied from 1.8 μm, 1.2 μm, 0.8 μm and 0.5 μm. The trilayers deposition profile is shown in Figure 17 and the parameters for CGS/CIS/CGS trilayers deposition are shown in Table 7.

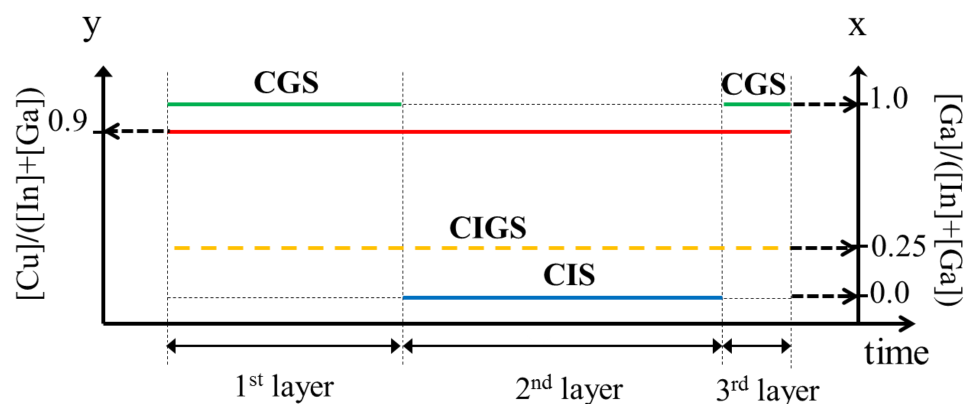

Figure 17 The evaporation profile of trilayers deposition process of CGS/CIS/CGS trilayers.

Table 7 The parameters for deposition of CGS/CIS/CGS trilayers.

Parameters	**Data**		
	CGS (1st layer)	**CIS (2nd layer)**	**CGS (3rd layer)**
Thickness	0.45 μm	1.35 μm	30 nm
Time	24 min	36 min	1.5 min
x	1.0	0.0	1.0
y	0.9	0.9	0.9

จุฬาลงกรณ์มหาวิทยาลัย
Chulalongkorn University

CHAPTER III
EXPERIMENTAL PROCEDURES

In this chapter, I will describe the fabrication processes of CIGS thin film solar cells, including the characterization techniques such as J-V characteristics and EQE measurements for observing the performances of the device.

3.1 Fabrication processes of CIGS thin film solar cells

The typical structure of CIGS thin film solar cells consists of six different layers deposited on soda-lime glass (SLG) substrate; Al-grid/ZnO(Al)/i-ZnO/CdS/CIGS/Mo/SLG. Firstly, Mo metallic layer as a back contact of solar cell is deposited by DC magnetron sputtering with the thickness of 0.6 μm. The CIGS absorber layer as p-type semiconducting material is deposited by the three-stage process, CGS/CIS, CIS/CGS bilayer and CGS/CIS/CGS trilayer processes with the thickness of 1.8 μm. The CdS buffer layer with the thickness of 50 nm is deposited by chemical bath deposition (CBD). Then, i-ZnO and the n-type semiconducting materials of ZnO(Al) window layer are deposited by RF magnetron sputtering. The thicknesses of i-ZnO and ZnO(Al) are approximately 50 nm and 200 nm, respectively. Finally, Al metallic layer as a front contact is deposited by thermal evaporation with the thickness of 2 μm. The typical structure of CIGS thin film solar cell is illustrated in Figure 18.

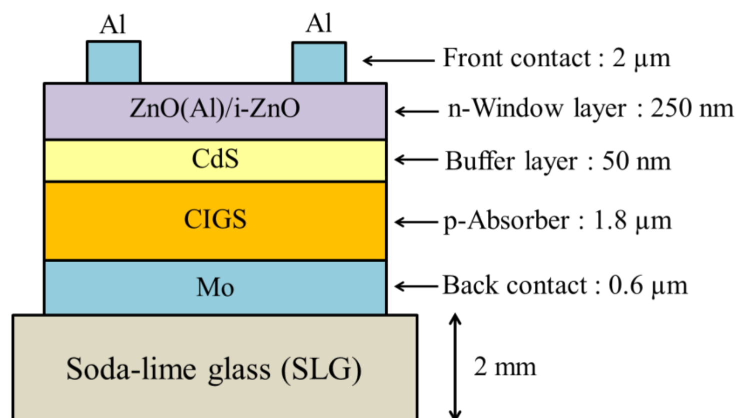

Figure 18 Schematic structure of $Cu(In,Ga)Se_2$ thin film solar cells.

CIGS absorber layer

In this work, the methods to fabricate normal and double Ga-grading profiles compared with uniform Ga distribution are studied. CGS/CIS, CIS/CGS bilayers and CGS/CIS/CGS trilayers are examples to observe Ga-grading profiles by means of front, back and double grading. Moreover, thinner absorbers using double grading profile for reduction of materials and times used in the process are also under investigation. The schematic structures of bilayers and trilayers are depicted in Figure 19. Each layer of the bilayers, CGS/CIS and CIS/CGS are also studied under both Cu-rich (y=1.2) and Cu-poor (y=0.9) conditions. The diagrams of bilayer growth conditions are shown in Figure 20.

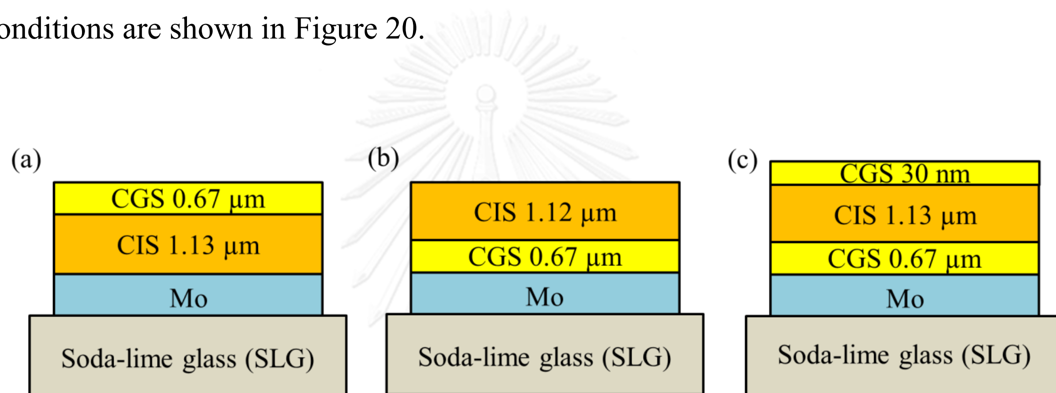

Figure 19 Schematic structure of $Cu(In,Ga)Se_2$ thin film solar cells prepared by Ga-grading profiles (a) front grading, (b) back grading and (c) double grading.

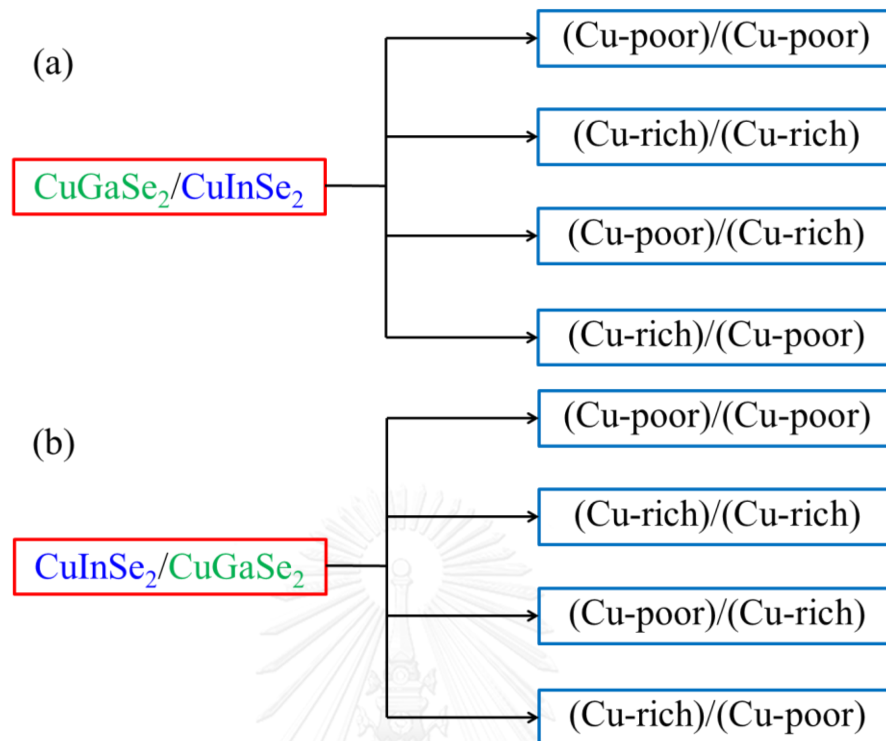

Figure 20 Diagram of CGS/CIS and CIS/CGS bilayers deposited under Cu-rich (y=1.2) and Cu-poor (y=0.9) conditions.

3.1.1 SLG substrate preparation

Soda-lime glass (SLG) substrate is widely used for CIGS thin film solar cells due to its adhesion property and low cost material. The thermal coefficient of SLG matches with α–CIGS and the alkali metals e.g. Sodium (Na) from SLG can diffuse through and thus improve the solar cell performance [34]. Firstly, deionized (DI) water and the dishwashing liquid are mixed for SLG soaking. Then, a wet cellulose sponge is used to polish SLG for 5 minutes and placed in substrate holder. The cleaned SLG is soaked with mixing of concentrated cleaning solution (Micro-90) of 30 ml and DI water of 1500 ml in an ultrasonic bath at 60°C for one hour. Next, the cleaned SLG is soaked with Chromic acid (H_2CrO_4) for one hour in order to enhance surface adhesion. Finally, the substrates are dried with compressed nitrogen gas and kept in a dry cabinet.

จุฬาลงกรณ์มหาวิทยาลัย
Chulalongkorn University

3.1.2 Mo back contact

In this experiment, Mo metallic layer is used as a back contact of CIGS thin film solar cells. The advantages of Mo metallic layer are good adhesion to SLG substrate, low resistivity and no reaction with Cu, In and Ga. In many studies [35, 36], Mo can react with Se to form $MoSe_2$ layer at high temperature. Then, slightly thin layer of $MoSe_2$ can enhance the adhesion of CIGS on Mo interface and it can improve the electrical properties as the ohmic contact. Mo metallic layer is deposited by DC magnetron sputtering using 4-inch diameter Mo target. The adhesion and low resistivity arise from high sputtering power (550W) and low sputtering pressure of Ar gas (1.0 x 10^{-3} mbar). The sputtering time for Mo film deposition is 12 minutes with substrate rotation at 3 rpm. The typical thickness of Mo for CIGS thin film solar cells in this work is ~600 nm.

3.1.3 CdS buffer layer

The Cadmium sulfide (CdS) buffer layer is II-VI semiconducting material with direct bandgap energy of 2.4 eV. The wet process of chemical bath deposition (CBD) is used to deposit CdS thin films. The advantages of the wet process are that it can enhance the entire surface covering and remove natural oxide at CdS/CIGS interface. The formation of CdS thin film is a result from two different mechanisms as the accumulation of the colloids (heterogeneous growth) and direct reaction of the ions at the substrate surface (ion-by-ion growth). The reaction of CdS formation performed by Cadmium ions, Thiourea molecules and Ammonia solutions is shown in eq. 25 [37, 38].

$$Cd(NH_3)_4^{2+} + SC(NH_2)_2 + 2OH^- \rightarrow CdS + CH_2N_2 + 4NH_3 + 2H_2O \qquad (25)$$

Each reaction is separately described in eqs. 26-28.

1) Release Cd^{2+} from ammonia complex;

$$Cd(NH_3)_4^{2+} \rightarrow Cd^{2+} + 4NH_3. \qquad (26)$$

2) Release of S^{2-} from Thiourea;

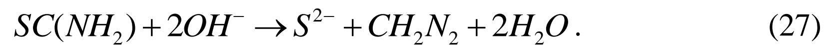

$$SC(NH_2) + 2OH^- \rightarrow S^{2-} + CH_2N_2 + 2H_2O. \quad (27)$$

3) Precipitation of CdS;

$$Cd^{2+} + S^{2-} \rightarrow CdS. \quad (28)$$

In this experiment, 0.3456 g of $CdSO_4$ solid powder is dissolved in 50 ml DI water (0.27 M concentration). Then, 2.85 g of $SC(NH_2)_2$ solid powder is dissolved in 100 ml DI water (0.375 M concentration). Finally, 25% ammonia solution of 80 ml is mixed in the aqueous solution of the two solutions mentioned previously. The aqueous solutions in the beaker are mixed and stirred at room temperature for 1 minute. Then, the CIGS film in the beaker is put in the heat bath at 65^oC. The total time for CdS deposition is 15 minutes for CdS thickness as approximately 50 nm. Before CIGS film is put in the CdS solution, KCN (potassium cyanide) aqueous solution is used to etch CIGS surface in order to remove excess $Cu_{2-x}Se$ compound by immersing in the KCN solution for 1 minute.

3.1.4 ZnO window layers

Two layers of intrinsic zinc oxide (i-ZnO) and aluminum-doped zinc oxide (ZnO(Al)) with direct bandgap of 3.3 eV and 3.6 eV, respectively, are deposited on top of CdS layer. For slightly thin i-ZnO layer, it provides high resistivity that prevents the leakage paths between CdS buffer and ZnO(Al) window layers [39].

The advantages of ZnO(Al) are its high optical transmission, low resistivity, non-toxicity and low-cost material [40]. In addition, ZnO(Al) thin film does not interact with oxygen in the environment and stable than other materials such as tin-doped In_2O_3 (ITO) and tin oxide (SnO_2). In this experiment, the layer of i-ZnO is deposited by RF magnetron sputtering using 2-inch diameter of i-ZnO target with reactive O_2 gas and Ar gas at sputtering pressure of 3.0 x 10^{-4} mbar and 6.0 x 10^{-3} mbar, respectively. Also, the sputtering power is 80 W for 11 minutes with substrate rotation of 10 rpm. Then, ZnO(Al) is deposited using only pure Ar gas at the low

pressure of 1.0 x 10^{-3} mbar using 4-inch diameter ZnO(Al) target. The sputtering power is 220 W for 20 minutes with substrate rotation of 3 rpm. The typical thickness of i-ZnO and ZnO(Al) are approximately 50 nm and 200 nm, respectively.

3.1.5 Al-grid front contact

Al metallic layer as a front contact of CIGS thin film solar cells is deposited by thermal evaporation system using stainless steel shadow mask. The individual cell of 0.515 cm^2 is obtained by mechanical scribbling. The 3cm x 3cm substrate can be divided into 8 cells. Al-grid should be thick enough for collecting the generated carriers inside the CIGS absorber layer. The base pressure of the vacuum chamber is around 6.0 x 10^{-6} mbar. The thickness of Al layer is monitored by a quartz crystal monitor (QCM) during evaporation process for thickness of 2 μm.

3.2 Solar cell characterizations

3.2.1 Current density-Voltage measurement (J-V)

The most important tool for solar cell characterization is the current density-voltage (J-V) measurement. The J-V measurement set up consists of the xenon lamp as a light source evaluated under AM1.5 or 100 mW/cm^2 at 25°C. The DC power supply is a voltage source/current measurement unit (Keithley model 237). The four-point probe configuration is used as the contact of solar cells. Then, J-V measurement parameters such as the open-circuit voltage (V_{oc}), the short-circuit current density (J_{sc}), the fill factor (FF) and the efficiency (η) display on the PC are acquired by IEEE-488 card and data acquisition software using the agilent VEE. The J_{sc} refers to the photons that are absorbed and generated inside the absorber layer. The V_{oc} is related to the bandgap energy of the absorber, and the fill factor is the ratio of the maximum output power to the obtained value of J_{sc} and V_{oc}. The J-V measurement set up is shown in figure 21.

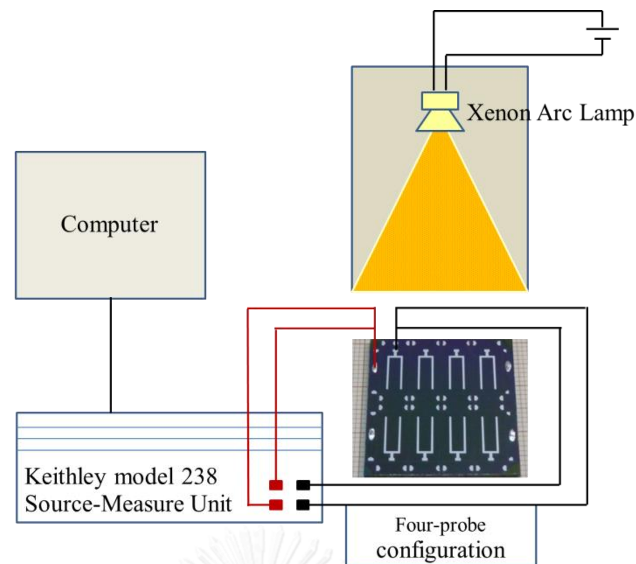

Figure 21 The schematic diagram of J-V measurement set up.

3.2.2 External Quantum Efficiency measurement (EQE)

The external quantum efficiency (EQE) measurement is the tool for measuring the spectral response that the carriers can be generated by the absorber layer. When the incident photons including reflection and transmission are illuminated at the photovoltaic devices, the carriers can be generated at the specific wavelength measured by the J_{sc} as defined by

$$QE(\lambda) \equiv \frac{\text{number of collected electrons}}{\text{number of incident photons}} = \frac{I_{sc}(\lambda)/q}{\Phi_{ph}(\lambda)}, \quad (29)$$

where $I_{sc}(\lambda)$ is the photocurrent generating in unit of [A], $\Phi_{ph}(\lambda)$ is the incident photon flux in unit of [#/sec].

In addition, the actual QE may be reduced by many factors so that the EQE curve corresponding to photo-generated current reduction is seen in Figure 22.

จุฬาลงกรณ์มหาวิทยาลัย
Chulalongkorn University

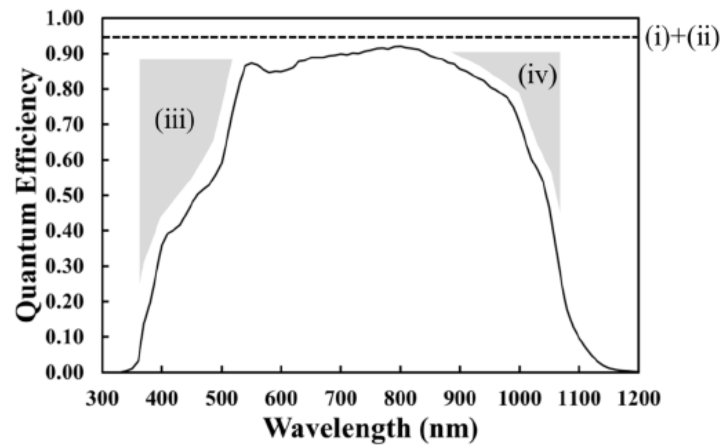

Figure 22 EQE spectrum of a CIGS solar cell showing the factors causing the current losses as labeled in each region.

(i) Grid shading; the incident photons that shining cover the front surface area can be lose in QE spectrum by shading of Al-grid.

(ii) Reflection; the incident photons can be reduced by anti-reflecting layer, e.g. MgF_2 at the front side.

(iii) Window and buffer layers absorptions; the optical absorptions in ZnO window and CdS buffer layers depend on heavy n-type doping. Thus, the carriers may have a short life time and cannot diffuse to the SCR.

(iv) Incomplete collections; the carriers generated at long wavelength can be recombined before drifting to the SCR, and the defect at the CdS/CIGS interface may result in the incomplete current collections.

While the integrated area under a curve implies the total photogenerated current produced by a cell which can be calculated by

$$I_{sc} = q\int_{\lambda} \Phi_{ph}(\lambda) \cdot EQE(\lambda) d\lambda , \tag{30}$$

where $\Phi_{ph}(\lambda)$ is the incident photon flux of wavelength λ, the integration is the optical absorption at all wavelength ranges [41].

CHAPTER IV
THE FABRICATION OF CIGS THIN FILM SOLAR CELLS BY THE THREE-STAGE PROCESS

CIGS absorber thin films with uniform bandgap are usually deposited by the three-stage process. These will be used as reference cell. In this method, Se is always over supplied. First, the $(In,Ga)_2Se_3$ precursor layer is to be examined by varying Se evaporation flux during the 1st stage. Then, the substrate temperatures of entire stages are investigated to find the optimum working temperatures for achieving the highest efficiency of the reference cell. Finally, CIGS thin film solar cells grown by the three-stage process are compared with the graded bandgap grown by the bilayer and trilayer systems discussed in chapter V.

The three-stage process deposition of CIGS is based on multi-sources co-evaporation of Cu, In Ga and Se. The evaporation source for each element is a Knudsen type with a 40cc pyrolytic boron nitride (PBN) cylindrical crucible inserted in the heat-shielded housing wound with a tantalum heater. The substrate heater was made of a resistive heating element and the thermocouple was placed near the backside of the SLG substrate to provide a signal for the PID temperature controller. The base pressure of the system prior to the deposition was less than 2×10^{-6} Torr. During the 1st stage of deposition, $(In_{1-x}Ga_x)_2Se_3$ (IGS) precursor layer was deposited at low substrate temperature (T_1). In the 2nd stage, the substrate temperature was rapidly increased to T_2 and only Cu and Se were co-evaporated until the overall composition is Cu-rich (y = [Cu]/([In]+[Ga]) = 1.3) to form CIGS layer. Finally, in the 3rd stage, In Ga and Se were again co-evaporated at T_2 until slightly Cu-poor phase (y ~ 0.9) was obtained at the end of the process. The ramp-up time from T_1 to T_2 was set to 5 minutes. In this work, the substrate temperatures T_1 were first varied from 300°C to 410°C while T_2 was kept constant at 580°C. Once the optimum value of T_1 was obtained by considering the properties of the CIGS absorber and the device parameters, then T_2 was varied from 500°C to 580°C while T_1 was kept constant at its optimum value. We note that the T_1 and T_2 values reported here were the setting values at the PID temperature controller for the substrate. The duration time for the

CIGS deposition process is approximately 120 minutes with the thickness of the CIGS absorber layer of approximately 1.8 μm. In this work, the average value of x = [Ga]/([In]+[Ga]) was approximately set to 0.37. A pyrometer and an output power signal of the substrate temperature controller were employed to monitor the radiations from the surface of the growing films corresponding to change in the emissivity of the surface of the growing CIGS films as shown in Figure 23. The oscillations in the pyrometer signals during the 1st stage were due to multiple reflections of radiations from the front and back surfaces of the growing $(In_{1-x}Ga_x)_2Se_3$ precursor. The thickness of the precursor was also verified from the period of oscillations using the 1.55 μm wavelength detected by the pyrometer and the index of refraction of IGS precursor. Points A and B are when the CIGS films are at stoichiometric ratio in the 2nd and 3rd stage, respectively. Point C is at the end of the deposition process where y ~ 0.9. After deposition process, the finished CIGS thin film grown on 10 cm x 10 cm Mo-coated SLG substrate were divided into 9 pieces of 3 cm x 3 cm as shown in Figure 24 (a) and (b), respectively. The CIGS thin films were labeled in each of substrate position as the upper zone of A1, A2, A3, middle zone of B1, B2, B3 and lower zone of C1, C2, C3.

จุฬาลงกรณ์มหาวิทยาลัย
CHULALONGKORN UNIVERSITY

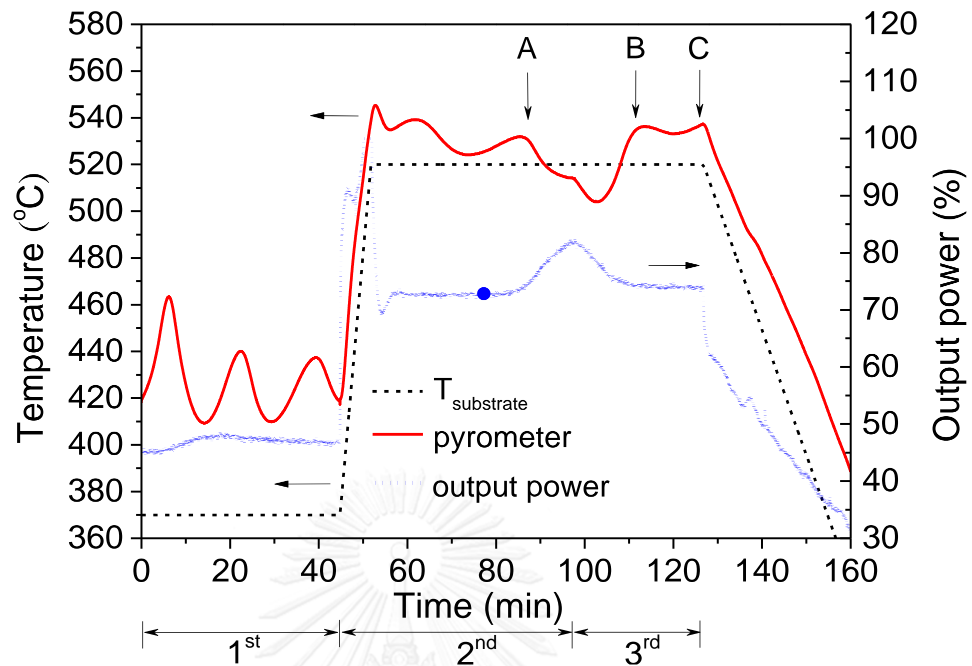

Figure 23 The three-stage deposition process during CIGS thin film growth observed by the output power of substrate (blue line), the pyrometer signal (red line) and the substrate temperature (black line). Then, Cu composition observed by stoichiometric (y=1), Cu-rich (y>1) and Cu-poor (y<1).

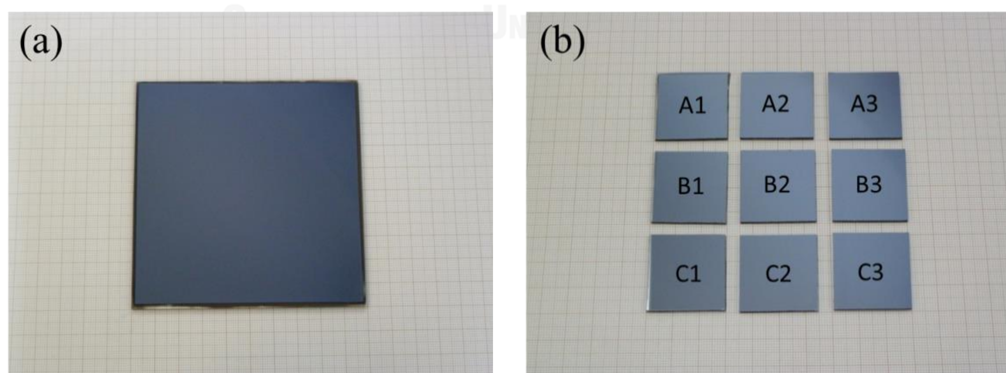

Figure 24 The finished CIGS thin film grown on (a) 10 cm x 10 cm Mo-coated SLG substrate and (b) CIGS films was divided into 9 pieces of 3 cm x 3 cm.

4.1 The effect of Se source temperatures on $(In,Ga)_2Se_3$ precursors

In this study, Se source temperatures or Se fluxes were investigated on $(In,Ga)_2Se_3$ (IGS) precursor layers with the substrate temperature of 390°C. The Se source temperature was varied in the range of 280°C, 300°C and 320°C. Surface morphologies and cross-section images were examined by FESEM. The Se composition was confirmed by Energy dispersive X-ray spectrometer (EDS).

FESEM results

Surface morphologies, cross-section images and Se composition of IGS precursor layer with Se source temperature at 280°C are shown in Figure 25. The surface morphologies of IGS precursor layer show combinations of triangular and granular grains for each position. The center of the film area (B2 zone) shows larger sharp triangular grains than those of other zones. It can be noticed that C1 zone shows many small grains. The cross-section image shows the thickness of IGS precursor layer is 869 nm and the ratio of Se composition to group III elements ([Se]/([In]+[Ga]) at 280°C is 1.52.

Se source temperature of 300°C, surface morphologies, cross-section images and Se composition of the IGS precursor layer are shown in Figure 26. The surface morphologies of IGS precursor layer show more triangular grains than small round grains in all positions. At the center of the film area (B2 zone) show significantly larger triangular grain and less number of round grains than the previously discussed results at 280°C. Then, cross-section image of IGS thin film shows the thickness of 884 nm and the EDS result indicates that the ratio of Se composition to group III elements is 1.57.

When the Se source temperature was increased to 320°C, the results are somewhat similar to those of 300°C and shown in Figure 27. The cross-section image of the IGS thin film show the thickness of 850 nm and the EDS result indicates that

the ratio of Se composition to group III elements is 1.58. The thickness of the IGS precursor layers and Se composition ratio for Se source temperatures at 280°C, 300°C and 320°C are summarized in Table 8.

The results indicate that triangular grains are related to the supplied Se flux during the IGS thin film deposition. For smaller round grains, supplied Se may be insufficient and can lead to solar cell performances deterioration [42]. It can be seen that the [Se]/([In]+[Ga]) is ~1.5 despite the increasing of Se flux during the 1st stage. Se flux directly affects surface morphology of the IGS precursor.

J-V characterization

The solar cell parameters, e.g. V_{oc}, J_{sc}, FF and η are summarized in Table 9. The J-V curves of various Se fluxes are shown in Figure 28. In case of Se source temperature at 320°C, Se source was inadequate for the whole deposition process. The results indicate that Se source temperature of 300°C has the best solar cell parameters including the highest efficiency of 12.2%. The Se source temperature of 280°C has insufficient evaporation rate for the device fabrications. Thus, the optimum Se source temperature is 300°C for CIGS thin film deposition.

จุฬาลงกรณ์มหาวิทยาลัย
Chulalongkorn University

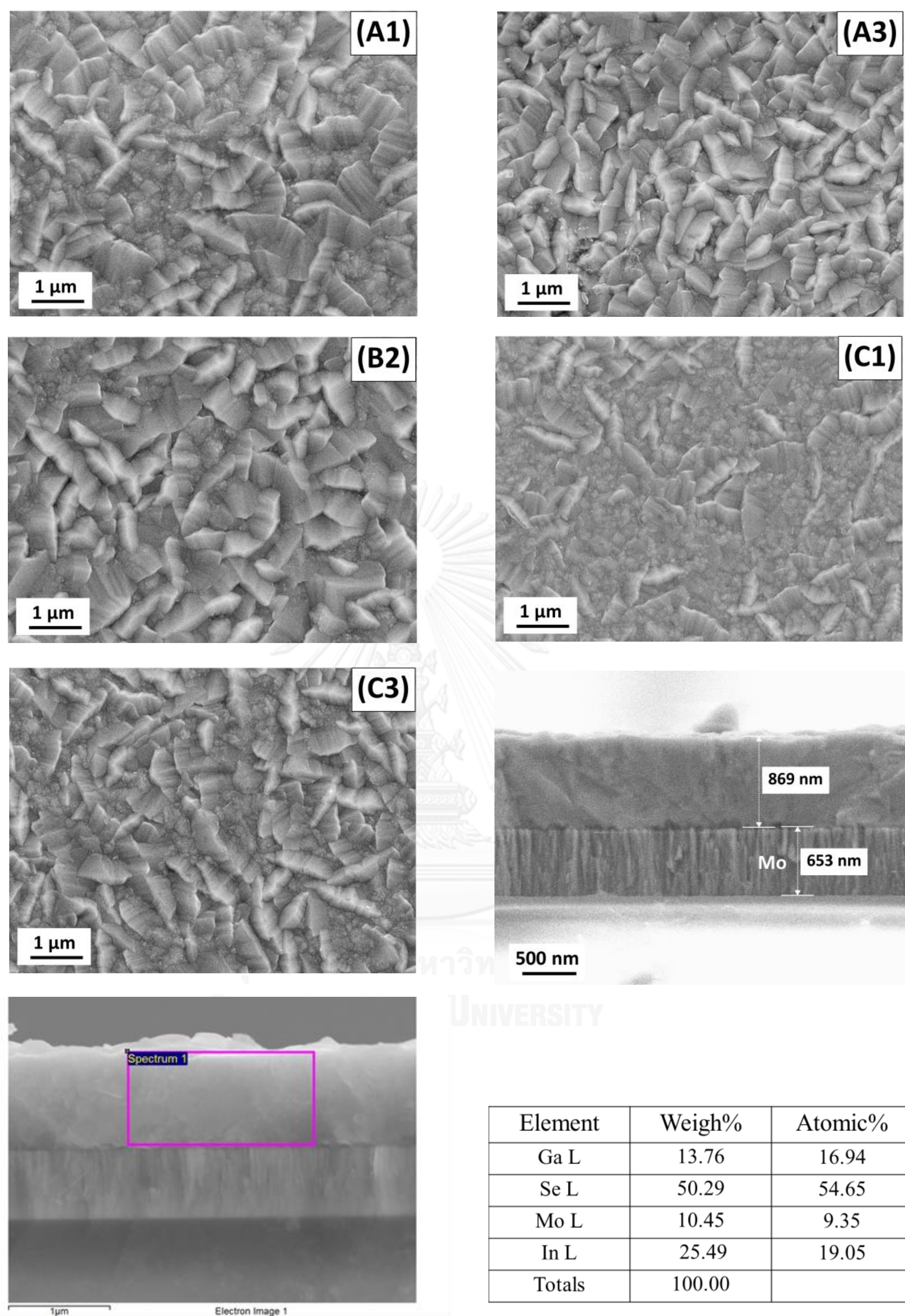

Element	Weigh%	Atomic%
Ga L	13.76	16.94
Se L	50.29	54.65
Mo L	10.45	9.35
In L	25.49	19.05
Totals	100.00	

Figure 25 The surface morphologies of $(In,Ga)_2Se_3$ precursors by varying Se source temperature at 280°C in each different film area, cross-section image of $(In,Ga)_2Se_3$ precursor grown on Mo-coated SLG substrate and EDS result measured the Se composition in the IGS precursor layer.

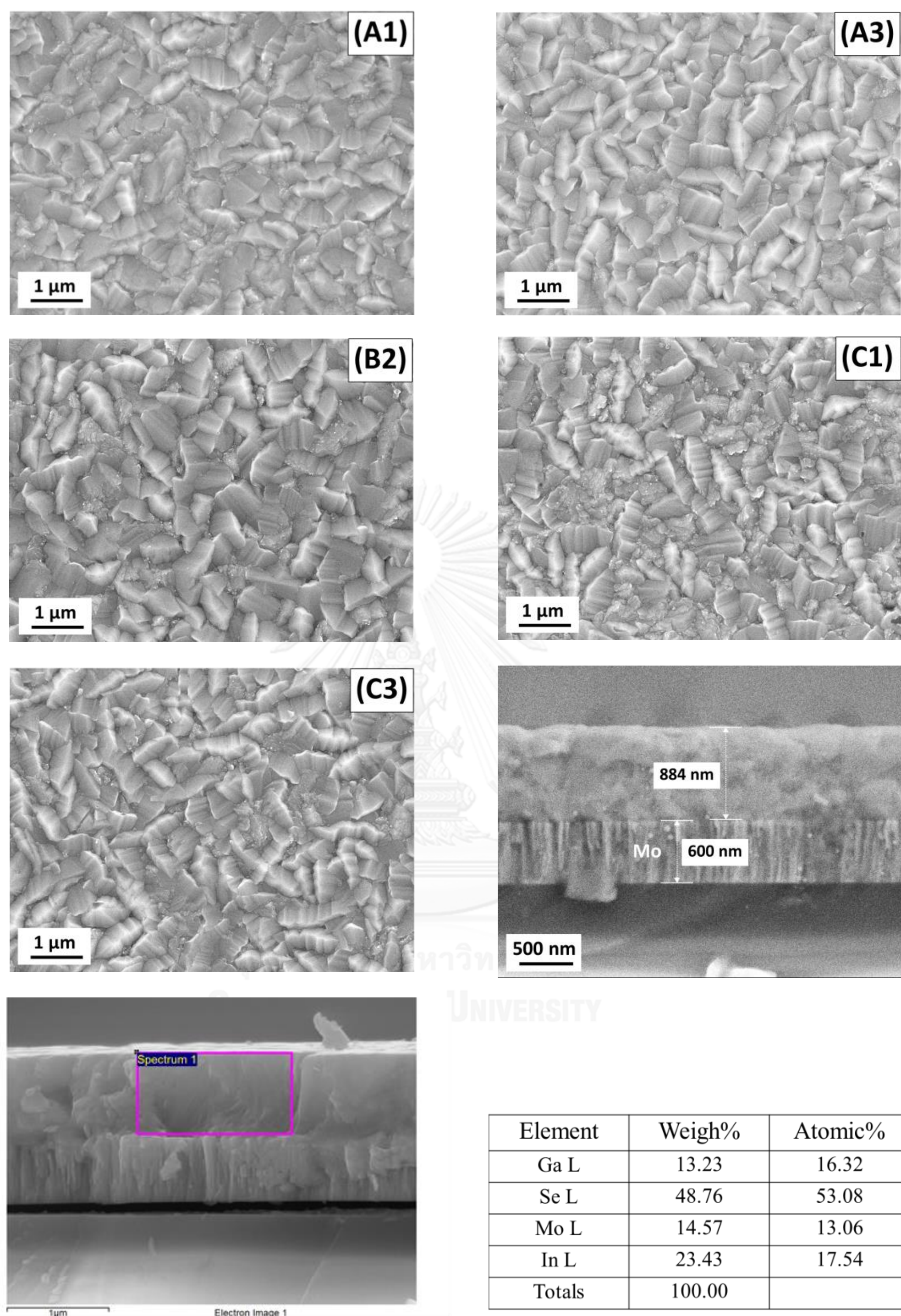

Element	Weigh%	Atomic%
Ga L	13.23	16.32
Se L	48.76	53.08
Mo L	14.57	13.06
In L	23.43	17.54
Totals	100.00	

Figure 26 The surface morphologies of $(In,Ga)_2Se_3$ precursors by varying Se source temperature at 300°C in each different film area, cross-section image of $(In,Ga)_2Se_3$ precursor grown on Mo-coated SLG substrate and EDS result measured the Se composition in the IGS precursor layer.

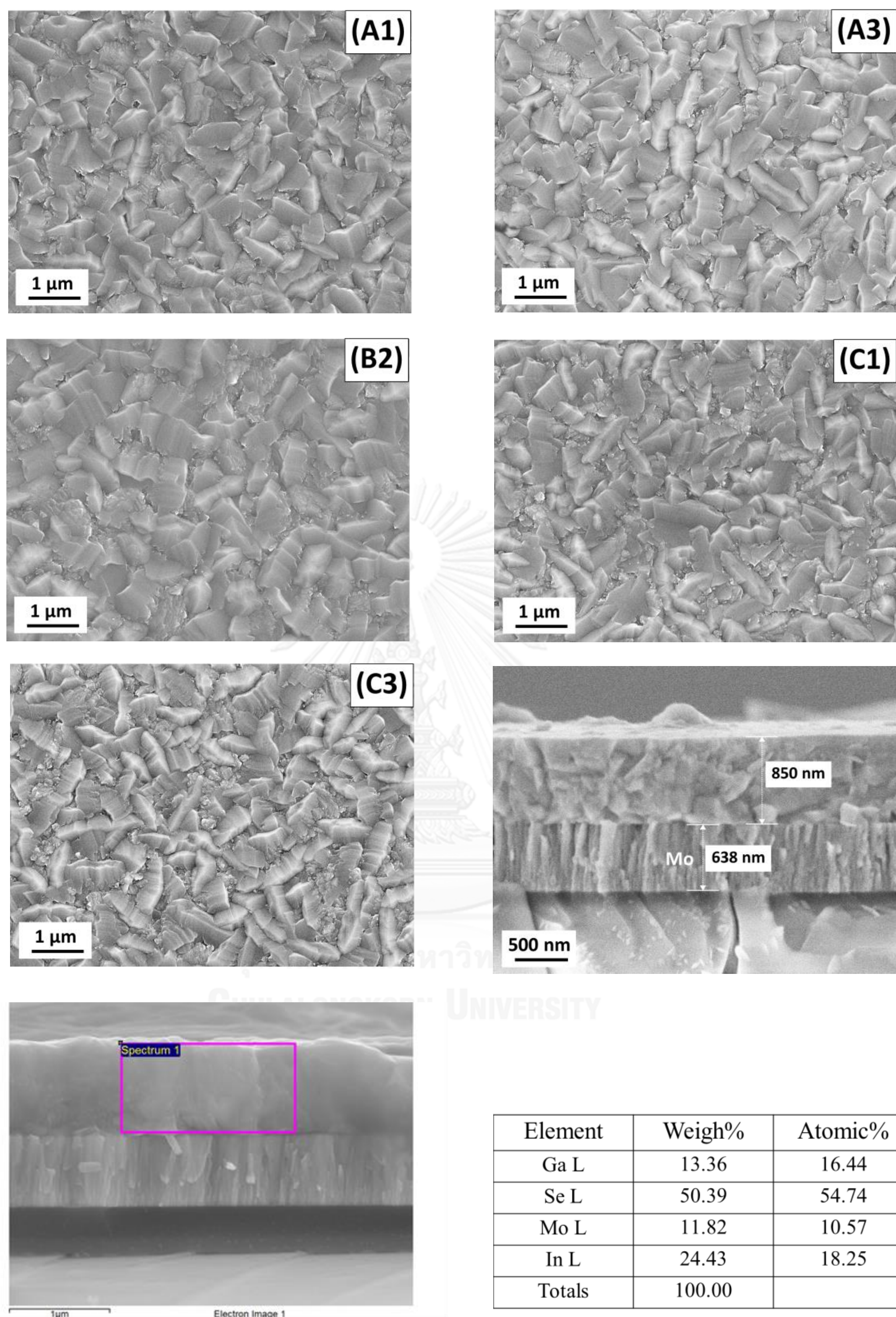

Element	Weigh%	Atomic%
Ga L	13.36	16.44
Se L	50.39	54.74
Mo L	11.82	10.57
In L	24.43	18.25
Totals	100.00	

Figure 27 The surface morphologies of $(In,Ga)_2Se_3$ precursors by varying Se source temperature at 320°C in each different film area, cross-section image of $(In,Ga)_2Se_3$ precursor grown on Mo-coated SLG substrate and EDS result measured the Se composition in the IGS precursor layer.

Table 8 The variation of Se composition and thickness of precursor layers by varying Se source temperatures at 280°C, 300°C and 320°C.

Se source temperature (°C)	280	300	320
$(In,Ga)_2Se_3$ thickness (nm)	869	884	850
[Se]/([n]+[Ga])	1.52	1.57	1.58

Table 9 The solar cell parameters of varying Se source temperatures at 280°C and 300°C.

Se source temperature (°C)	V_{oc} (mV)		J_{sc} (mA/cm^2)		FF (%)		η (%)	
	Avg.	Max.	Avg.	Max.	Avg.	Max.	Avg.	Max.
280	557.6	593.0	25.7	29.7	60.2	65.4	8.6	10.1
300	598.7	632.0	28.8	30.9	64.2	70.5	11.0	12.2

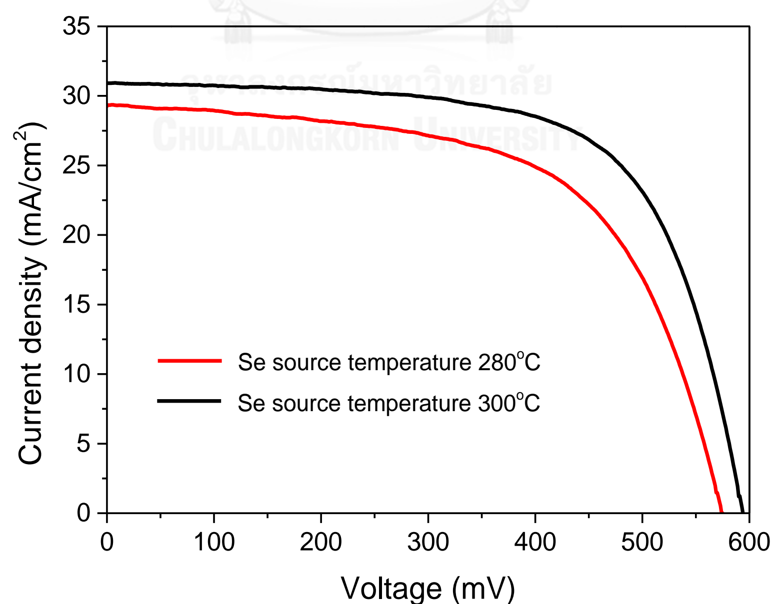

Figure 28 J-V characteristics of the devices with best efficiency fabricated from varying Se source temperature at 280°C and 300°C.

CHULALONGKORN UNIVERSITY

It can be summarized here that Se flux plays an important role in the formation of the $(In_{1-x}Ga_x)_2Se_3$ precursor in the 1st stage. The Se flux in our setup was found to be sufficient for the temperature of the Se source at 300°C. The surface morphologies of 300°C show more triangular grains rather than small round grains in all positions with [Se]/[III] ~ 1.57 and have the best solar cell parameters including the highest efficiency of 12.2%. However the Se source temperature at 320°C was inadequate for the whole deposition process in this setup.

4.2 The effect of substrate temperatures on CIGS thin film solar cells

4.2.1 FESEM cross-section images of varying substrate temperatures in the 1st stage

In this study, substrate temperatures in the 1st stage (T_1) were varied from 300°C, 350°C, 370°C, 390°C and 410°C with constant substrate temperature in the 2nd stage (T_2) and the 3rd stages at 580°C. FESEM cross-section images of various substrate temperatures at the 1st stage are shown in Figure 29. The results show large columnar grains as large as the CIGS thickness and dense grains with no crevices all of substrate temperatures. These suggest that the large grains are the effect from the high substrate temperature in the 2nd and 3rd stages closed to the softening point of the SLG substrate. The thermal energy from the substrate at 580°C can induce the grain growth of approximately 0.5-1.0 μm in size by the existence of $Cu_{2-x}Se$ liquid phase in all temperatures.

4.2.2 XRD patterns of varying substrate temperatures in the 1st stage

The XRD patterns of various substrate temperatures in the 1st stage from 300°C, 350°C, 370°C, 390°C and 410°C with constant substrate temperature at the 2nd and 3rd stage of 580°C are shown in Figure 30. The (112) and (220)(204) phases indicate the chalcopyrite structure. The intensities of (112) peak increase with increasing substrate temperatures from 300°C to 390°C, but because lower at 410°C. It is known that III_2-VI_3 compound such as the γ-$(In,Ga)_2Se_3$ layer have many phase transformations as well as different crystalline structures and quite sensitive to

deposition conditions including substrate temperature. At 300°C and 350°C, the (220)(204) phase is a more preferred-orientation than the (112) phase, which may be the effect of residual strain for insufficient temperature [42]. The phase transformation to (112) plane occurs at higher temperature that is referred to re-crystallization of γ-$(In,Ga)_2Se_3$ structure at 370°C and 390°C. For 410°C, the deformation of γ-$(In,Ga)_2Se_3$ structure can occur and then it may cause the change of preferred orientation to (220)(204). The results indicate that the increasing substrate temperature can improve the crystalline quality of CIGS structure but it should not be more than 400°C. Thus, the substrate temperature in the 1st stage should be between 370°C and 390°C

4.2.3 J-V measurements of varying substrate temperatures in the 1st stage

The solar cell parameters of various substrate temperatures in the 1st stage are summarized in Table 10. In this study, 40 devices, each of 0.515 cm^2 were investigated at each substrate temperature. The solar cell parameters for the substrate temperatures of 300°C and 350°C show the increase of the J_{sc} but the V_{oc} is not improved. In case of the substrate temperature of 370°C, both of the J_{sc} and the V_{oc} are improved. The substrate temperatures of 390°C and 410°C show the increase of the V_{oc} with lowering J_{sc}. The results indicate that the increase of substrate temperature can enhance the V_{oc}, but the J_{sc} is a trade-off. The optimum temperature in the 1st stage is 370°C to achieve the maximum efficiency of 13.1%. However, the temperature of 390°C that has the highest crystalline quality show the highest FF up to 70.5%. It was suggested that larger grain size might be induced the undesirable cluster formation of the CIGS films that affects the current generations. The solar cell parameters and the J-V curves of various substrate temperatures in the 1st stage are shown in Figure 31 and Figure 32, respectively.

จุฬาลงกรณ์มหาวิทยาลัย
Chulalongkorn University

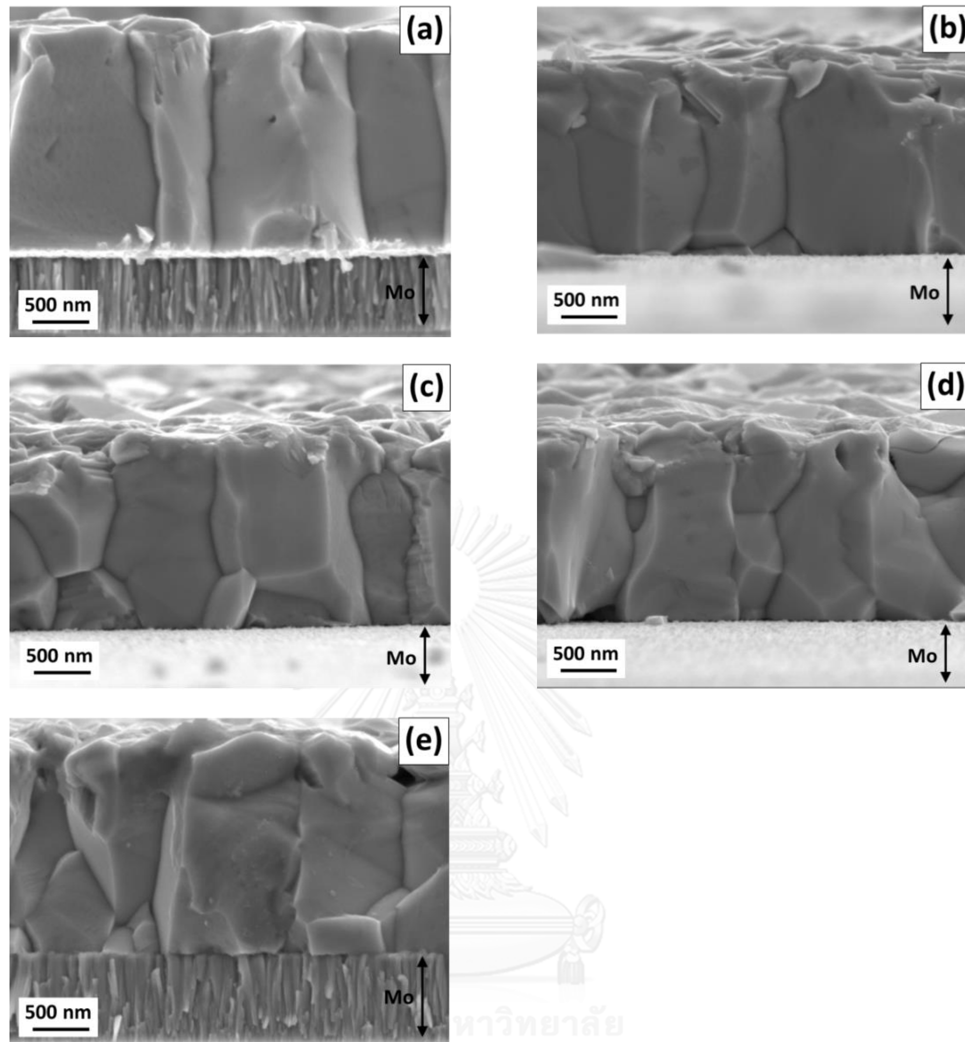

CHULALONGKORN UNIVERSITY

Figure 29 FESEM cross-section images of CIGS thin film for varying substrate temperatures in the 1st stage at (a) 300°C, (b) 350°C, (c) 370°C, (d) 390°C and (e) 410°C with constant substrate temperature in the 2nd and 3rd stages at 580°C.

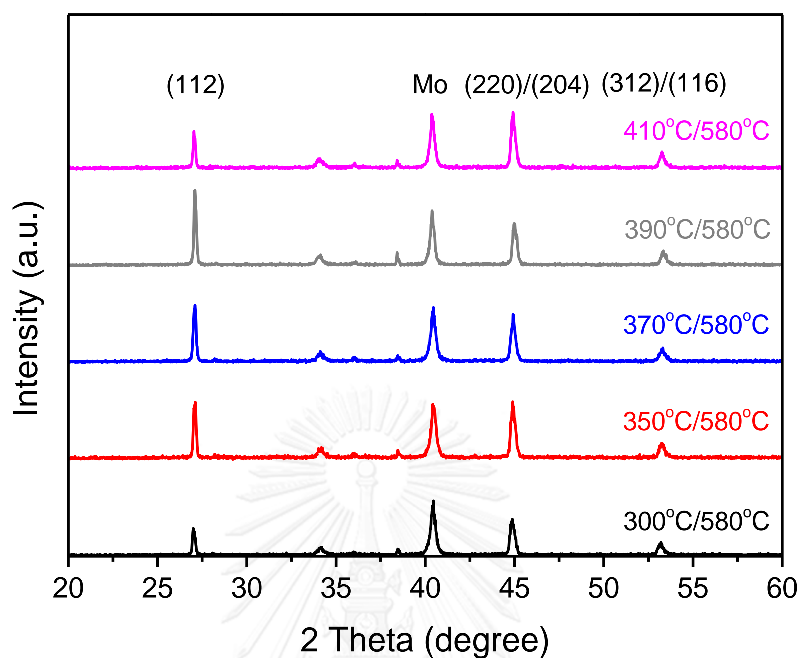

Figure 30 XRD patterns of CIGS thin film for varying substrate temperatures in the 1st stage at (a) 300°C, (b) 350°C, (c) 370°C, (d) 390°C and (e) 410°C with constant substrate temperature in the 2nd and 3rd stages at 580°C.

จุฬาลงกรณ์มหาวิทยาลัย
Chulalongkorn University

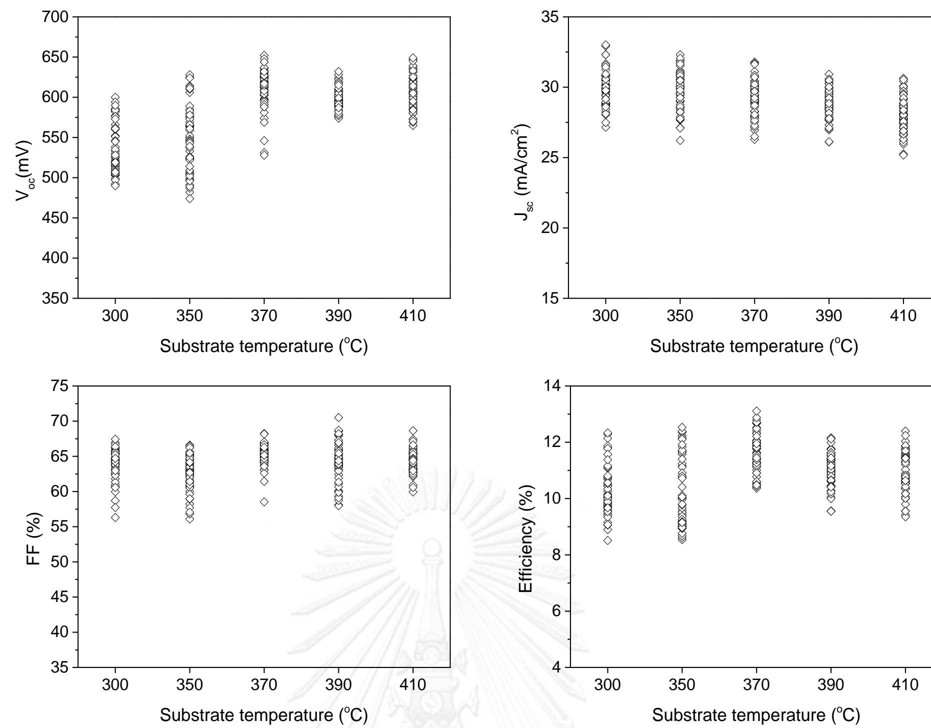

Figure 31 Distributions of CIGS solar cell parameters of the devices fabricated from varying substrate temperatures in the 1st stage at 300°C, 350°C, 370°C, 390°C and 410°C with constant substrate temperature in the 2nd and 3rd stages at 580°C.

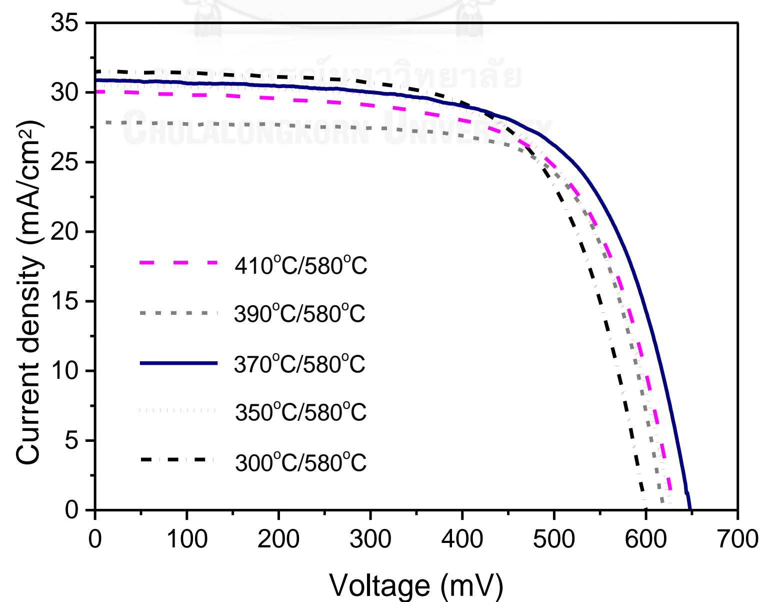

Figure 32 J-V characteristics of the devices with best efficiency fabricated from varying substrate temperatures in the 1st stage at 300°C, 350°C, 370°C, 390°C and 410°C with constant substrate temperature in the 2nd and 3rd stages at 580°C.

Table 10 The solar cell parameters of varying substrate temperatures in the 1st stage at 300°C, 350°C, 370°C, 390°C and 410°C with constant substrate temperature in the 2nd and 3rd stages at 580°C.

$T_{substrate}$ (°C) (1st stage)	V_{oc} (mV)		J_{sc} (mA/cm^2)		FF (%)		η (%)	
	Avg.	Max.	Avg.	Max.	Avg.	Max.	Avg.	Max.
300	540.8	600.0	30.1	33	63.8	67.4	10.4	12.3
350	556.6	628.0	29.5	32.3	62.7	66.6	10.3	12.5
370	617.4	652.0	29.2	31.8	65.2	68.2	11.7	13.1
390	598.6	632.0	28.8	30.9	64.5	70.5	11.1	12.2
410	608.9	649.0	28.2	30.6	64.2	68.6	11	12.4

It can be summarized here that the influence of γ-$(In,Ga)_2Se_3$ phase transformation of (112) and (220)(204) has an important role for crystalline quality and change in the nucleation of films in the 1st stage. The highest crystalline quality of (112) phase appear at lower substrate temperatures between 370°C and 390°C due to re-crystalline structure leading to high solar cell performances up to 13.1%. The higher intensity of (220)(204) phase appears at 300°C, 350°C due to residual strain for insufficient temperature and the deformation at 410°C. All T_1 conditions show large grain sizes by $Cu_{2-x}Se$ inducing grain growth at higher temperature at 580°C.

4.2.4 FESEM cross-section images of varying substrate temperatures in the 2nd and 3rd stages

The study of varying substrate temperature in the 1st stage yielded the optimum value for the 1st stage temperature of 370°C by keeping the substrate temperature in the 2nd and 3rd stages at 580°C. To find the optimum temperature in the 2nd and 3rd stages, the substrate temperatures were varied from 500°C, 520°C, 540°C, 560°C and 580°C with constant substrate temperature at the 1st stage at 370°C.

FESEM cross-section images of various substrate temperatures in the 2nd and 3rd stages are shown in Figure 34. When substrate temperatures were increased, the average grain sizes were visibly increased. At the temperature of 560°C and 580°C, the columnar grains are as large as CIGS thin film thickness due to $Cu_{2-x}Se$ enhancement by thermal energy at higher substrate temperature. It can be explained that the increasing atomic mobility can induce the film formation and reduce the grain boundaries. While smaller grains with many grain boundaries appeared at 500°C to 540°C. It is suggested that the less inter-diffusion of atoms is slowly settled down on the precursor at lower energy. The average grain size at lower temperatures is approximately 0.25-0.50 µm.

EDS depth profile of CIGS absorber layer

The compositional depth profile of CIGS absorber layer was investigated by series of EDS spot scan and the results shown in Figure 33. The result indicates that Ga contents were relatively uniform composition throughout the CIGS thickness. It can be noticed that CIGS absorber layer grown by the three-stage process was rather homogeneous Ga distribution which used as a reference absorber for comparing with those of bilayer and trilayer absorbers.

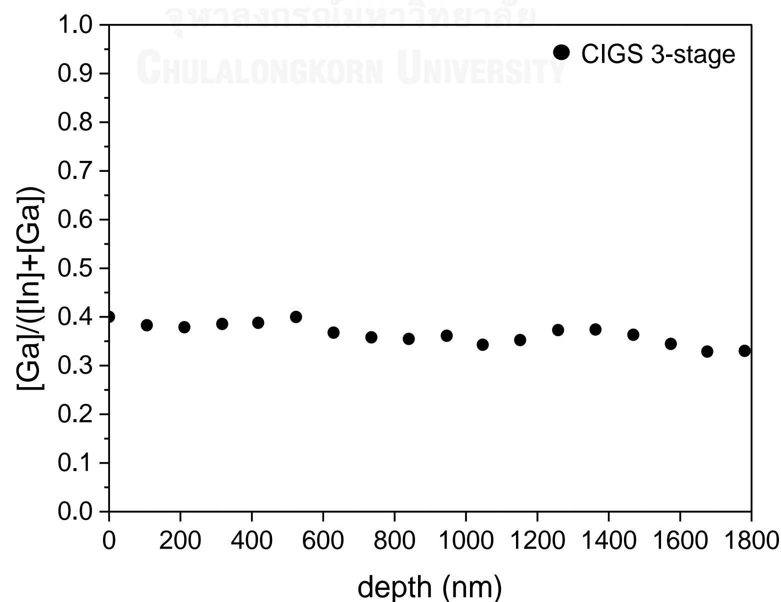

Figure 33 EDS depth profile of CIGS absorber layer grown by the 3-stage process.

CHULALONGKORN UNIVERSITY

4.2.5 XRD patterns of varying substrate temperatures in the 2nd and 3rd stages

The XRD patterns of various substrate temperatures in the 2nd and 3rd stages from 500°C, 520°C, 540°C, 560°C and 580°C with constant substrate temperature in the 1st stage at 370°C are illustrated in Figure 35. The XRD patterns also show (112) and (220)(204) phases of chalcopyrite structure. All conditions show the intensity of (112) phase higher than that of the (220)(204) phase. The highest intensity of (112) peak appears at the substrate temperature of 520°C and is referred as the preferred orientation with the highest (112) : (220)/(204) intensity ratio of 2.2. It was implied that the good crystalline quality appear in lower temperature because the atoms were slowly settled down on γ-$(In,Ga)_2Se_3$ precursor at lower energy. The cross-section images of substrate temperatures at 560°C and 580°C show larger columnar grains, but the XRD patterns show lower intensities of (112) peak. It is implied that higher substrate temperature may not promote the quality of CIGS structure during thin film deposition due to undesirable cluster formation. In addition, Na diffusion from SLG can promote the (112) preferred-orientation and may improve the crystalline quality at temperature of 520°C.

4.2.6 J-V measurements of varying substrate temperatures in the 2nd and 3rd stages

The solar cell parameters of various substrate temperatures in the 2nd and 3rd stages are shown in Table 11. When the substrate temperatures were increased in the range of 500°C to 580°C, the V_{oc} was also increased to the maximum value of 652 mV but the J_{sc} are decreased. The J_{sc} are relatively higher at temperatures of 500°C and 520°C leading to higher efficiencies, but the FF at 500°C is less than that of 520°C. The highest efficiency of CIGS thin film solar cell is up to 13.7% for the substrate temperature in the 2nd and 3rd stages of 520°C. It was indicated that the highest crystalline quality due to increasing (112) phase at 520°C tends to increase the solar cell performances. In addition, the minor effect of Na diffusion from SLG may increase the p-type doping in the solar cells. The solar cell parameters and the J-V curves of various substrate temperatures in the 2nd and 3rd stages are shown in Figure 36 and Figure 37, respectively.

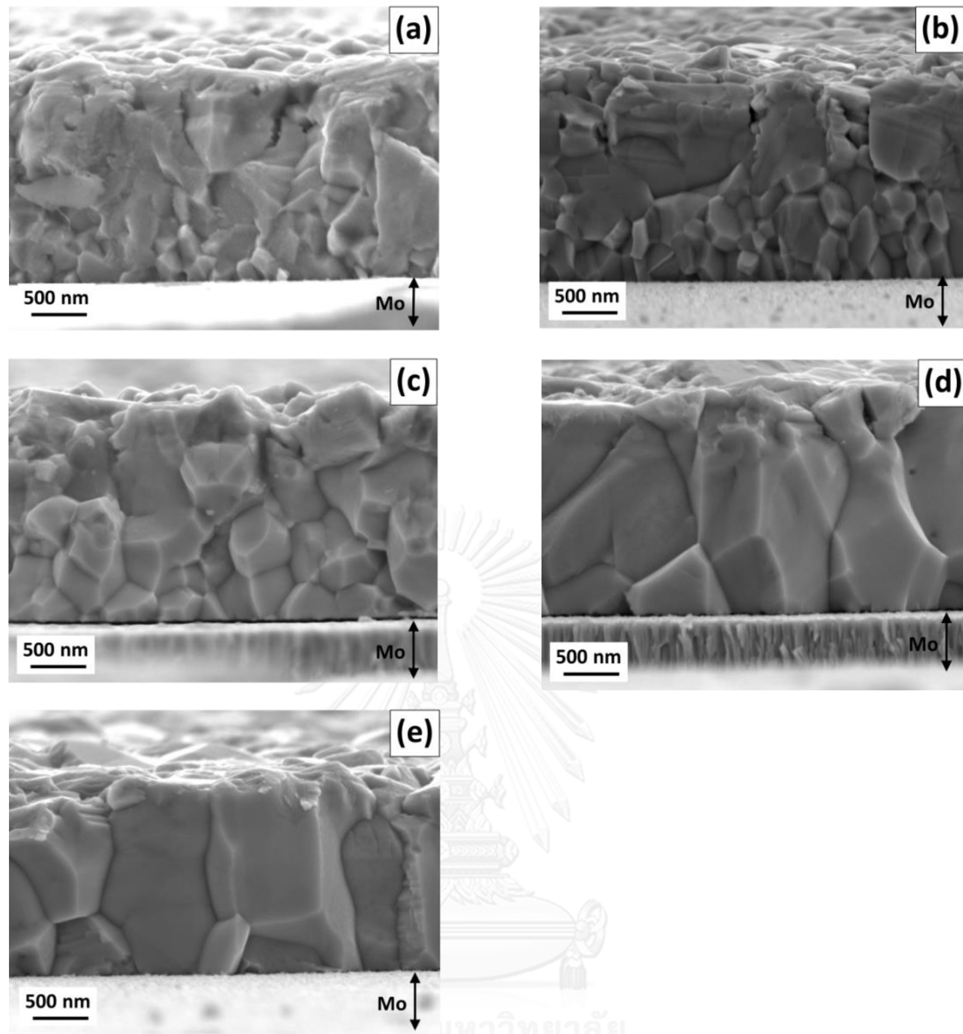

จุฬาลงกรณ์มหาวิทยาลัย
CHULALONGKORN UNIVERSITY

Figure 34 FESEM cross-section images of CIGS thin films for varying substrate temperatures in the 2nd and 3rd stages at (a) 500°C, (b) 520°C, (c) 540°C, (d) 560°C and (e) 580°C with constant substrate temperature in the 1st stage at 370°C.

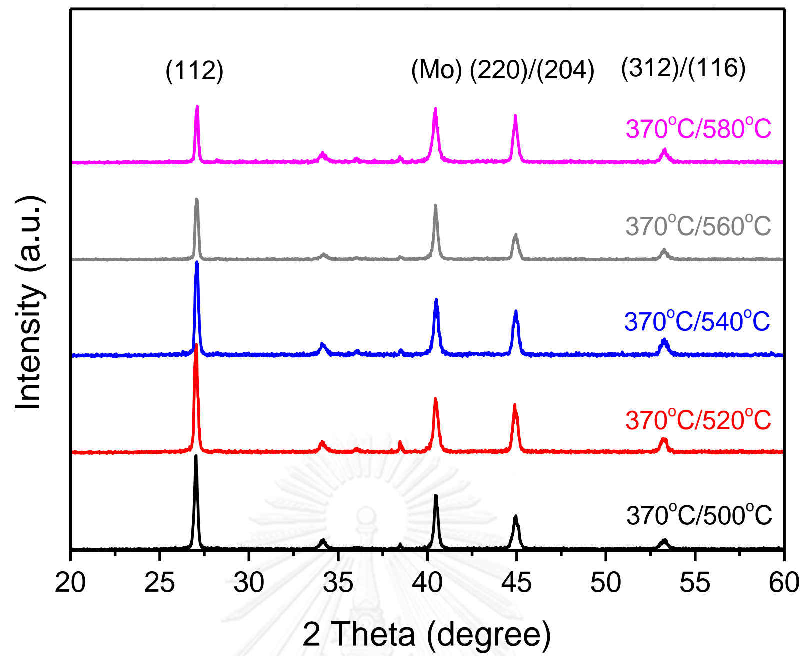

Figure 35 XRD patterns of CIGS thin film for varying substrate temperatures in the 2nd and 3rd stages at 500°C, 520°C, 540°C, 560°C and 580°C with constant substrate temperature in the 1st stage at 370°C.

จุฬาลงกรณ์มหาวิทยาลัย
Chulalongkorn University

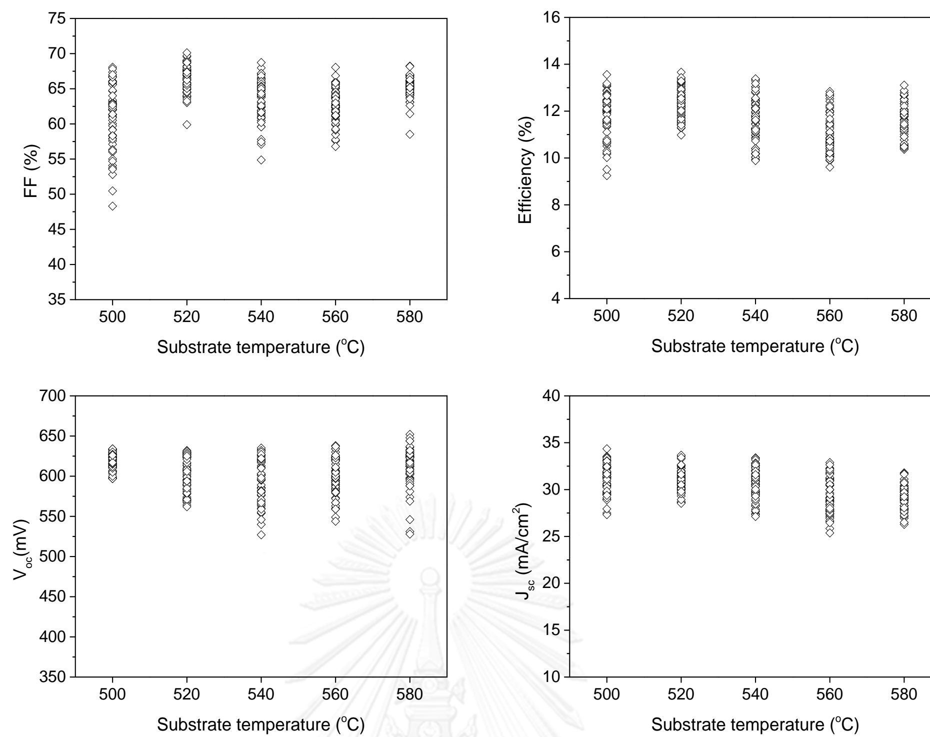

Figure 36 Distributions of CIGS solar cell parameters of the devices fabricated from varying substrate temperatures in the 2nd and 3rd stages at 500°C, 520°C, 540°C, 560°C and 580°C with constant substrate temperature in the 1st stage at 370°C.

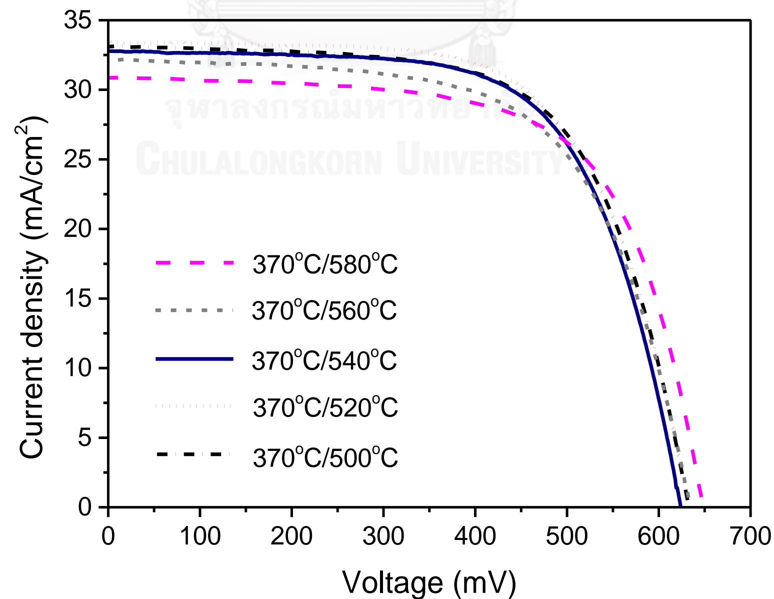

Figure 37 J-V characteristics of the devices with best efficiency fabricated from varying substrate temperatures in the 2nd and 3rd stages at 500°C, 520°C, 540°C, 560°C and 580°C with constant substrate temperature in the 1st stage at 370°C.

จุฬาลงกรณ์มหาวิทยาลัย
Chulalongkorn University

Table 11 The solar cell parameters of varying substrate temperatures in the 2nd and 3rd stages at 500°C, 520°C, 540°C, 560°C and 580°C with constant substrate temperature in the 1st stage at 370°C.

$T_{substrate}$ (°C) (2nd and 3rd stage)	V_{oc} (mV)		J_{sc} (mA/cm^2)		FF (%)		η (%)	
	Avg.	Max.	Avg.	Max.	Avg.	Max.	Avg.	Max.
500	617.4	634	31.4	34.4	61.9	68.1	12.0	13.6
520	607.1	632	31.1	33.7	66.2	70.1	12.5	13.7
540	598.4	635	30.5	33.4	64.2	68.7	11.7	13.4
560	605.6	638	29.3	32.9	62.4	68.1	11.1	12.8
580	617.4	652	29.2	31.8	65.2	68.2	11.7	13.1

4.3 Summary

The optimization to obtain the suitable substrate temperatures T_1 andT_2 for the three-stage deposition process of the CIGS absorber was performed by considering the crystal quality together with photovoltaic performances. The influence of thermal energy enhancement from the substrate has an effect on the atomic mobility. The less inter-diffusion of atoms were slowly settled down on the precursor at lower energy at 500°C to 540°C and the columnar grains are as large as CIGS thin film thickness due to $Cu_{2-x}Se$ enhancement by thermal energy from higher substrate temperature at 560°C and 580°C. Thus, the highest crystalline quality by increasing of (112) phase at 520°C resulting from the atomic relaxation tends to increase the solar cell performances with the maximum device efficiency of 13.7% and FF = 70.1% for this particular deposition system. Furthermore, it is shown here that higher efficiency devices do not necessary need to have large grain size.

จุฬาลงกรณ์มหาวิทยาลัย
Chulalongkorn University

CHAPTER V
THE FABRICATION OF CIGS THIN FILM SOLAR CELLS USING BILAYER AND TRILAYER SYSTEMS

For the previous study, the CIGS thin film solar cell with uniform bandgap was fabricated by the three-stage deposition process for the reference device. In this chapter, the variations of bandgap leading to bandgap grading are discussed. The increase of Ga composition at the front (CGS/CIS) or back (CIS/CGS) contacts leads to the front or back grading, respectively. Then, the increasing Ga composition at both front and back (CGS/CIS/CGS) contacts leading to double grading is also examined. To observe the effects of the bilayer and trilayer systems, the single layer of CGS and CIS were firstly investigated in order to study the properties of each layer that has an effect on the solar cell performances.

5.1 CGS and CIS single layer grown by the single stage process

The single layer of $CuGaSe_2$ (CGS) and $CuInSe_2$ (CIS) were deposited by single stage evaporation process under Cu-poor ([Cu]/[In]+[Ga]; y=0.9) composition with the substrate temperature of 560°C. The composition of Ga was set at x=1 for CGS single layer, and x=0 for CIS single layer throughout the deposition process. The deposition time is around 75 minutes for the typical thickness of approximately 1.8 μm. The base pressure of the evaporation process was approximately 2×10^{-6} Torr. The schematic of the deposition process of CGS and CIS single layer is illustrated in Figure 38. The *in situ* monitoring signals consisting of the pyrometer and the output power of the substrate heater are employed during the CIGS deposition. The surface morphologies, cross-section images and elemental composition of CGS and CIS single layer were investigated by FESEM and EDS. The structural properties of single layers were examined by XRD. The device performances of CGS and CIS single layer were investigated by J-V and EQE measurements.

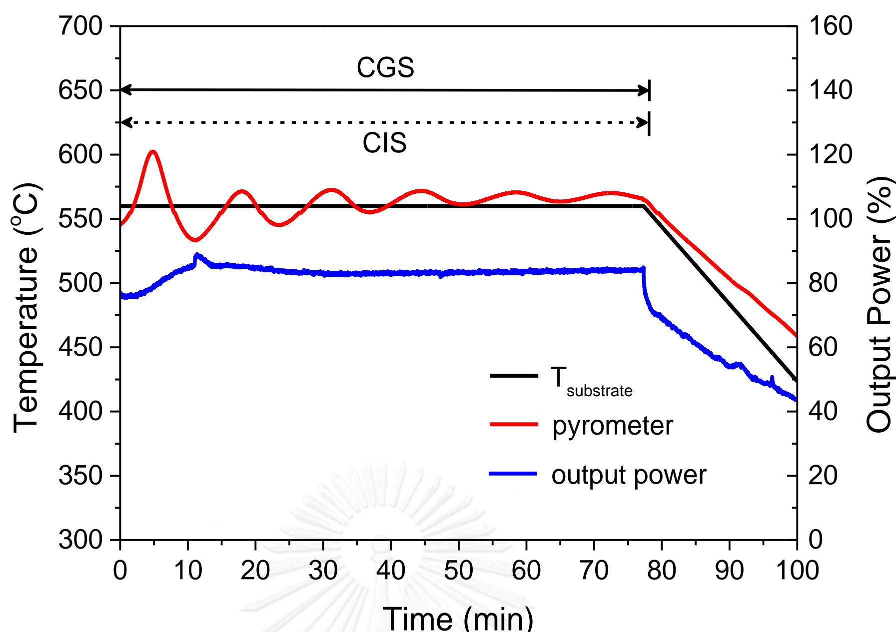

Figure 38 The single stage process of CGS or CIS thin film observed by the output power of substrate heater (blue line), the pyrometer signal (red line) and the substrate temperature (black line).

5.1.1 FESEM surface and cross-section images of CGS and CIS single layer

FESEM surface morphologies and cross-section images of CGS and CIS single layer with thickness of ~1.8 µm are presented in Figure 39. The grain sizes of CGS and CIS single layer are clearly different. CGS single layer has smaller grain sizes with many grain boundaries and smoother surface morphologies. The CIS single layer has relatively larger grain size and rougher surface morphologies than the CGS single layer. In addition, all of the single layers have dense grains with no crevices.

5.1.2 XRD patterns of CGS and CIS single layer

The XRD patterns of CGS and CIS single layer are shown in Figure 40. The XRD results show peaks of (112) and (220)(204) phases of the chalcopyrite structure. The peak positions of CGS single layer shift towards higher diffraction angle to those of CIS single layer. In addition, the intensity of (112) peak of CGS is lower than that of CIS. The results indicate that the CGS single layer has less crystalline quality than

the CIS single layer due to c/a distortion or lattice parameter reduction. It is also difficult to deposit the high quality CGS single layer at the same substrate temperature because melting point of CGS is higher than CIS.

5.1.3 J-V measurements of CGS and CIS single layer

The solar cell parameters; V_{oc}, J_{sc}, FF and η of CGS and CIS single layer are summarized in Table 12. The results show that the V_{oc} and the J_{sc} of CGS single layer are clearly different from those CIS single layer. In case of CGS single layer, the V_{oc} is extremely high but the J_{sc} is dramatically low. It can be seen that CGS single layer can improve the built-in voltage of the devices due to increasing conduction band edge at the interface. For CIS single layer, the V_{oc} is almost half of the CGS while the J_{sc} is quadruply increased. The highest efficiency of CGS and CIS single layer devices are 4.1% and 9.8%, respectively. The J-V curves of CGS and CIS single layer are shown in Figure 41.

5.1.4 EQE measurements of CGS and CIS single layer

The external quantum efficiency (EQE) results of CGS and CIS single layer are shown in Figure 42. The results indicate that CIS single layer can generate more carriers in the absorber than that of CGS single layer and then it can enhance photocurrent to generate electron-hole pairs at long wavelength regions. In case of CGS single layer, the photocurrent can generate for short spectral ranges from 350 nm to 800 nm. The current-blocking at long wavelength regions for CGS single layer is also an effect from excess Ga gradient at the CdS/CIGS interface. The current generations in the absorber layer measured by EQE measurement agree with the J_{sc} measured by J-V measurement accordingly.

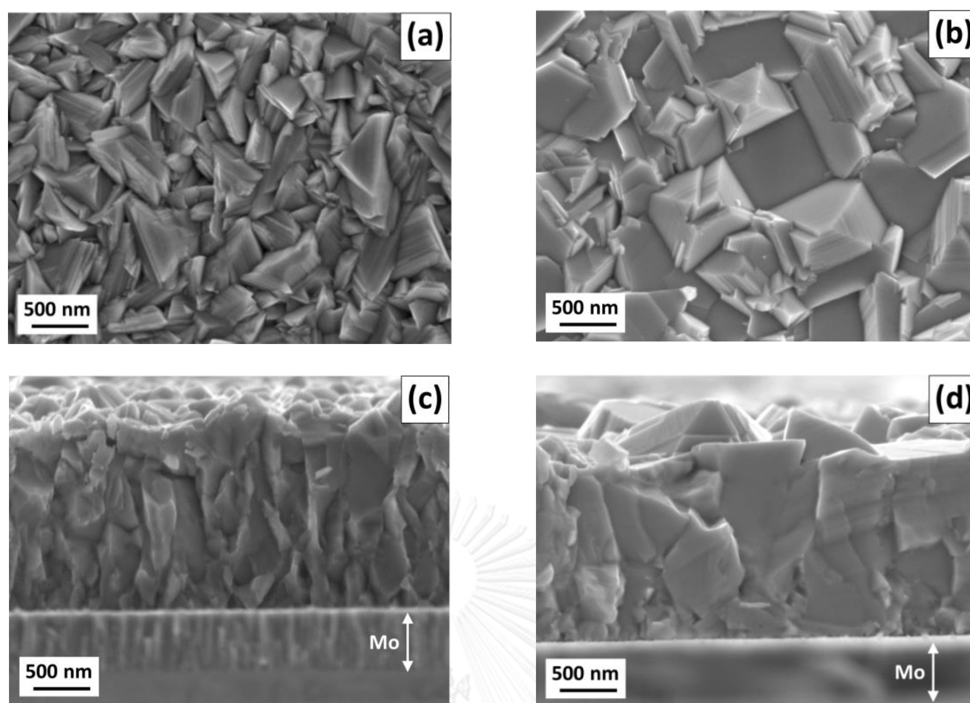

Figure 39 FESEM surface morphologies of (a) CGS single layer, (b) CIS single layer and cross-section images of (c) CGS single layer, (d) CIS single layer.

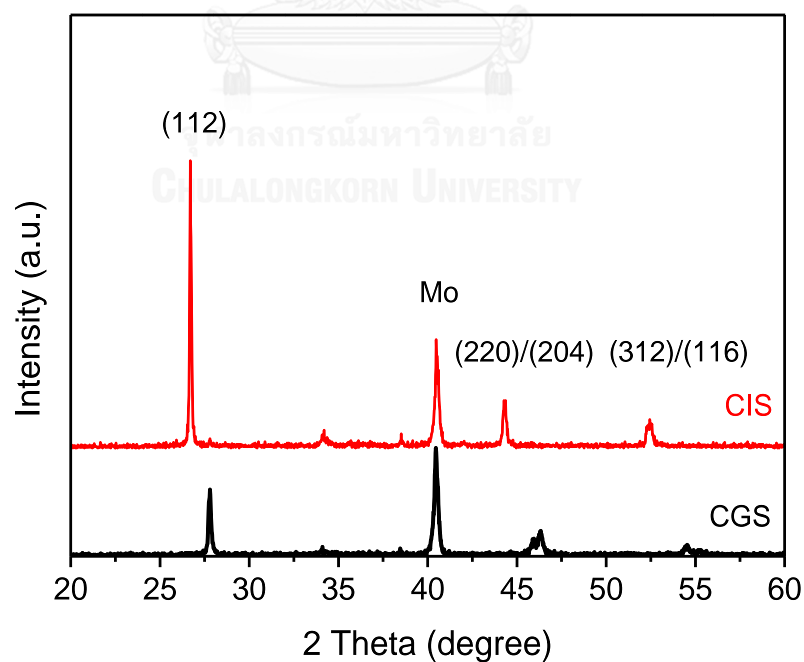

Figure 40 XRD patterns of CGS and CIS single layer.

จุฬาลงกรณ์มหาวิทยาลัย
Chulalongkorn University

Table 12 The solar cell parameters of CGS and CIS single layer.

Single layer	V_{oc} (mV)		J_{sc} (mA/cm^2)		FF (%)		η (%)	
	Avg.	Max.	Avg.	Max.	Avg.	Max.	Avg.	Max.
CGS	810.0	825.0	9.5	10.2	47.9	50.8	3.7	4.1
CIS	413.9	453.0	39.4	41.9	52.3	57.3	8.5	9.8

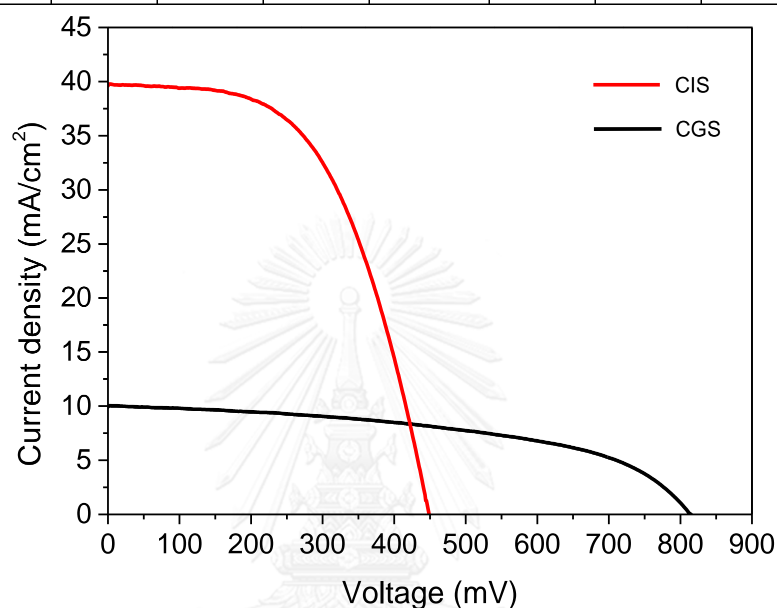

Figure 41 J-V characteristics of the devices with best efficiency fabricated from CGS and CIS single layer.

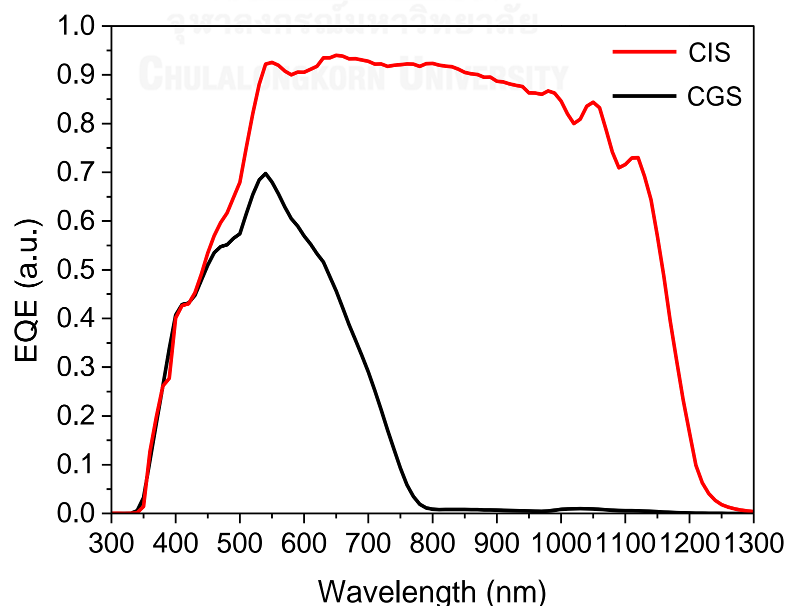

Figure 42 EQE curves of the devices with best efficiency fabricated from CGS and CIS single layer.

5.2 CGS/CIS and CIS/CGS bilayers

In this study, Ga-grading according to increasing of Ga composition at the front and the back surfaces was examined by the CGS/CIS and CIS/CGS bilayer systems. When Ga composition increased, the bandgap energy was also increased by the raise of conduction band edge. For CGS/CIS and CIS/CGS bilayer processes, total thickness was set ~1.8 μm with total deposition time of 75 minutes such that the thickness of CGS and CIS layer were approximately 0.67 μm and 1.13 μm, respectively. The composition of Ga/III related to the CGS thickness was set at ~0.37. Moreover, for all bilayer conditions, Cu/III was varied for both Cu-poor and Cu-rich at ~0.9 and ~1.2, respectively. The base pressure of the evaporation process was approximately 2×10^{-6} Torr. Consequently, the bilayers of CGS/CIS and CIS/CGS can reduce materials and times used in the process when compared to the three-stage process. The bilayer deposition profile is shown in Figure 43. The substrate temperature was set at 560°C throughout the deposition process. The red line is the pyrometer signal and the blue line is the output power of substrate. The interference fringes are corresponding to the thickness of the film.

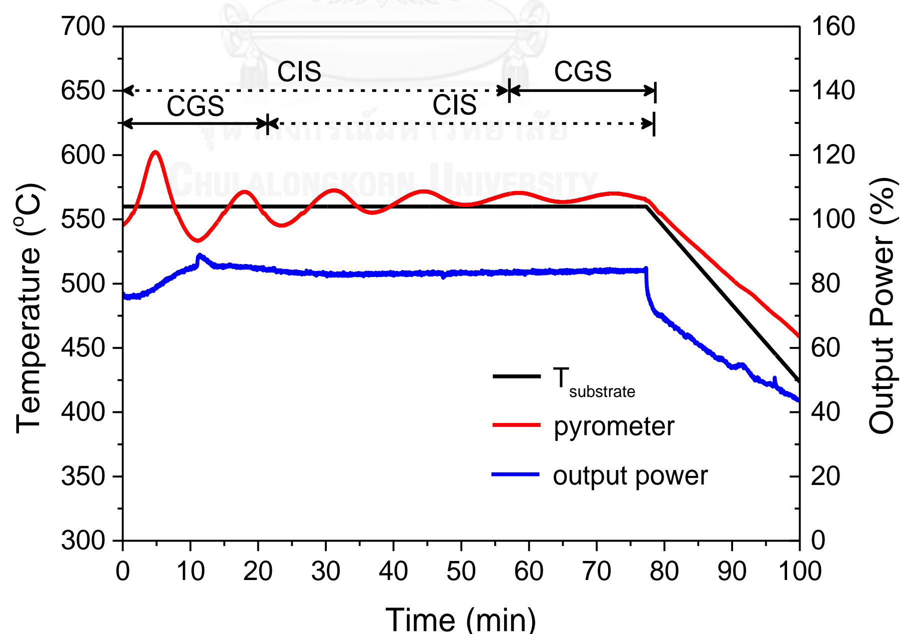

Figure 43 The bilayer deposition processes observed by the output power of substrate heater (blue line), the pyrometer signal (red line) and the substrate temperature setting (black line).

5.2.1 FESEM surface and cross-section images of CGS/CIS and CIS/CGS bilayers

CGS(y=0.9)/CIS(y=0.9) and CIS(y=0.9)/CGS(y=0.9) conditions

The surface morphologies and cross-section images of CGS(y=0.9)/CIS(y=0.9) bilayers are shown in Figure 44 (a)-(b) and then CIS(y=0.9)/CGS(y=0.9) bilayers are shown in Figure 44 (c)-(d). In this condition, the bilayers were deposited under Cu-poor composition (y=0.9). The surface morphologies are not much different between the CGS/CIS and CIS/CGS bilayers. They exhibit sharp and dense grains. In case of the cross-section images, the columnar grain sizes of CGS/CIS bilayers seem to be larger than CIS/CGS bilayers. CIS/CGS bilayers show many small grains of CGS near the bottom surface. This result is evidently verified the less inter-diffusion of Ga into the CIS layer under Cu-poor condition. For CGS/CIS bilayers, the average grain size of CIS at bottom layer is rather larger than CGS at bottom layer.

CGS(y=0.9)/CIS(y=1.2) and CIS(y=0.9)/CGS(y=1.2) conditions

The surface morphologies and cross-section images of CGS(y=0.9)/CIS(y=1.2) bilayers are shown in Figure 45 (a)-(b) and then CIS(y=0.9)/CGS(y=1.2) bilayers are shown in Figure 45 (c)-(d). For this condition, the bottom layer and the front layer were deposited under Cu-rich composition (y=1.2) and Cu-poor composition (y=0.9), respectively. The surface morphologies and cross-section images are not much different from the all Cu-poor cases. For CIS at the bottom layer under Cu-rich composition, the columnar grains are slightly larger than that of CGS at the bottom layer. Some crevices near the surface may be seen. It was indicated that Cu-rich composition especially when CIS was at the bottom layer could enhance the grain growth due to excess $Cu_{2-x}Se$ liquid phase.

CGS(y=1.2)/CIS(y=1.2) and CIS(y=1.2)/CGS(y=1.2) conditions

The surface morphologies and cross-section images of CGS(y=1.2)/CIS(y=1.2) bilayers are shown in Figure 46 (a)-(b) and then CIS(y=1.2)/CGS(y=1.2) bilayers are shown in Figure 46 (c)-(d). These bilayer conditions were deposited under Cu-rich (y=1.2) composition at the bottom and the front layers. The surface morphologies of bilayers under Cu-rich composition show larger grain sizes than those of other conditions because the excess $Cu_{2-x}Se$ liquid phase can enhance the grain growth. CIS/CGS bilayers seem to have sharper grain than CGS/CIS bilayers. For the cross-section images, the grains of CGS/CIS bilayers have many and large crevices through the bilayers thickness. Thus, it may be the path of current leakage in the device.

CGS(y=1.2)/CIS(y=0.9) and CIS(y=1.2)/CGS(y=0.9) conditions

The surface morphologies and cross-section images of CGS(y=1.2)/CIS(y=0.9) bilayers are shown in Figure 47 (a)-(b) and then CIS(y=1.2)/CGS(y=0.9) bilayers are shown in Figure 47 (c)-(d). For this condition, the bottom layer and the front layer were deposited by Cu-poor composition and Cu-rich composition, respectively. The surface morphologies of CGS/CIS bilayers show large grains and rough surface with small crevices than CIS/CGS bilayers. In case of the cross-section images, CGS at the bottom layer has smaller grain sizes than CIS at the bottom layer. For CGS/CIS bilayers, the cross-section image shows small crevices in the upper layer.

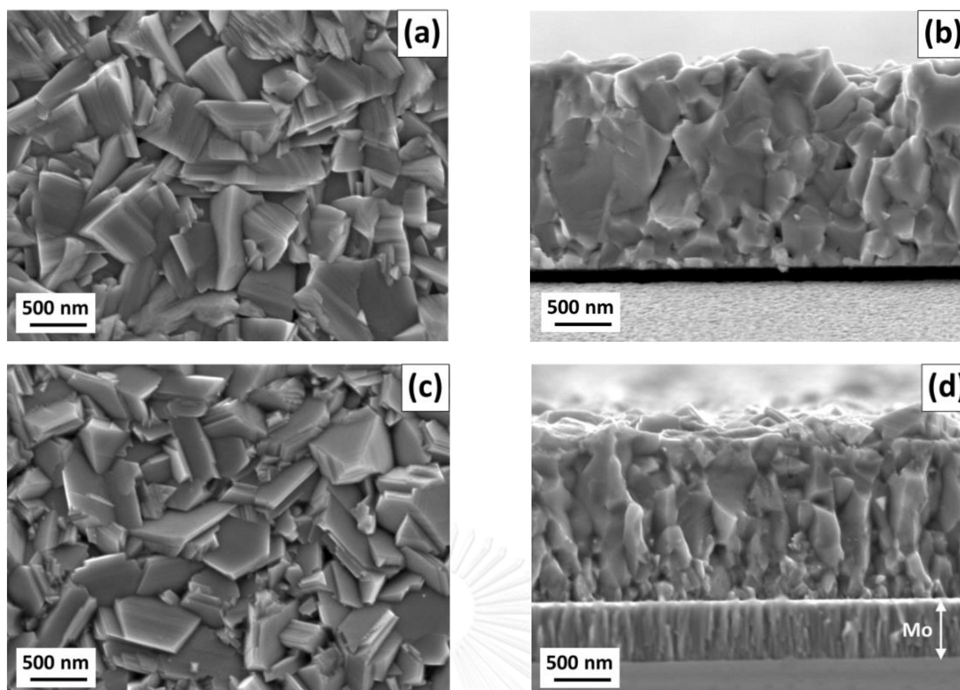

Figure 44 FESEM surface morphologies and cross-section images of (a),(b) CGS/CIS bilayers and (c),(d) CIS/CGS bilayers under Cu-poor(y=0.9)/Cu-poor(y=0.9) conditions.

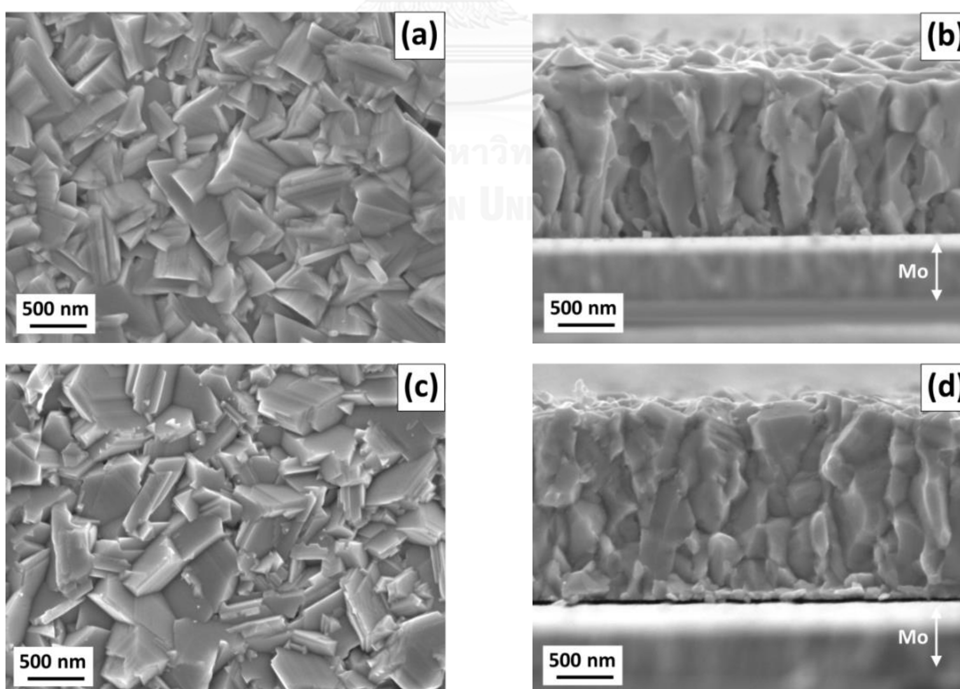

Figure 45 FESEM surface morphologies and cross-section images of (a),(b) CGS/CIS bilayers and (c),(d) CIS/CGS bilayers under Cu-poor(y=0.9)/Cu-rich(y=1.2)

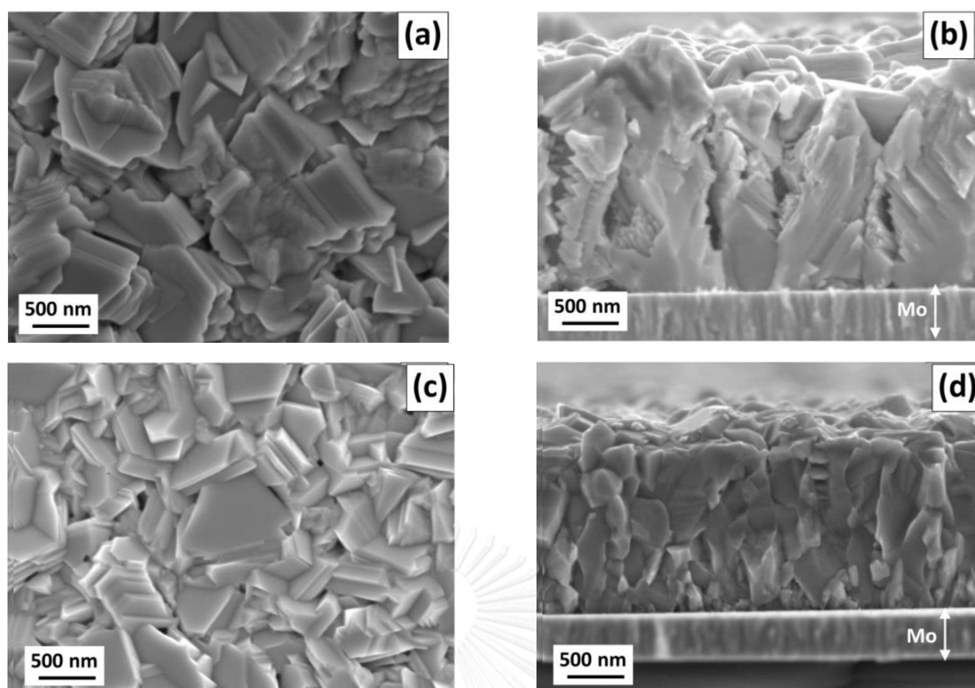

Figure 46 FESEM surface morphologies and cross-section images of (a),(b) CGS/CIS bilayers and (c),(d) CIS/CGS bilayers under Cu-rich(y=1.2)/Cu-rich(y=1.2) conditions.

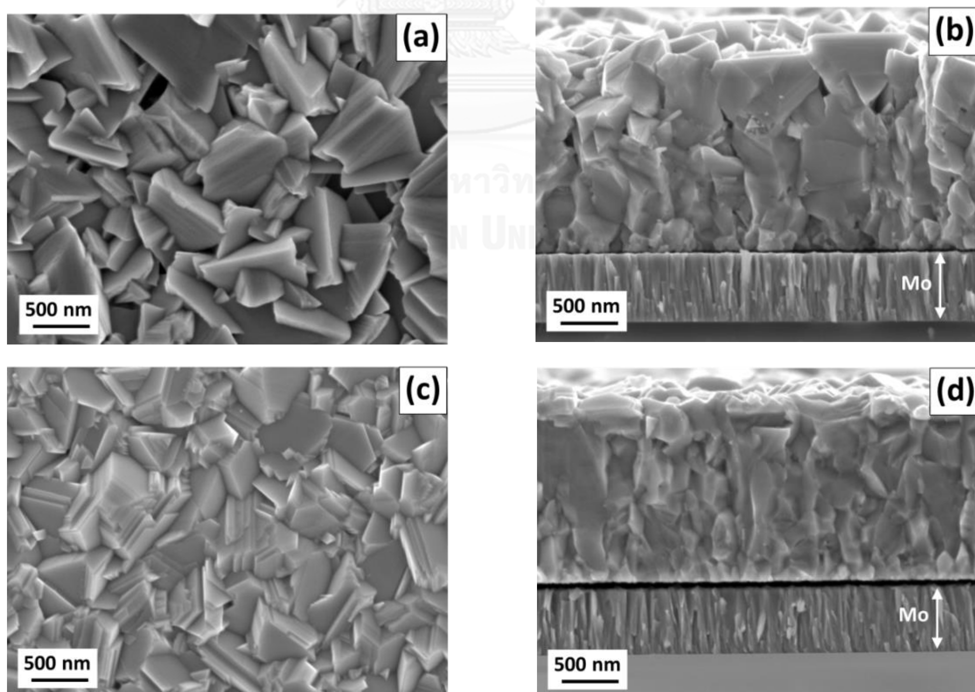

Figure 47 FESEM surface morphologies and cross-section images of (a),(b) CGS/CIS bilayers and (c),(d) CIS/CGS bilayers under Cu-rich(y=1.2)/Cu-poor(y=0.9) conditions.

5.2.2 EDS depth profiles of CGS/CIS and CIS/CGS bilayers

The EDS depth profiles of CGS/CIS and CIS/CGS bilayers are illustrated in Figure 48. In this study, the bilayers thickness was set for 1.8 μm correspond to CGS and CIS thickness of 0.67 μm and 1.13 μm, respectively. The thickness of CGS layer leads to average Ga composition of 0.37. However, Cu composition was varied for Cu-poor and Cu-rich conditions. The results show the inter-diffusion of Ga and In by the gradients of the x value in the bilayers under various Cu compositions. When CGS layer was deposited on the top layer (CGS/CIS), Ga composition was higher at the front surface and then decreased toward the back surface. This is the case of front Ga-grading. In case of back Ga-grading, Ga composition was higher at the back surface and then decreased toward the front surface in the case of CIS/CGS bilayer.

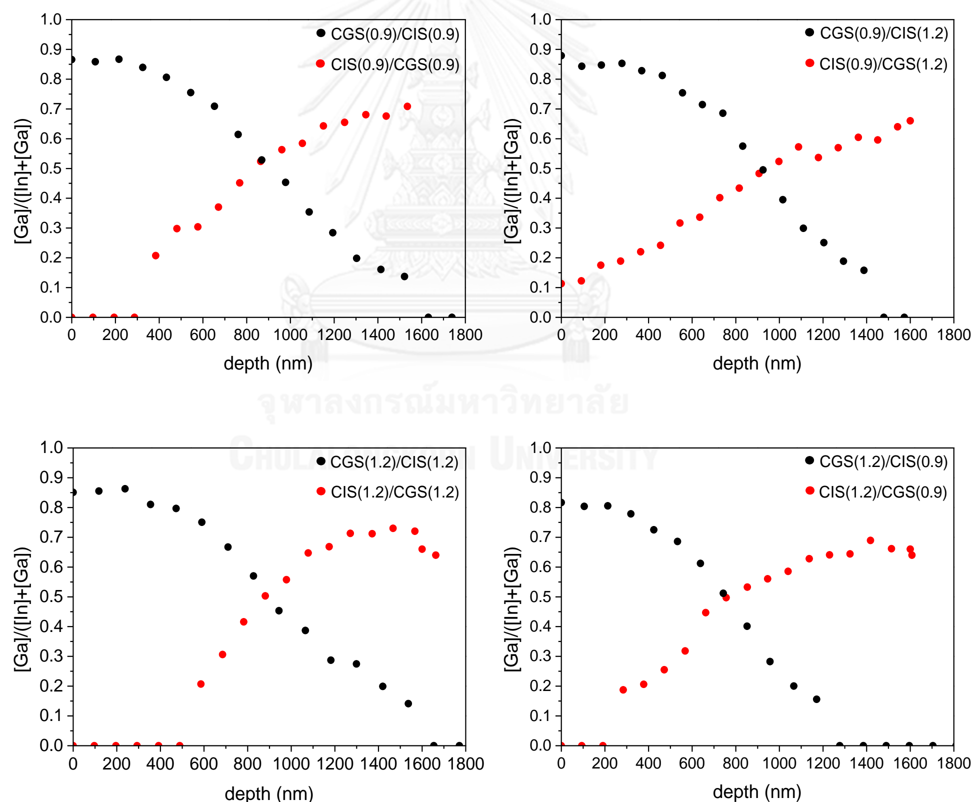

Figure 48 EDS depth profiles of CGS/CIS and CIS/CGS bilayers grown under various Cu compositions.

5.2.3 XRD patterns of CGS/CIS and CIS/CGS bilayers

The XRD patterns of CGS/CIS and CIS/CGS bilayers grown under various Cu compositions are shown in Figure 49. The (112) and (220)(204) phases of the bilayers are compared with the peaks of CGS and CIS single layer. The intensities of all bilayer conditions are lower than CIS single layer. The lower intensity of the bilayers may result in lattice mismatch between two interfaces due to non-uniform strain in the structures. This result indicates that bilayers have low crystalline quality.

It can be noticed that the two peaks of the bilayers are located between the CIS and CGS peaks. All conditions of the bilayers show separated (112) and (220)(204) peaks close to non-homogeneous alloying of CIS and CGS as a result of bilayer deposition. Thus, the doublets can be used to observe the inter-diffusion of Ga and In in the bilayer systems.

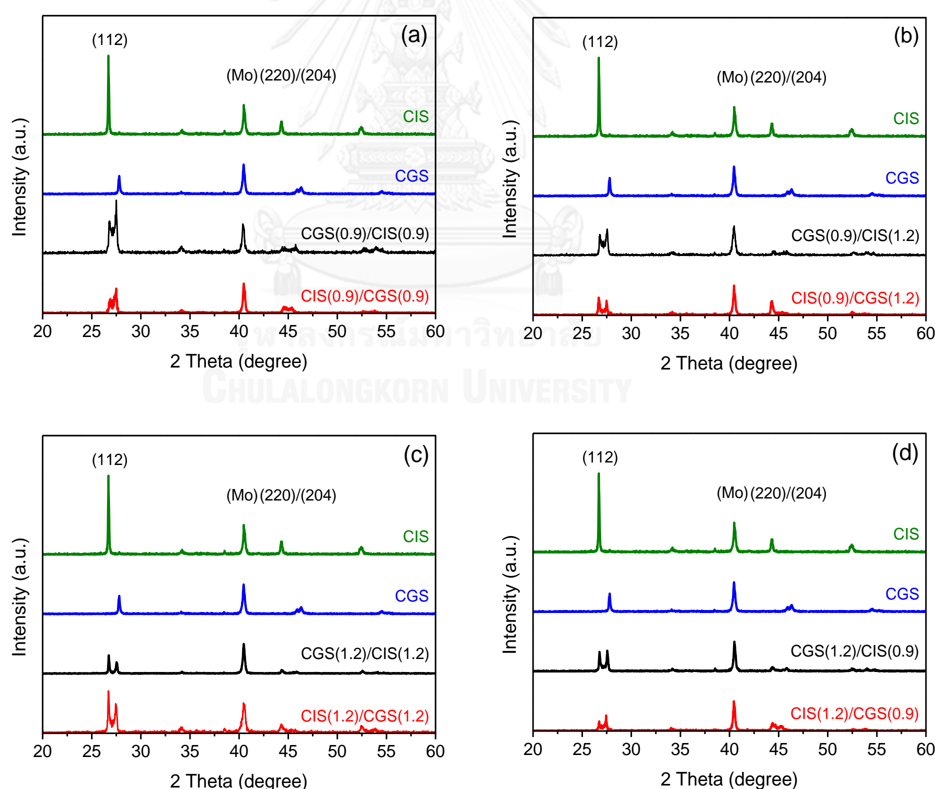

Figure 49 XRD patterns of CGS/CIS and CIS/CGS bilayers grown under various Cu compositions which compared to the CGS and CIS single layers.

5.2.4 J-V measurements of CGS/CIS and CIS/CGS bilayers

To observe the solar cell performances of the bilayers under various Cu compositions, the solar cell parameters; V_{oc}, J_{sc}, FF and η are summarized in Table 13. The efficiencies of the CGS/CIS bilayers are significantly lower than those of CIS/CGS bilayers. In case of CGS/CIS bilayers, the V_{oc} are relatively high while the J_{sc} are extremely low. As a result, the front Ga-grading can only enhance the built-in potential at the CdS/CIGS interface. In case of CIS/CGS bilayers, the J_{sc} are increased but the V_{oc} are reduced. The latter case indicates that more carriers can be collected by the assistance of the back surface field and the recombination at the back contact should be lower for back Ga-grading.

The solar cell parameters of CGS/CIS and CIS/CGS bilayers from 40 cells of each condition are plotted in Figure 50 and Figure 51, respectively. The results of Cu-poor/Cu-poor compositions of the bilayers yielded highest efficiencies for each system. It is suggested that Cu-deficient near the CdS/CIGS interface should enhance the formation of p-n junction. In addition, the FF of CIS/CGS bilayers under Cu-poor/Cu-poor was greatly improved than those of other conditions. For Cu-rich/Cu-rich compositions, the solar cell performances are relatively poor because Cu-excess compounds can cause the leakage current in the absorber layer. The highest solar cell efficiency of 12.5% was obtained from CIS(y=0.9)/CGS(y=0.9) bilayer. The J-V curves of CGS/CIS and CIS/CGS bilayers grown under various Cu compositions are shown in Figure 52.

จุฬาลงกรณ์มหาวิทยาลัย
Chulalongkorn University

Table 13 The solar cell parameters of CGS/CIS and CIS/CGS bilayers.

Bilayers conditions	V_{oc} (mV)		J_{sc} (mA/cm^2)		FF (%)		η (%)	
	Avg.	Max.	Avg.	Max.	Avg.	Max.	Avg.	Max.
CGS/CIS bilayers								
poor/poor	791.4	816.0	13.2	15.1	53.1	57.0	5.6	6.5
poor/rich	713.9	803.0	12.9	17.7	49.2	55.0	4.5	5.8
rich/rich	590.8	761.0	11.3	14.8	53.5	57.5	3.7	6.1
rich/poor	742.5	789.0	13.7	14.8	52.0	55.7	5.3	5.9
CIS/CGS bilayers								
poor/poor	527.5	565.0	33.6	37.9	67.2	69.9	11.9	12.5
poor/rich	501.6	528.0	37.1	40.3	58.0	62.7	10.8	12.5
rich/rich	446.9	498.0	34.2	41.0	45.2	55.4	6.9	9.3
rich/poor	516.8	538.0	36.6	40.2	43.9	48.8	8.3	9.6

จุฬาลงกรณ์มหาวิทยาลัย
Chulalongkorn University

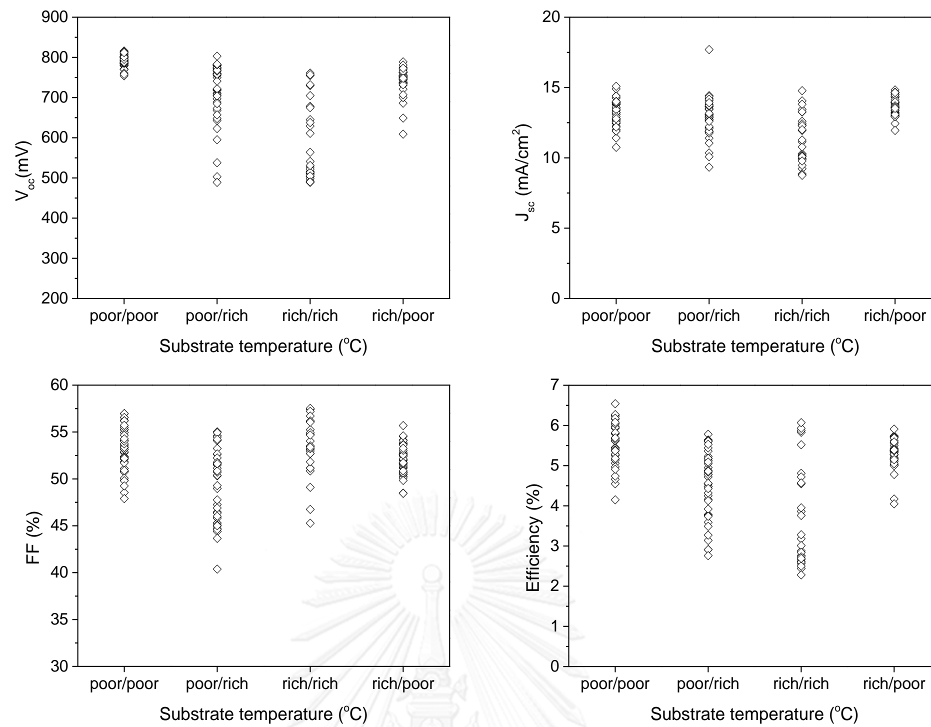

Figure 50 Distributions of CIGS solar cell parameters of the devices fabricated from CGS/CIS bilayer grown under various Cu compositions.

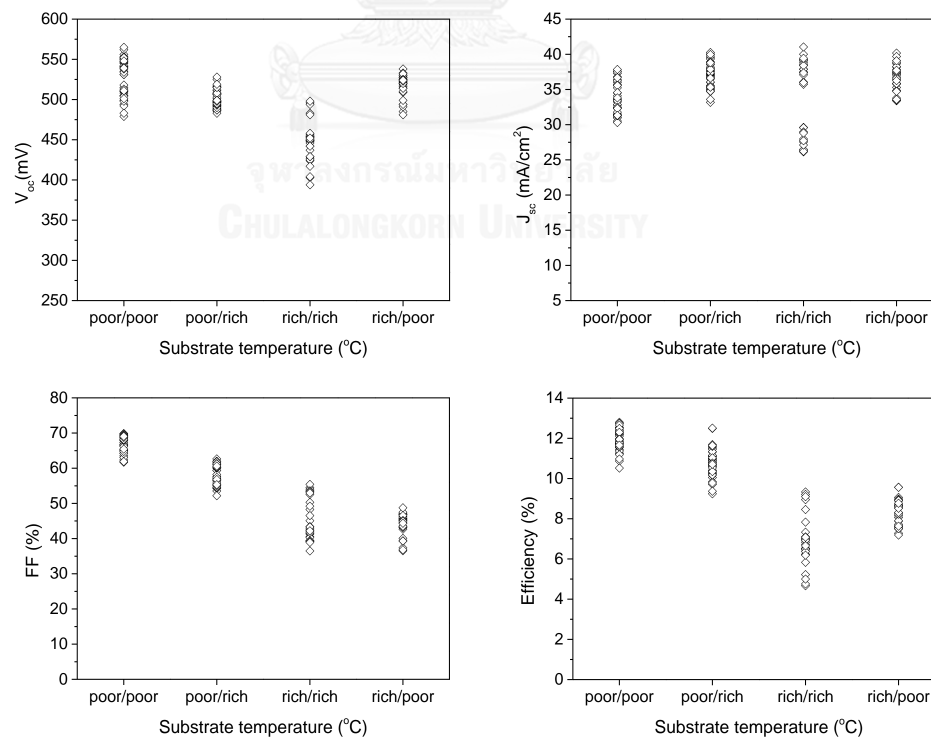

Figure 51 Distributions of CIGS solar cell parameters of the devices fabricated from CIS/CGS bilayer grown under various Cu compositions.

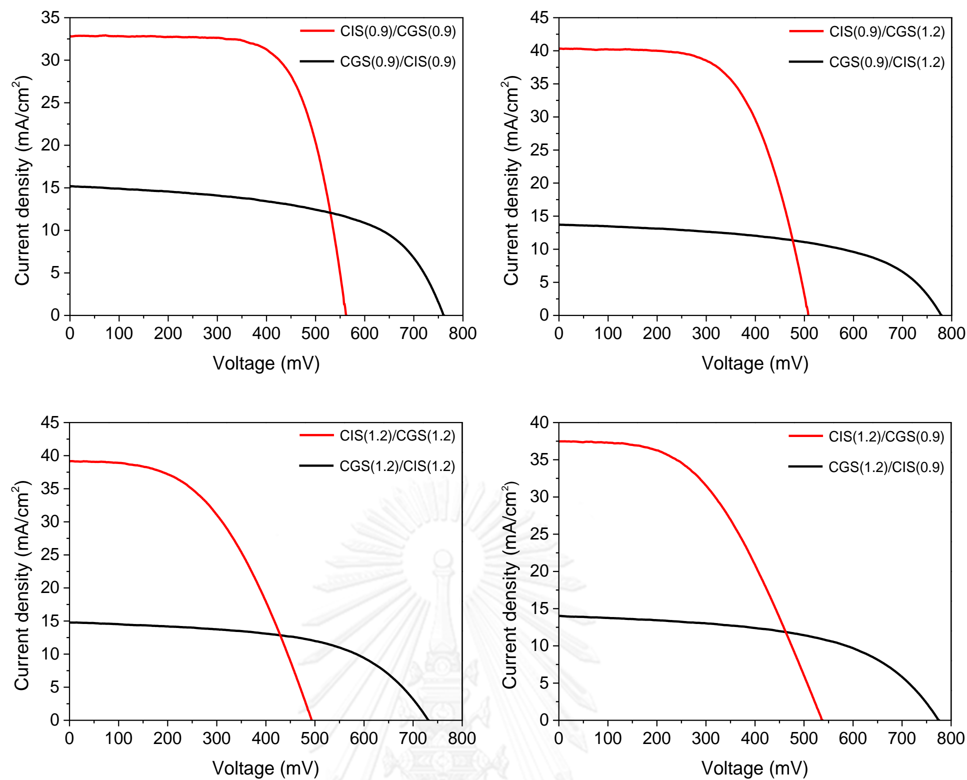

Figure 52 J-V characteristics of the devices with best efficiency fabricated from CGS/CIS and CIS/CGS bilayers grown under various Cu compositions.

จุฬาลงกรณ์มหาวิทยาลัย
Chulalongkorn University

5.2.5 EQE measurements of CGS/CIS and CIS/CGS bilayers

The external quantum efficiency (EQE) curves of CGS/CIS and CIS/CGS bilayers are shown in Figure 53. The EQE results indicate that the back Ga-grading (CIS/CGS) of all conditions can collect more carriers in the absorber layer than the front Ga-grading (CGS/CIS). For the front Ga-grading, the photocurrents are generated in the range from 350 to 850 nm due to the high V_{oc} at the p-n junction. In case of the back Ga-grading, the absorption threshold starts in a longer wavelength regions. The back Ga-grading can reduce the carrier recombination at the back contact and also the back surface field can drive more carriers inside the absorber layer toward the p-n junction leading to the increase of J_{sc} and agrees with the J-V measurements.

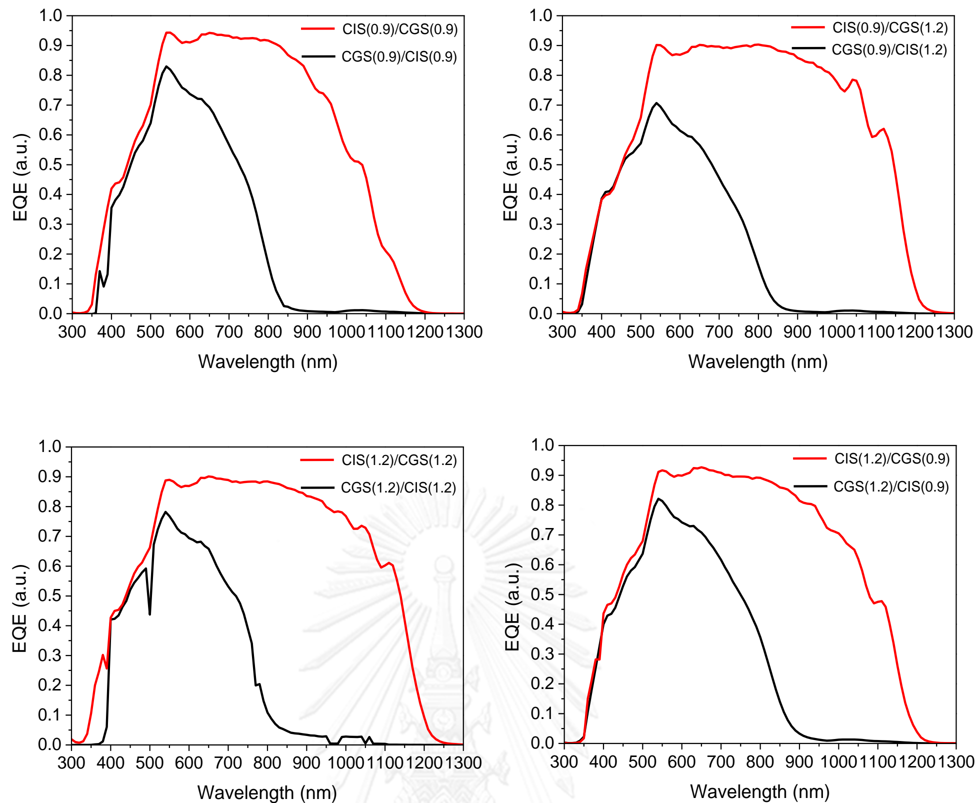

Figure 53 EQE curves of the devices with best efficiency fabricated from CGS/CIS and CIS/CGS bilayers grown under various Cu compositions.

จุฬาลงกรณ์มหาวิทยาลัย
Chulalongkorn University

It can be summarized here that the CGS/CIS and CIS/CGS bilayers were employed owing to different diffusivities of In and Ga for the growth of CIGS absorbers with slightly Cu-poor/Cu-poor condition. All bilayer conditions show separated XRD peaks (obviously the (112) plane) due to incomplete alloying of Ga and In leading to normal grading. The separated peaks with lower intensity might indicate stronger strain in the structure due to the lattice mismatch. For the solar cell performances, front grading of CGS/CIS can improve V_{oc} by increasing the conduction band edge at CdS/CIGS interface with the highest efficiency of 6.5%. The back grading of CIS/CGS bilayer can improve J_{sc} by BSF assisting carrier collections in the absorber with the highest efficiency of 12.5% in our deposition system.

5.3 CGS/CIS/CGS trilayers grown by the trilayer processes

The CGS/CIS/CGS trilayers was modified from the CIS/CGS bilayer system in order to examine the double Ga-grading affecting the solar cell performances. The standard thickness of CGS/CIS/CGS trilayers is approximately 1.8 µm for comparing with the standard process. The trilayer deposition profile is shown in Figure 54. The black line is the substrate temperature set at 560°C throughout the deposition process. The red line is the pyrometer signal and the blue line is the output power of substrate heater. The total deposition time used is about 105 minutes. In addition, the thickness reduction was examined from 1.2 µm, 0.8 µm and 0.5 µm correspond to the deposition time as 75 minutes, 52 minutes and 32 minutes, respectively.

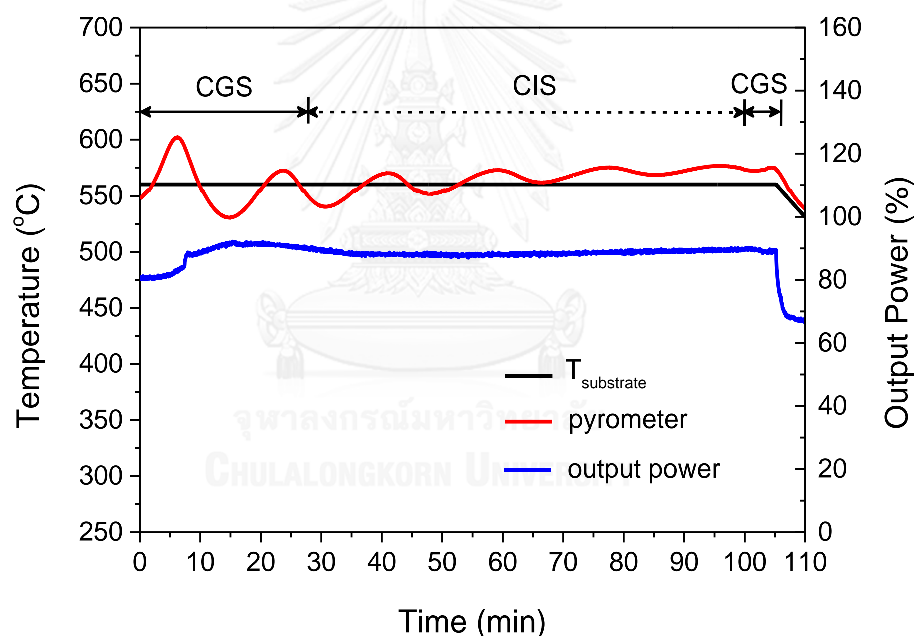

Figure 54 The trilayer process of CGS/CIS/CGS thin film which observed by the output power of substrate (blue line), the pyrometer signal (red line) and the substrate temperature (black line).

5.3.1 FESEM surface and cross-section images of CGS/CIS/CGS trilayers

The surface morphologies and cross-section images of all absorbers of the 0.5-1.8 μm thick grown by the CGS/CIS/CGS trilayers on Mo-coated SLG substrates are shown in Figure 55 (a)-(d). All surfaces show compact grains with crystalline structure. Grains with sharper edges are seen in the absorbers. The grains of the 0.5 μm thick trilayer are relatively smaller than the others due to the reduction of the growth thickness and the process time. It can also be seen that the grains along the growth direction absorbers become smaller as the absorber thickness decreases. The grains of the trilayer absorbers are closely packed with no crevices.

จุฬาลงกรณ์มหาวิทยาลัย
CHULALONGKORN UNIVERSITY

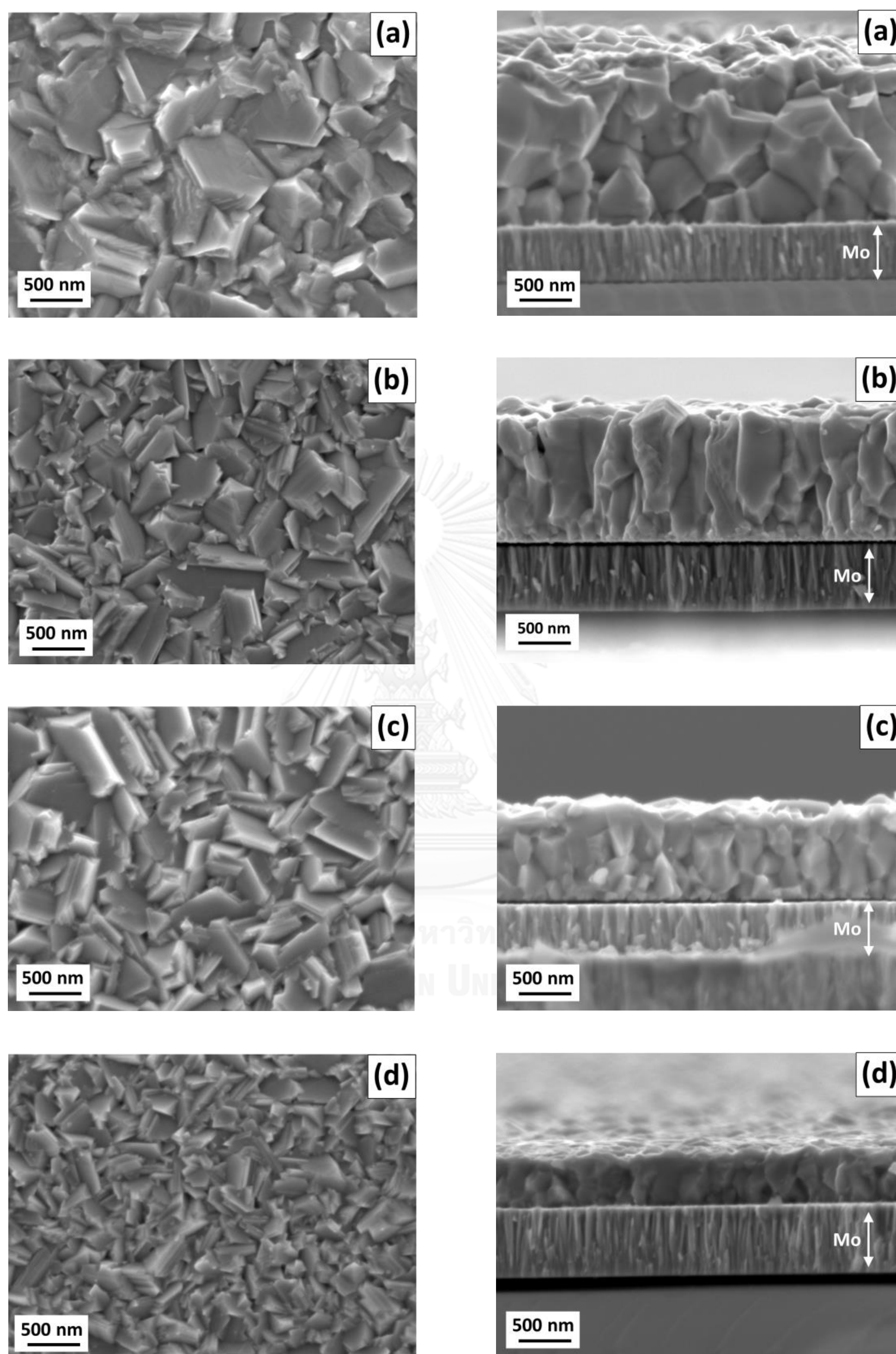

Figure 55 FESEM surface morphologies and cross-section images of various CGS/CIS/CGS trilayer thicknesses (a) 1.8 µm, (b) 1.2 µm, (c) 0.8 µm and (d) 0.5 µm.

5.3.2 EDS depth profiles of CGS/CIS/CGS trilayers

The compositional depth profiles of all absorbers were investigated by series of EDS spot scan and the results are shown in Figure 56. The Ga contents were gradually decreased, due to the inter-diffusion of In and Ga, from the back contact to about 100-200 nm below the front surface and then increased towards the surface leading to double Ga-grading. It can be noticed that the depth profiles of the thinner trilayers show relatively more uniform composition than the thicker absorbers. In all trilayers, the [Ga]/([In]+[Ga]) is raised by approximately 0.1 for about 100 nm below the surface. It was achieved by short time evaporation of CGS at the front surface in order to avoid excessive amount of Ga diffusing into the underneath CIS layer.

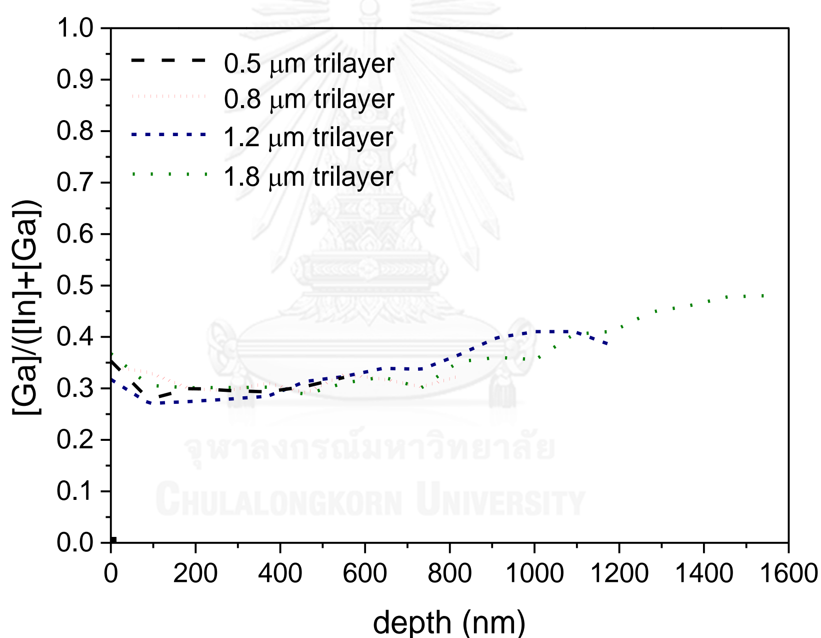

Figure 56 EDS depth profiles of various CGS/CIS/CGS trilayers thicknesses of 1.8 μm, 1.2 μm, 0.8 μm and 0.5 μm.

5.3.3 XRD patterns of CGS/CIS/CGS trilayers

The XRD patterns as illustrated in Figure 57 (a) show (112) preferred orientation in all samples. Incomplete CIGS alloying was observed by the segregation of the (112) and (220)(204) diffraction peaks in some of the samples, 1.2 and 1.8 µm thick trilayers. The shoulder in the diffraction of (112) plane in Figure 57 (b) indicates the incomplete alloying in the 1.8 µm thick trilayer leaving some part in the absorber with higher Ga concentration when compared with the 3-stage process absorber of the same thickness. For the 0.5 and 0.8 µm thick trilayers, more uniformly alloyed CIGS is observed by sharper (112) peak in both samples, however, with much lower intensity for the 0.5 µm thick absorber. On the other hand, with the reduction of the thickness of the trilayer absorbers to 0.5 and 0.8 µm, a single diffraction peak of CIGS (112) chalcopyrite phase is observed because Ga can easily diffuse to form the complete CIGS crystalline structure in a relatively shorter distance when compared with the thicker ones. The diffraction intensity of a 0.5 µm thick trilayer absorber is much lower due to a very thin layer of materials.

จุฬาลงกรณ์มหาวิทยาลัย
Chulalongkorn University

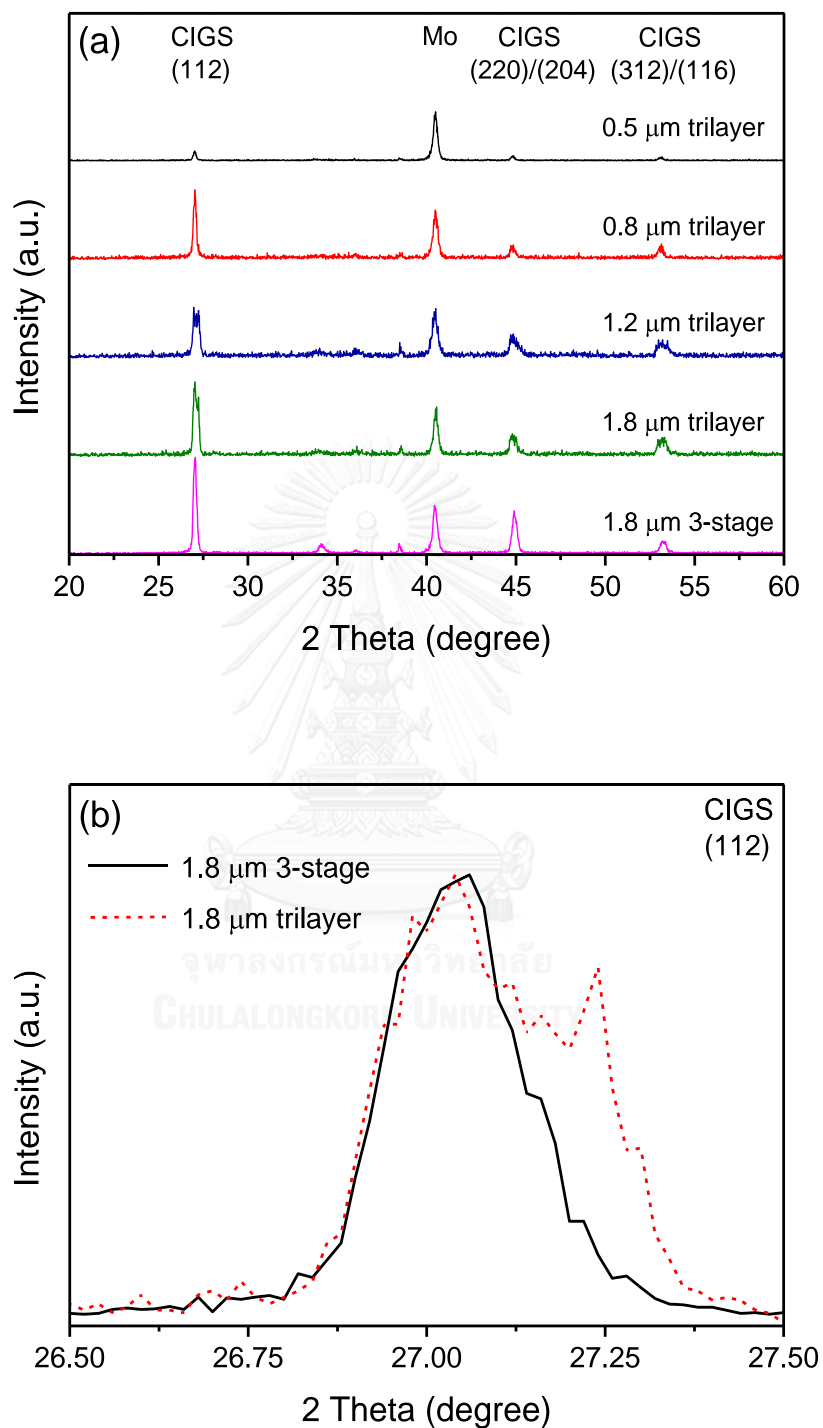

Figure 57 (a) XRD patterns of 3-stage process CIGS and various CGS/CIS/CGS trilayers thicknesses of 1.8 μm, 1.2 μm, 0.8 μm and 0.5 μm. (b) Segregation of CIGS (112) phase observed in the trilayer absorber.

5.3.4 J-V measurements of CGS/CIS/CGS trilayers

The average and maximum device parameters; V_{oc}, J_{sc}, FF and η of the trilayer absorbers are summarized in Table 14. It should be noted that the maximum values of V_{oc} and J_{sc} indicated in Table 14 do not necessarily correspond the maximum efficiency. The device parameters for the trilayer and 3-stage process absorbers are plotted and compared in Figure 58. The highest efficiency of 15.5% was obtained from the 1.8 μm thick trilayer absorber and the range of efficiencies is from 12.1% to 15.5%. The average values of the J_{sc} and V_{oc} of the 1.8 μm thick trilayer devices are comparable ~ 33.5 mA/cm^2 and 605 mV, respectively, is much higher than that of the 3-stage devices, thus resulting in higher efficiency. It can be noticed that for the trilayer devices, both V_{oc} and J_{sc} decrease as the absorber thickness is reduced. It can be seen that the thinner trilayer absorbers of 0.8 μm and 1.2 μm thick can maintain the same level of efficiency. This could significantly reduce the materials and times used in the absorber deposition process. The J-V characteristic curves of the devices with best efficiency are shown in Figure 59. It can be seen that the current density of the trilayer device is significantly higher than that of the 3-stage process device.

Table 14 The solar cell parameters of various CGS/CIS/CGS trilayer thicknesses.

Thicknesses (μm)	V_{oc} (mV)		J_{sc} (mA/cm^2)		FF (%)		η (%)	
	Avg.	Max.	Avg.	Max.	Avg.	Max.	Avg.	Max.
1.8 (3-stage)	602.7	624	31.0	33.4	66.3	65.5	12.4	13.7
1.8 (Trilayer)	605.3	620.0	33.5	35.3	67.0	71.4	13.6	15.5
1.2 (Trilayer)	566.0	588.0	29.8	33.6	71.1	73.3	12.0	12.7
0.8 (Trilayer)	548.6	564.0	29.3	32.8	70.3	71.9	11.3	12.4
0.5 (Trilayer)	533.1	566.0	23.9	26.5	69.6	71.8	8.9	10.4

จุฬาลงกรณ์มหาวิทยาลัย
Chulalongkorn University

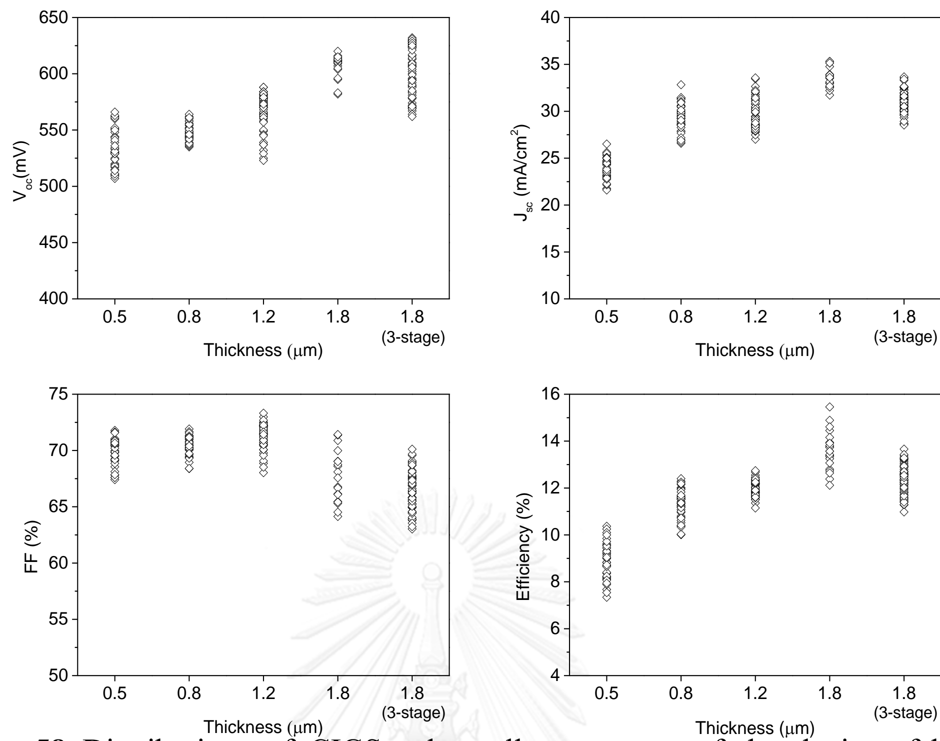

Figure 58 Distributions of CIGS solar cell parameters of the devices fabricated from1.8 μm of 3-stage process absorbers, trilayer of various thicknesses of 1.8 μm, 1.2 μm, 0.8 μm and 0.5 μm.

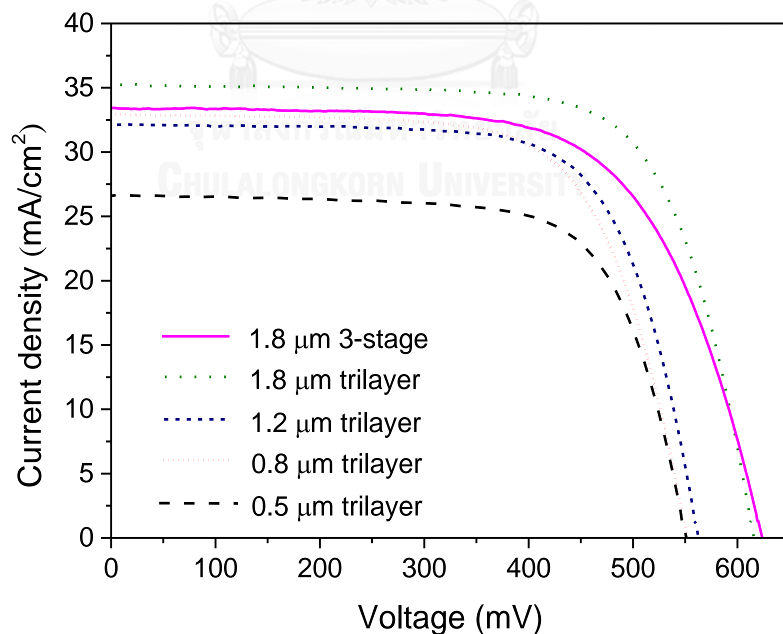

Figure 59 J-V characteristics of the devices with best efficiency fabricated from 3-stage process absorbers and various CGS/CIS/CGS trilayers thicknesses of 1.8 μm, 1.2 μm, 0.8 μm and 0.5 μm.

5.3.5 EQE measurements of CGS/CIS/CGS trilayers

The external quantum efficiency (EQE) measurements of the devices with best efficiency are shown in Figure 60. For the best devices made from 1.8 μm thick trilayer absorbers, the EQE curves show some enhancement at the wavelengths greater than 1000 nm when compared to that of the 3-stage device and that corresponds to the increase of the current density as seen in the J-V curves in Figure 58. The current collections are less in thinner absorber as expected and the absorption thresholds shift towards shorter wavelengths for the devices with thinner absorber but V_{oc} do not increase accordingly. The area under the EQE curves decreases as the thickness of absorber is reduced resulting in lower current collections.

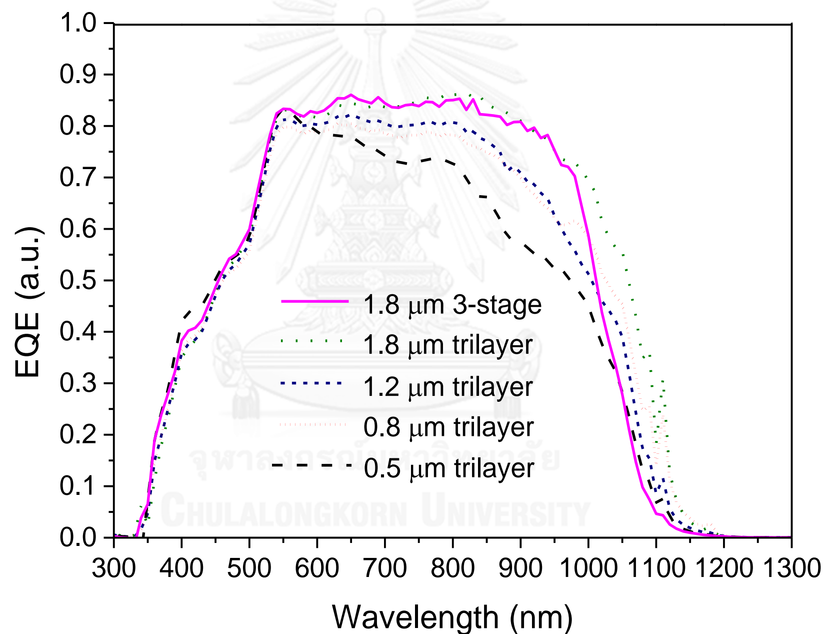

Figure 60 EQE curves of the devices with best efficiency fabricated from 3-stage process absorbers and various CGS/CIS/CGS trilayers thicknesses of 1.8 μm, 1.2 μm, 0.8 μm and 0.5 μm.

5.4 The comparison of Ga-graded and homogeneous bandgap of CIGS thin film solar cells

In this work, CIGS thin film solar cells were fabricated by the three-stage process as a representative for homogeneous Ga distribution in the absorber layer. The Ga-graded devices are obtained from CGS/CIS, CIS/CGS bilayer and CGS/CIS/CGS trilayer systems. For the bilayer and trilayer techniques, the materials and times used are reduced resulting in production cost reduction. The comparisons of the deposition times with the solar cell efficiencies grown by various techniques are illustrated in Table 15. It can be clearly seen that CGS/CIS/CGS trilayers at the thickness of 1.8 μm achieve the highest efficiency with total deposition time of 105 minutes when compared with the 120 minutes three-stage process. In addition, the thickness reduction of CGS/CIS/CGS trilayers as 1.2 μm, the solar cell efficiency as well as deposition time are comparable to CIS/CGS bilayers of 1.8 μm thick. It was found that the bilayer and trilayer systems could reduce the materials and times used in the deposition process than that of the three-stage process.

5.4.1 J-V Characteristics

จุฬาลงกรณ์มหาวิทยาลัย
Chulalongkorn University

The J-V parameters of various absorber conditions of 40 cells for each condition and the J-V curves of the devices with maximum efficiency can be seen in Figure 61 and 62, respectively. For the 1.8 μm thick CIS/CGS bilayers, the J_{sc} are enhanced by back surface field but the V_{oc} are relatively low. CGS/CIS/CGS trilayers can improve both the V_{oc} and the J_{sc} leading to the efficiency enhancement. For the homogeneous Ga distribution grown by the three-stage process, the J_{sc} are slightly less than those of the bilayer and trilayer systems with 1.8 μm thick. In case of thinner CGS/CIS/CGS trilayers, the solar cell performances decrease on the absorber becomes thinner.

5.4.2 EQE measurements

The effect of carrier collections can be seen in the EQE results as shown in Figure 63. The results show that the 1.8 μm thick CGS/CIS/CGS trilayers can enhance photocurrent generation at long wavelength regions. The results indicate that double Ga-grading can enhance both the V_{oc} and also the carrier collections by the assistance of the back surface field leading to less recombination at the interface. For thinner thicknesses, the carriers are less collected due to the absorption loss for thickness reduction.

Table 15 The deposition times with the efficiencies of the 3-stage CIGS, CIS/CGS bilayers and CGS/CIS/CGS trilayers absorbers.

Sample	Deposition process	Thickness (μm)	Total time (min)	The highest efficiency (%)
CIGS	3-stage	1.8	120	13.7
CIS/CGS	bilayers	1.8	80	12.5
CGS/CIS/CGS	trilayers	1.8	105	15.5
CGS/CIS/CGS	trilayers	1.2	75	12.7
CGS/CIS/CGS	trilayers	0.8	52	12.4
CGS/CIS/CGS	trilayers	0.5	32	10.4

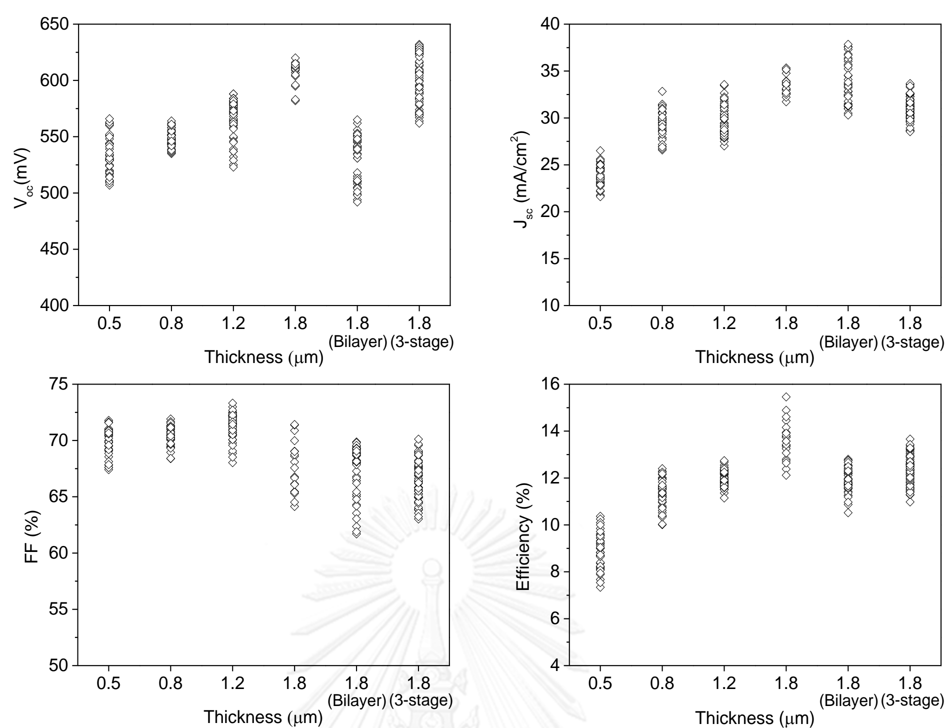

Figure 61 Distributions of CIGS solar cell parameters of the devices fabricated from bilayer, trilayer of various thicknesses and 3-stage process absorbers.

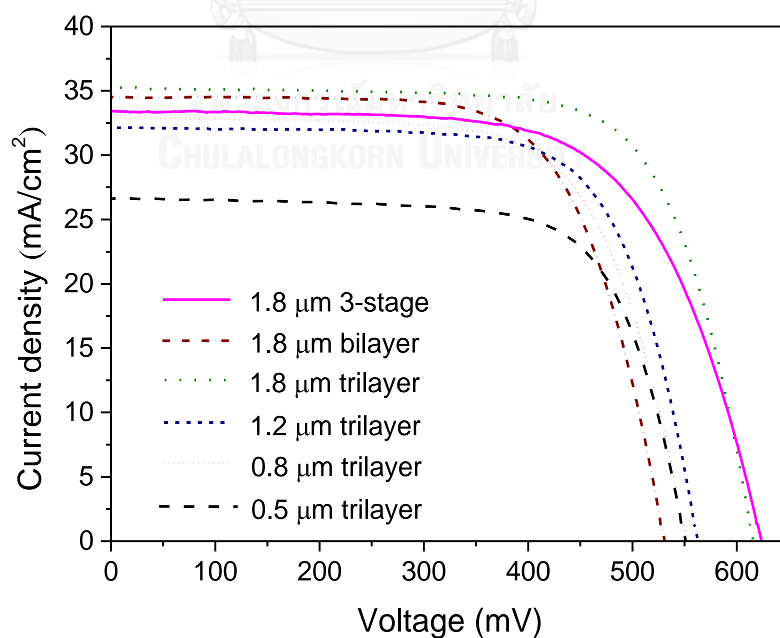

Figure 62 J-V characteristics of the devices with best efficiency fabricated from bilayer, trilayer of various thicknesses and 3-stage process absorbers.

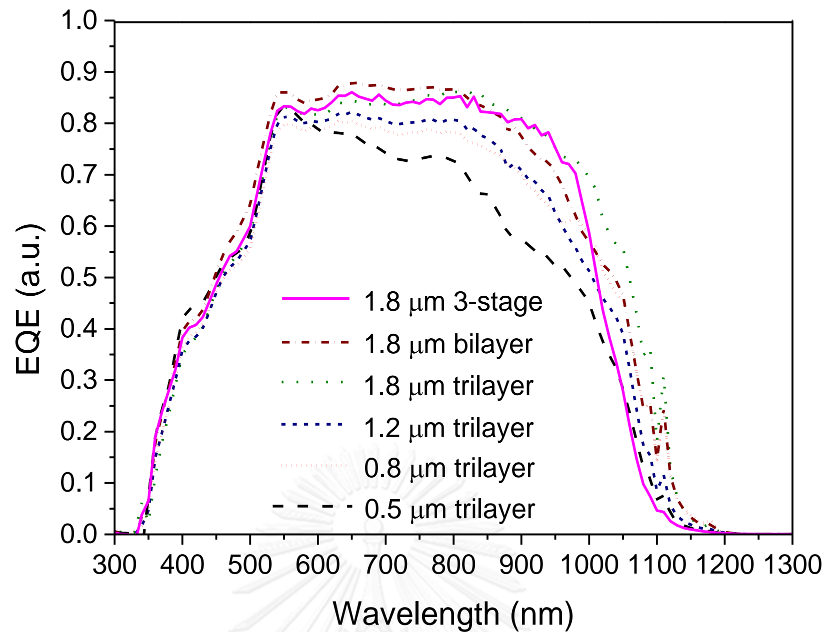

Figure 63 EQE curves of the devices with best efficiency fabricated from bilayer, trilayer of various thicknesses and 3-stage process absorbers.

5.5 Summary

It is shown in this chapter that the bandgap engineering of CGS/CIS/CGS trilayers can improve both V_{oc} and J_{sc}. The increasing of conduction band at the CdS/CIGS interface can improve the V_{oc} while the increasing of conduction band at the back surface can improve the J_{sc} by BSF assistant. The XRD peak of the trilayers shows less separation than the bilayers due to the reducing of lattice mismatch at interface. The maximum efficiency of 15.5% was obtained from the 1.8 μm thick trilayer absorber and EQE measurements indicated that the photo-generated currents were enhanced in the long wavelengths. In case of the thinner absorbers, significantly loss in the carrier collections results in the decrease of device efficiency. Thinner trilayer absorbers can maintain the same level of efficiency compared to that of the bilayer absorbers, thus the materials and process times can be significantly reduced.

CHAPTER VI
CONCLUSION

In this dissertation, I have successfully fabricated bandgap engineering CIGS absorbers for photovoltaic devices by changing Ga-grading profiles using CGS/CIS, CIS/CGS bilayer and CGS/CIS/CGS trilayer absorbers. The non-homogeneous Ga distributions can improve the solar cell parameter such as V_{oc} and J_{sc} when compared to the homogeneous Ga distributions grown by the three-stage process. To find the optimum growth condition, Se evaporation temperature and substrate temperatures were also investigated in the three-stage deposition process. Then, the normal and double grading in CIGS absorber layer were fabricated by the bilayer and trilayer processes, respectively. In addition, thickness reduction of the trilayers was examined in terms of materials and times used in the deposition process. The important results of finding in this research can be concluded as followed.

(I) Optimization of the three-stage deposition process :

- The effect of Se evaporation temperature

The formation of the $(In_{1-x}Ga_x)_2Se_3$ precursor in the 1st stage is the basis for CIGS structure. The thickness of the precursor is approximately 850 nm. The Se flux at 300°C was found to be sufficient for the 3-stage deposition process. However, at the Se source temperature of 320°C, the Se flux was inadequate for the whole deposition process in the present set up. The surface morphologies of 300°C show more of triangular grains than small round grains with [Se]/[III] elements of ~1.5 leading to the best solar cell parameters including the highest efficiency of 12.2%.

- The effect of substrate temperature in the 1st stage

The influence of γ-$(In_{1-x}Ga_x)_2Se_3$ phase transformation of (112) and (220)(204) has an important role for crystalline quality and changing in the nucleation of films in the 1st stage. The substrate temperatures of 300°C and 350°C show the higher (220)(204) phase due to residual strain in the structure. At the substrate temperatures of 370°C and 390°C, the phase transformation to (112) is likely due to nucleation and

re-crystalline structure. Then, the phase transformation to (220)(204) plane at 410°C is believe to be due to the deformation at higher temperature. The highest crystalline quality appears at 390°C leading to the highest FF up to 70.5% but the highest V_{oc} corresponding to highest efficiency up to 13.1% appears at 370°C. All T_1 conditions show large grain sizes by the excess $Cu_{2-x}Se$ that induces grain growth at higher temperature of 580°C.

- **The effect of substrate temperature in the 2nd and 3rd stages**

The influence of thermal energy enhancement from substrate in the 2nd and 3rd stages has an effect on the atomic mobility. The less inter-diffusion of atoms were slowly settled down on the precursor at lower energy at 500°C to 540°C and the columnar grains are as large as CIGS thin film thickness at 560°C and 580°C due to $Cu_{2-x}Se$ liquid phase at higher substrate temperature. Thus, the highest crystalline quality as indicated by high intensity of the (112) phase at 520°C resulting from the atomic relaxation on the basis layer leads to the maximum device efficiency of 13.7% and FF = 70.1%. This can be said that the absorbers from the optimization of the 3-stage deposition process with (112) preferred orientation generally result in high efficiency devices.

The formation of $(In_{1-x}Ga_x)_2Se_3$ precursor layer in the 1st stage was firstly examined by various Se source temperature at 280°C, 300°C and 320°C. Then, the substrate temperatures in the 1st stage were varied from 300°C, 350°C, 370°C, 390°C and 410°C with constant substrate temperature in the 2nd stage and the 3rd stages (T_2) at 580°C. Finally, the substrate temperatures in the 2nd and 3rd stages were varied from 500°C, 520°C, 540°C, 560°C and 580°C with constant substrate temperature in the 1st stage (T_1) at 370°C.

The bilayer and trilayer processes: The front and the back Ga-grading were fabricated by CGS/CIS and CIS/CGS bilayers under Cu-rich and Cu-poor conditions. The CIS/CGS bilayer grown under Cu-poor(0.9)/Cu-poor(0.9) is the optimum condition for observing the double Ga-grading of CGS/CIS/CGS trilayers. The various thickness reductions of CGS/CIS/CGS trilayers were varied from 1.8 μm, 1.2

μm, 0.8 μm and 0.2 μm.

(II) CGS/CIS and CIS/CGS bilayers :

The CGS/CIS and CIS/CGS bilayers were employed owing to different diffusivities of In and Ga for the growth of CIGS absorbers with slightly Cu-poor/Cu-poor condition leading to the best overall performances. All bilayer conditions show separated peaks of XRD due to incomplete alloying of Ga and In leading to normal grading. In addition, the lower XRD intensity results from the strain in the structure due to the lattice mismatch. The cross-section images show that the grains along the growth direction of the bilayer absorber are relatively smaller than those of the 3-stage and trilayer absorbers of the same thickness. For the solar cell performances, the front grading from the CGS/CIS bilayer can improve V_{oc} by increasing the conduction band edge at CdS/CIGS interface with the highest efficiency of 6.5%, while the back grading from the CIS/CGS bilayer can enhance J_{sc} by BSF assisting carrier collections in the absorber with the highest efficiency of 12.5% in our present deposition system.

(III) CGS/CIS/CGS trilayers :

The bandgap engineering of CGS/CIS/CGS trilayers is the result from the the bilayer system that can enhance both V_{oc} and J_{sc}. The XRD shows less separation of the peaks than the bilayers of the same thickness that could be due to reduction of lattice mismatch at the interface or better alloying between layers. The EDS depth profiles show Ga contents with x ~ 0.3-0.37 near the surface of all thicknesses. The Ga contents slightly decreased for about the depth of 100 nm below the surface of the trilayers and gradually increased towards the back contact leading to a double-graded band gap. As a result, the average value of the efficiency of the trilayer is higher than that of the bilayer and the 3-stage process absorbers. The maximum efficiency of 15.5% was obtained from the trilayer absorber. EQE measurements indicated that the photo-generated currents were enhanced in the long wavelengths for the 1.8 μm thick trilayer absorbers when compared to that of the 3-stage process absorber. In case of thinner absorbers, significantly loss in the carrier collections results in the decrease of device efficiency. Thinner trilayer absorbers can maintain the same level of efficiency by BSF assistant, thus the materials and process times can be significantly reduced.

REFERENCES

1. Kodigala, S.R., *$Cu(In_{1-x}Ga_x)Se_2$ based thin film solar cells*. Vol. 35. 2010.
2. Luque, A., Hegedus, S., *Handbook of photovoltaic science and engineering*. 2 ed. 2011, United Kingdom: John Wiley & Sons, Ltd.
3. *A strategic research agenda for photovoltaic solar energy technology*. 2 ed. 2011, Luxembourg Publications Office of the European Union.
4. Ullal, H.S., Zweibel, K., Roedem, B.G. von *Thin-Film CdTe and $CulnSe_2$ Photovoltaic Technology.* Prepared for the ISES Solar World Congress Budapest, Hungary, 1993: p. 1-8.
5. Huang, C.-H., *Effects of Ga content on $Cu(In,Ga)Se_2$ solar cells studied by numerical modeling.* Journal of Physics and Chemistry of Solids, 2008. **69**: p. 330–334.
6. Sakdanuphab, R., Chityuttakan, C., Pankiew, A., Somwang, N., Yoodee, K., Chatraphorn, S., *Growth characteristics of $Cu(In,Ga)Se_2$ thin films using 3-stage deposition process with a NaF precursor* Journal of Crystal Growth 2011. **319**: p. 44–48.
7. *Solar Frontier. Solar Frontier achieves world record thin–film solar cell efficiency: 22.3%. 2015 [Cited 2016 22/04/2016]; Avaliable from: http://www.solar-frontier.com/eng/news/2015/C051171.html.*
8. Green, M.A., Emery, K., Hishikawa, Y., Warta W., Dunlop, E.D. , *Solar cell efficiency tables (version 47).* Prog. Photovolt: Res. Appl., 2016. **24**: p. 3-11.
9. Jia, T., Dong, L., Zhao, Z., Li, X., Li, D., *Structurally tailored $Cu(In_xGa_{1-x})Se_2$ thin films via RF magnetron sputtering.* Surface & Coatings Technology, 2014. **259**: p. 94–97.
10. Zhu, X.L., Wang, Y.M., Zhou, Z., Li, A.M., Zhang, L., Huang, F.Q., *13.6%-efficient $Cu(In,Ga)Se_2$ solar cell with absorber fabricated by RF sputtering of $(In,Ga)_2Se_3$ and CuSe targets.* Solar Energy Materials & Solar Cells 2013. **113**: p. 140–143.
11. Nakada, T., Onishi, R., Kunioka, A., *$CulnSe_2$-based solar cells by Se-vapor selenization from Se-containing precursors.* Solar Energy Materials and Solar Cells 1994. **35** p. 209-214.

จุฬาลงกรณ์มหาวิทยาลัย
Chulalongkorn University

12. Liang, H., Avachat, U., Liu, W., Duren, J. van, Le, M. , *CIGS formation by high temperature selenization of metal precursors in H_2Se atmosphere.* Solid-State Electronics, 2012. **76**: p. 95–100.

13. Deshmukh, L.P., Suryawanshi, R.V., Masumdar, E.U., Sharon, M. , *$Cu_{1-x}In_xSe_2$ thin films: Deposition by spray pyrolysis and characteristics.* Solar Energy 2012. **86**: p. 1910–1919.

14. Valdés, M.H., Berruet, M., Goossens, A., Vázquez, M. , *Spray deposition of $CuInS_2$ on electrodeposited ZnO for low-cost solar cells.* Surface & Coatings Technology 2010. **204**: p. 3995-4000.

15. Calixto, M.E., Sebastian, P.J., Bhattacharya, R.N., Noufi, R., *Compositional and optoelectronic properties of CIS and CIGS thin fims formed by electrodeposition.* Solar Energy Materials & Solar Cells 1999. **59** p. 75-84.

16. Bhattacharya, R.N., Hiltner, J.F., Batchelor, W., Contreras, M.A., Noufi, R.N., Sites, J.R. , *15.4% $CuIn_{1-x}Ga_xSe_2$-based photovoltaic cells from solution-based precursor films.* Thin Solid Films 2000. **361-362**: p. 396-399.

17. Hunger, R., Sakurai K., Yamada, A., Fons, P., Iwata, K., Matsubara, K., Niki, S., *In situ deposition rate monitoring during the three-stage-growth process of $Cu(In,Ga)Se_2$ absorber films.* Thin Solid Films 2003. **431-432**: p. 16-21.

18. Ramanathan, K., Teeter, G., Keane, J.C., Noufi, R. , *Properties of high-efficiency $CuInGaSe_2$ thin film solar cells.* Thin Solid Films 2005. **480-481**: p. 499-502.

19. Miguel A. Contreras, B.E., K. Ramanathan, J. Hiltner, A. Swartzlander, F. Hasoon, Rommel Noufi, *Progress Toward 20% E • fficiency in $Cu(In,Ga)Se_2$ Polycrystalline Thin-film Solar Cells.* Prog. Photovolt: Res. Appl. , 1999. **7**: p. 311-316.

20. Namnuan, B., Yoodee, K., Chatraphorn, S., *Probing diffusion of In and Ga in $CuInSe_2$/$CuGaSe_2$ bilayer thin films by x-ray diffraction.* Journal of Crystal Growth 2015. **432**: p. 24–32.

21. Contreras, M.A., Tuttle, J., Gabor, A., Tennant, A., Ramanathan, K., Asher, S., Franz, A., Keane, J., Wang, L., Scofield, J., Noufi, R., *HIGH EFFICIENCY $Cu(ln,Ga)Se_2$-BASED SOLAR CELLS: PROCESSING OF NOVEL ABSORBER STRUCTURE.* First WCPEC, 1994: p. 68-75.

จุฬาลงกรณ์มหาวิทยาลัย
Chulalongkorn University

22. Dullweber, T., Hanna, G., Rau, U., Schock, H.W. , *A new approach to high-efficiency solar cells by band gap grading in $Cu(In,Ga)Se_2$ chalcopyrite semiconductors.* Solar Energy Materials & Solar Cells 2001. **67** p. 145-150.
23. Schleussner, S., Zimmermann, U., Watjen, T., Leifer, K., Edoff, M., *Effect of gallium grading in $Cu(In,Ga)Se_2$ solar-cell absorbers produced by multi-stage coevaporation.* Solar Energy Materials & Solar Cells 2011. **95**: p. 721–726.
24. Lundberg, O., Lu, J., Rockett, A., Edoff, M., Stolt, L. , *Diffusion of indium and gallium in $Cu(In,Ga)Se_2$ thin film solar cells.* Journal of Physics and Chemistry of Solids 2003. **64**: p. 1499–1504.
25. Lundberg, O., Edoff, M., Stolt, L. , *The effect of Ga-grading in CIGS thin film solar cells.* Thin Solid Films 2005. **480–481**: p. 520–525.
26. Rau, U., Schock, H.W. , *$Cu(In,Ga)Se_2$ Thin-Film Solar Cells*. 2013: Institut fur Physikalische Elektronik (IPE), Universitat Stuttgart, Germany. p. 262-274.
27. Ohring, M., *The materials science of thin films*. 1992: Academic Press.
28. SEYRLING, S.R., *Advanced Concepts for $Cu(In,Ga)Se_2$ Thin Film Solar Cells*. 2011, ETH ZURICH.
29. Rudmann, D., *Effect of sodium on growth and the properties of $Cu(In,Ga)Se_2$ thin films and solar cells*. 2004, SWISS FEDERAL INSTITUTE OF TECHNOLOGY (ETH) ZURICH. p. 199.
30. Thantsha, N.M., *ON THE CHARACTERISATION OF COPPER INDIUM DISELENIDE BASED PHOTOVOLTAIC DEVICES*. 2006, Nelson Mandela Metropolitan University. p. 118.
31. Lu, J.G., Fujita, S., Kawaharamura, T., Nishinaka, H., Kamada, Y., Ohshima, T., Ye, Z.Z., Zeng, Y. J., Zhang, Y.Z., Zhu, L.P., He, H.P., Zhao, B.H. , *Carrier concentration dependence of band gap shift in n-type ZnO:Al films.* Journal of Applied Physics, 2007. **101**.
32. Gabor, A.M., Tuttle, J.R., Bode, M.H., Franz A., Tennant, A.L., Contreras, M.A., Noufi, R., Jensen, D.G., Hermann, A.M. , *Band-gap engineering in $Cu(In,Ga)Se_2$ thin films grown from $(In,Ga)_2 5e_3$ precursors.* Solar Energy Materials and Solar Cells 1996. **41/42** p. 247-260.

33. Dullweber, T., Lundberg, O., Malmstrom, J., Bodegard, M., Stolt, L., Rau, U., Schock, H.W., Werner, J.H. , *Back surface band gap gradings in Cu(In,Ga)Se_2 solar cells.* Thin Solid Films 2011. **387** p. 11-13.

34. Bodegard, M., Granath, K., Stolt, L., Rockett, A., *The behaviour of Na implanted into Mo thin films during annealing.* Solar Energy Materials & Solar Cells, 1999. **58**: p. 199-208.

35. Kohara, N., Nishiwaki, S., Hashimoto, Y., Negami, T., Wada, T., *Electrical properties of the Cu(In,Ga)Se_2/$MoSe_2$/Mo structure.* Solar Energy Materials & Solar Cells 2001. **67**: p. 209-215.

36. Wada, T., Kohara, N., Nishiwaki, S., Negami, T. , *Characterization of the Cu(In,Ga)Se_2/Mo interface in CIGS solar cells.* Thin Solid Films 2001. **387** p. 118-122.

37. O'Brien, P., McAleese, J., *Developing an understanding of the processes controlling the chemical bath deposition of ZnS and CdS.* Journal of Materials Chemistry Feature Article 1998. **8(11)**: p. 2309–2314.

38. Quang, N.H., *The Role of the Heterointerfaces in the Cu(In,Ga)Se_2 Thin Film Solar Cell with Chemical Bath Deposited Buffer Layers*. 2004. p. 110.

39. Ishizuka, S., Sakurai, K., Yamada, A., Matsubara, K., Fons, P., Iwata, K., Nakamura, S., Kimura, Y., Baba, T., Nakanishi, H., Kojima, T., Niki, S. , *Fabrication of wide-gap Cu($In_{1-x}Ga_x$)Se_2 thin film solar cells: a study on the correlation of cell performance with highly resistive i-ZnO layer thickness.* Solar Energy Materials and Solar Cells, 2005. **87**(1-4): p. 541-548.

40. Xiao-Tao Hao, J.M., De-Heng Zhang, Ying-Ge Yang, Hong-Lei Ma, Chuan-Fu Cheng, Xiang-Dong Liu, *Comparison of the properties for ZnO:Al films deposited on polyimide and glass substrates.* Materials Science and Engineering 2002. **B90**: p. 50–54.

41. Sukaiem, S., *QUANTUM EFFICIENCY MEASUREMENTS OF $CuIn_{1-x}Ga_xSe_2$ SOLAR CELLS*. 2014, Chulalongkorn University. p. 78.

42. Mise, T., Nakada, T., *Microstructural properties of $(In,Ga)_2Se_3$ precursor layers for efficient CIGS thin-film solar cells.* Solar Energy Materials and Solar Cells, 2009. **93**(6-7): p. 1000-1003.

APPENDIX

List of Symbols and Abbreviations

Symbols

μm	Micrometer (10^{-6})
Å	Angstrom
a	Lattice parameter
a.u.	Arbitrary unit
b	Bowing parameter
c	Lattice parameter
C_B	Conduction band
E_C	Conduction band energy
E_F	Fermi energy
E_g	Bandgap energy
eV	Energy unit: electron volt
E_v	Valance band energy
FF	Fill factor
Ga_{Cu}	Gallium substitution to Copper site
In_{Cu}	Indium substitution to Copper site
i-ZnO	Intrinsic zinc oxide
J_0	Reverse saturation current density
J_D	Dark current density
J_L	Photocurrent density
J_{sc}	Short-circuit current density
J-V	Current density-Voltage
K	Temperature unit: Kelvin
k_B	Boltzmann constant
K-cells	Knudsen cells
M	Molecular mass
n	Diode ideality
N_A	Avogadro's number

nm	Nanometer (10^{-9} m)
^oC	Temperature unit: degree celsius
P	Power unit: watt
rf	Radio frequency
R_s	Series resistance
R_{sh}	Shunt resistance
T_1	Substrate temperatures during 1st stage
T_2	Substrate temperatures during 2nd and 3rd stage
Torr	Pressure unit
V_B	Valence band
V_{Cu}	Copper vacancy
V_{oc}	Open-circuit voltage
x	[Ga]/([In]+[Ga]) ratio
$y < 1$	Cu-poor composition
$y = 1$	Stoichiometric composition
$y > 1$	Cu-rich composition
y	[Cu]/([In]+[Ga]) ratio
α	Absorption coefficient
ε	Emissivity
η	Conversion efficiency
λ	Wavelength
ρ	Density

จุฬาลงกรณ์มหาวิทยาลัย
Chulalongkorn University

Abbreviations

Al	Aluminum
AM	Air mass
BEI	Backscatter electron image
BSF	Back surface field
CBD	Chemical bath deposition
CdS	Cadmium sulfide
CGS	Copper gallium diselenide; $CuGaSe_2$
CIGS	Copper indium gallium diselenide; $Cu(InGa)Se_2$
CIS	Copper indium diselenide; $CuInSe_2$
Cu	Copper element
Cu_2Se	Copper selenide
DC	Direct current
DI	De-ionized
EDS	Energy dispersive X-ray spectroscopy
EPD	End point detection
EQE	External quantum efficiency
EQE	External quantum efficiency
FESEM	Field emission scanning electron microscope
Ga	Gallium element
H_2CrO_4	Chromic acid
H_2Se	Hydrogen selenide
IGS	$(In,Ga)_2Se_3$ compound
In	Indium element
ITO	Tin-doped In_2O_3
i-ZnO	Intrinsic zinc oxide
KCN	Potassium cyanide
MgF_2	Magnesium fluoride
Mo	Molybdenum element
$MoSe_2$	Molybdenum selenide
NH_3	Ammonia solutions
ODC	Order defect compound

จุฬาลงกรณ์มหาวิทยาลัย
Chulalongkorn University

OVC	Order vacancy compound
PID	proportional–integral–derivative
PV	Photovoltaic
QCM	Quartz crystal monitor
$SC(NH_2)_2$	Thiourea
SCR	Space charge region
Se	Selenium element
SLG	Soda-lime glass
SnO_2	Tin oxide
XRD	X-ray diffraction
ZnO(Al)	Aluminum doped zinc oxide

จุฬาลงกรณ์มหาวิทยาลัย
CHULALONGKORN UNIVERSITY

VITA

Busarin Noikaew was born on 6th February 1983 in Bangkok and lived in Suphanburi province, Thailand. She received her Bachelor degree of Science in Physics from Silpakorn University in 2005, and received her Master degree of Science in Physics from King Mongkut's University of Technology Thonburi in 2009.

LIST OF CONFERENCES

1. Noikaew, B. and Chatraphorn, S. "The fabrication of 10 cm x 10 cm CIGS thin films by small co-evaporation system" The Eighth Mathematics and Physical Science Graduate Congress (8thMPSGC), Faculty of Science, Chulalongkorn University, Bangkok, Thailand, 8-10 December 2012.

2. Noikaew, B., Puangsudrak, M., Yoodee, K. and Chatraphorn, S. "The fabrication of 10 cm x 10 cm CIGS thin films by small co-evaporation system" 2013 Niigata Graduate Research Forum, TOKIMESSE Niigata Convention Center, Japan, 10-16 January 2013.

3. Noikaew, B., Puangsudrak, M., Sakdanuphab, R., Arthibenyakul, B., Yoodee, K. and Chatraphorn, S. "The fabrication of 10 cm x 10 cm CuIn1-xGaxSe2 thin films by small co-evaporation system" The 8th Annual Conference of the Thai Physics Society (SPC 2013), Chiang Mai, Thailand, 21-23 March 2013.

4. Noikaew, B., Namnuan, B., Sukaiem, S., Yoodee, K., and Chatraphorn, S. "Influence of thickness reduction for CGS/CIS/CGS absorber layer on solar cell performance" The 10th Annual Siam Physics Congress 2015 (SPC 2015), Krabi, Thailand, 20-22 May 2015.